

PAPER • OPEN ACCESS

Measurement of spherical tokamak plasma compression in a PCS-16 magnetized target fusion experiment

To cite this article: S.J. Howard *et al* 2025 *Nucl. Fusion* **65** 016029

View the [article online](#) for updates and enhancements.

You may also like

- [The role of ion-scale micro-turbulence in pedestal width of the DIII-D wide-pedestal QH mode](#)
Zeyu Li, Xi Chen, Xiang Jian et al.
- [Gyrokinetic simulation of the interplay between ion temperature gradient turbulence and reversed shear Alfvén Eigenmodes](#)
Yuheng Yang, Lei Ye, Yang Chen et al.
- [Assessment of validity of local neoclassical transport theory for studies of electric-field root-transitions in the W7-X stellarator](#)
M.D. Kuczyski, R. Kleiber, H.M. Smith et al.

Measurement of spherical tokamak plasma compression in a PCS-16 magnetized target fusion experiment

S.J. Howard^{*} , M. Reynolds , A. Froese , R. Zindler, M. Hildebrand, A. Mossman, M. Donaldson, T. Tyler, D. Froese, C. Eylich, K. Epp, K. Bell, P. Carle, C. Gutjahr, A. Wong, W. Zawalski, B. Rablah, J. Sardari, L. McIlwraith, R. Bouchal, J. Wilkie, R. Ivanov, P. de Vietien, I.V. Khalzov , S. Barsky, D. Krotez, M. Delage, C.P. McNally  and M. Laberge 

General Fusion Inc., Richmond, British Columbia, Canada

E-mail: stephen@generalfusion.com

Received 10 May 2024, revised 25 October 2024

Accepted for publication 8 November 2024

Published 26 November 2024



Abstract

A sequence of magnetized target fusion devices built by General Fusion has compressed magnetically confined deuterium plasmas inside imploding aluminum liners. Here we describe the best-performing compression experiment, PCS-16, which was the fifth of the most recent experiments that compressed a spherical tokamak plasma configuration. In PCS-16, the plasma remained axisymmetric with $\delta B_{\text{pol}}/B_{\text{pol}} < 20\%$ to a high radial compression factor ($C_R > 8$) with significant poloidal flux conservation (77% up to $C_R = 1.7$, and $\approx 30\%$ up to $C_R = 8.65$) and a total compression time of 167 μs . Magnetic energy of the plasma increased from 0.96 kJ poloidal and 17 kJ toroidal to a peak of 1.14 kJ poloidal and 29.9 kJ toroidal during the compression, while the thermal energy was in the range of 350 ± 25 J. Plasma equilibrium was a low- β state with $\beta_{\text{tor}} \approx 4\%$ and $\beta_{\text{pol}} \approx 15\%$. Ingress of impurities from the lithium-coated aluminum wall was not the dominant effect. Neutron yield from D-D fusion increased significantly during compression. Thermodynamics during the early phase of compression ($C_R < 1.7$) were consistent with increasing Ohmic heating of the electrons due to a geometric increase in the current density at near-constant resistivity, and with increasing ion cooling that approximately matched ion compression heating power. Ion cooling by electrons was significant because the electrons were much cooler than the ions ($T_e = 200\text{eV}$, $T_i = 600\text{eV}$). Magnetohydrodynamic simulations were used to model the emergence of instabilities that increase electron thermal transport in the final phase of compression. Conditions for ideal stability were actively maintained during compression through a current ramp applied to the central shaft and, after this current ramp reached its peak two-thirds of the way through compression, we measured a transition in plasma behavior across multiple diagnostics.

* Author to whom any correspondence should be addressed.



Original Content from this work may be used under the terms of the [Creative Commons Attribution 4.0 licence](https://creativecommons.org/licenses/by/4.0/). Any further distribution of this work must maintain attribution to the author(s) and the title of the work, journal citation and DOI.

Supplementary material for this article is available [online](#)

Keywords: magnetized target fusion, spherical tokamak, experimental plasma physics, plasma confinement, magnetohydrodynamics, coaxial helicity injection

(Some figures may appear in colour only in the online journal)

Contents

1. Introduction	2
2. Theory of plasma evolution during MTF compression	3
2.1. Non-ideal scaling with cooling and resistive flux loss	4
2.2. MHD stability during compression	5
3. PCS on a mobile platform	6
3.1. Plasma diagnostics	10
3.2. PCS-16 compression shot	10
3.3. Implosion kinematics	11
4. PCS-16 results	11
4.1. Density rise during compression and implied profile	13
4.2. Peak magnetic compression ratio	15
4.3. Poloidal flux conservation during compression	16
4.4. Electron temperature from filtered AXUV soft x-ray ratio	17
4.5. Ion temperature from IDS	18
4.6. Ion temperature from neutron analysis	20
4.7. Evolution of asymmetry in the poloidal magnetic field during compression	24
5. Comparison of simulation with experiment	26
5.1. Linear stability analysis	26
5.2. MHD simulations to match experimental signals	27
6. Improvements for future devices	30
7. Concluding remarks	31
Acknowledgments	32
Appendix A. Derivation of MTF scaling formula	32
Appendix B. Neutron yield calibration by MCNP simulation	33
Appendix C. Bayesian equilibrium reconstruction	36
Appendix D. Electron temperature lower bound from poloidal flux decay	36
Appendix E. Electron temperature lower bound from neutron measurements	37
Appendix F. Ion thermalization	38
Appendix G. Effective charge and fuel dilution	38
References	38

1. Introduction

In magnetized target fusion (MTF), a magnetized plasma is compressed in a time shorter than its initial thermal energy confinement time, thereby heating to fusion conditions [1]. An understanding of plasma behavior and confinement scaling laws during MTF-relevant compression scenarios is needed to

advance toward a reactor-scale demonstration. General Fusion [2–4] has conducted a sequence of subscale experiments in which compact toroid plasmas are compressed by the chemically driven implosion of an aluminum liner, providing data on how a magnetized plasma behaves as it is rapidly compressed, which may help to empirically address the key practical considerations necessary for MTF methods to reach fusion energy-producing conditions.

This sequence of subscale tests is designated Plasma Compression Science (PCS). In these devices, compact toroid plasmas were formed by the discharge of a coaxial magnetized Marshall gun [5], similar to spheromak formation [6] or coaxial helicity injection (CHI) methods [7]. In the final five experiments, including PCS-16, an additional current was driven on a center shaft, with the resulting safety factor (q) profile elevated so that $q > 1$ everywhere, similar to a spherical tokamak (ST) configuration (as in TS-2/TS-3 [8], SPHEX-Rod [9], HIT [10–12], NU-SpheroTok [13], and HIST [14]). In keeping with the MTF concept, the conductive compression liner acts as a close-fitting flux conserver that traps the magnetized plasma and stabilizes free-boundary MHD modes.

Previously published experimental results that explore what happens to a plasma as it is rapidly compressed have sparsely explored a very wide range of possible compression times and methods. There is a faster class of experiments in the 100 ns–10 μ s range often called Magneto-Inertial Fusion (MIF), an intermediary class of experiments compressing spheromaks in the 20–100 μ s range, and a slower class of experiments using tokamaks in the 2–15 ms range.

The faster class of experiments includes the FRX-L experiments where a Field Reversed Configuration (FRC) plasma is compressed with a Z-pinch-driven cylindrical liner [15, 16], a Z-pinch-driven spherical liner compressing a weakly magnetized plasma into the Mbar range [17], direct magnetic compression of an FRC (Helion [18]) and Z-pinch-driven compression of an axially magnetized plasma (MagLIF [19]).

Spheromak compression experiments other than in the PCS program have used direct magnetic compression, with primary examples being the inductively formed S-1 spheromak [20] with $\sim 100 \mu$ s compression time, and the CHI-formed SMRT spheromak [21] with a 20 μ s compression time. There was also a proposed plan to use high explosives (HE) to compress the CTX spheromak [22], which completed extensive studies of plasma formation in a non-mobile laboratory and performed preliminary demonstrations of $\sim 100 \mu$ s HE-driven liner implosions with no plasma. However, the two parallel efforts were never combined to compress a spheromak plasma with a mobile plasma formation system and a HE-driven liner.

A slower class of compressional heating experiments were performed on conventional tokamaks and used a rapid increase in the applied external magnetic field to compress the plasma. These include the ATC experiment [23–25], TUMAN-3 M [26], TOSCA [27], TFTR [28–30] and JET [31, 32]. The ATC experiment was designed specifically for this purpose, producing significant compression ratios and successfully demonstrating much of the basic concept. In faster experiments, direct diagnostic access is limited and MHD stability of the compressed plasma is not the focus of the project. In contrast, the tokamak experiments had very thorough diagnostic access. However, it has been many decades since that work was initially done because the primary goal of tokamak development has been steady-state operation, which favors heating methods such as neutral beam and RF heating. Following after these, General Fusion's PCS experiments have been the first to compress spheromak and ST plasmas with an imploding metal liner.

There are many advantages to a commercial pulsed fusion concept where compressional heating is accomplished with a metal liner. Liquid metal is a practical, economical method to input energy and to extract and utilize the fusion energy output [2, 4, 33, 34]. It enables high repetition rates, protects solid components, readily absorbs fusion energy, can be pumped through conventional heat-exchange systems, and can be manipulated with well-established industrial methods. Liquid lithium even breeds tritium when exposed to fusion neutrons, through fission of both ^6Li and ^7Li . However, for a physics experiment to study the behavior of a magnetized plasma during rapid compression, a simpler implementation of a single-use solid liner compression is highly desirable, which is the approach we have taken with the PCS program. Driving the compression with HE is a relatively inexpensive method to achieve a compression time in the intermediate range of 60–160 μs for a subscale experiment, which is predictive of an economically feasible compression concept when scaled up in size by roughly a factor of 5 in radius [35–42].

Experimental systems for PCS tests are built on a set of reinforced mobile containers to enable transport to the remote blasting range where compression experiments are performed. The system is designed to protect and reuse as many components as possible. We conducted 17 plasma compression tests in various configurations from 2012 to 2019. All tests successfully measured the key properties of the plasma with an extensive suite of diagnostics as it was being compressed. In pursuit of improved MHD stability and confinement, the plasma target was changed from a decaying spheromak to a sustained spheromak [43] and then to ST over the course of 17 tests. The compression liner was changed from bare aluminum to titanium-coated and then to lithium-coated aluminum in pursuit of improved wall interactions. Microdebris ejection is mitigated by diamond-turning the inner surface of the liner and then eliminating the leading-edge shock by including a vacuum gap between the aluminum outer surface and the inner surface of the surrounding plastic explosive charge [22]. Parallel to the experimental work, MHD simulations were used to model the plasma dynamics in two and three dimensions and make predictions for the occurrence of instabilities.

This paper will focus on the main results of PCS-16, which provided the clearest demonstration of MHD-stable compression on a timescale faster than the resistive decay time of the plasma. We begin in section 2 with a brief overview of relevant MTF theories that will be used to analyze our experimental results. Section 3 will describe the details of the mobile experiment and its operation. The measurements made during the PCS-16 plasma compression will be presented in section 4 and compared to the properties of our uncompressed ST plasmas, and basic expectations from theory and simulation. Interpretation of why the plasma behaved as observed will be discussed in section 5 through a comparison to MHD simulations and plasma stability analysis. Implications for future experiments will be discussed in section 6. Conclusions and directions for the application of these results in future work will be summarized in section 7. Supportive details of the methods and analysis will be provided in the appendices.

2. Theory of plasma evolution during MTF compression

MTF is an attractive concept because it has the potential to directly heat a plasma to fusion temperatures through compression, while geometrically increasing the plasma density to dramatically enhance the reaction rate. Because the method is pulsed, only short energy confinement times, on the order of the compression time, are required. The theoretic framework for MTF is typically explored via an adiabatic heating approximation, which is generally not realistic. Fully numerical simulations can include models that approximate realistic thermal losses but it is hard to extract general trends and physical insight where many effects are intertwined. To provide this physical insight we will outline some new analytic formulas to predict compressional heating in the case of realistic thermal losses, which can serve as a framework for interpreting experimental measurements presented in this paper as well as provide a basis for future studies in optimizing the MTF concept. The primary relation that needs theoretic clarification is how compressional heating depends on the ratio of thermal energy confinement time to compression time in a realistic scenario. We also address the question of how to maintain the plasma in a stable configuration that has good enough magnetic thermal confinement to enable significant heating to occur.

To provide a general guide to understand the foundations of the relevant physics, we briefly review some basics. Any MTF compression can be described in terms of a radial compression factor as a function of time, $C_R(t) = R_0/R(t)$ where $R(t)$ is the characteristic radius of the system and R_0 is its initial value. This is also referred to as a compression trajectory. Most practically achievable MTF concepts involve the compression liner moving significantly slower than the plasma Alfvén speed. Therefore, at each instant the plasma can adjust itself to maintain MHD force balance, always staying close to a Grad–Shafranov equilibrium [44] configuration. Within the framework of a stable, slowly evolving equilibrium there are several analytic results that provide useful insight into the

expected behavior of the plasma compression experiment, as described in section 2.1 and appendix A. However, due to realistic compression geometries deviating from perfect self-similarity, a more accurate description of MTF plasma compression can be found with numerical methods that take into account the spatial profiles and changing shape of wall geometry, as described in sections 2.2, 5.1, and 5.2.

The notation used throughout the paper for describing Grad–Shafranov equilibria will be to use $\psi(R, Z)$ for the poloidal flux function, in which the total magnetic flux passes through a circular loop of radius R at axial location Z , which has units of webers, while the alternate symbol $\bar{\psi}$ is a normalized poloidal flux coordinate with $\bar{\psi} = 0$ at the magnetic axis of the plasma and $\bar{\psi} = 1$ at the last closed flux surface (LCFS).

2.1. Non-ideal scaling with cooling and resistive flux loss

The general form of the compression-diffusion equation has a closed-form, self-similar solution that enables analytic exploration of the compression dynamics:

$$T(\rho, t) = T_0 C_R^2(t) \exp\left(-\frac{j_{01}^2}{a_0^2} \int_0^t \chi_E(t) C_R^2(t) dt\right) J_0\left(\frac{j_{01}}{a_0} C_R(t) \rho\right). \quad (1)$$

This solution for the evolution of the temperature profile $T(\rho, t)$ includes spatially uniform cross-field thermal diffusivity $\chi_E(t)$, with the plasma torus having minor radius $a(t) = a_0/C_R(t)$. We model the torus as a periodic cylinder with a minor-radius coordinate ρ , assume no loss of plasma particles ($n \sim C_R^3$), and spatially uniform density. In this solution $j_{01} = 2.4048$ is the first zero of the Bessel function J_0 , where T_0 is the central temperature at $t = 0$. A detailed derivation of this solution and its application is described in appendix A.

The time-dependent part of this solution contains two factors that work in opposition. The first factor $T_0 C_R^2(t)$ is the ideal (adiabatic) heating in the case of $\chi_E = 0$, while the second factor decreases exponentially with respect to the monotonically increasing time integral, thereby acting to bring down the temperature as the compression proceeds. The final behavior of overall heating or cooling depends the evolution and value of plasma $\chi_E(t)$ and the chosen compression trajectory $C_R(t)$.

Equation (1) can be integrated numerically in a straightforward manner, giving predictions of heating for a realistic compression trajectory when the value of overall thermal losses (modeled as a diffusion parameter $\chi_E(t)$) is assumed for the premise of a simulation or determined experimentally.

A simple analytic special case can be derived from (1) in the situation when χ_E is constant in time, and the trajectory obeys a particular formula. With these caveats it is possible to model departures from adiabatic compression with a scaling of the form:

$$T(t) = T_0 C_R^\epsilon(t), \quad (2)$$

where the exponent is limited to $\epsilon < 2$. For a class of compression trajectories of the form $R(t) = R_0 \sqrt{1 - t/\tau_C}$ this scaling

will hold exactly, for other slightly different trajectories this works as a reasonable approximation. In the case of ion compressional heating, the exponent is:

$$\epsilon = 2(1 - \tau_C/\tau_{Ei}), \quad (3)$$

where τ_C is the compression time, and τ_{Ei} is the initial thermal energy confinement time of the ions. This formula provides the simplest generalization to the Furth–Yoshikawa scaling [45], but the new formula includes realistic thermal losses rather than the overly optimistic case of perfect adiabatic compression. This formula can be used as a baseline metric to evaluate the possibility of significant heating by quantifying the ratio of the initial energy confinement time over the compression time τ_{Ei}/τ_C . The isothermal case of $\epsilon = 0$ will occur when $\tau_{Ei}/\tau_C = 1$. To achieve significant heating, this ratio must be several times unity, for instance to achieve $\epsilon = 1.5$ requires $\tau_{Ei}/\tau_C = 4$. It is often convenient to restate (3) as:

$$\frac{\tau_{Ei}}{\tau_C} = \frac{2}{2 - \epsilon} \quad (4)$$

which will give a minimum value of thermal energy confinement time for a given compression time necessary to achieve a certain heating exponent, provided that the plasma remains in a stable state throughout the compression. For electrons, collisions with ions can act as a significant heating term if $T_i \gg T_e$, and in the range of $T_e < 500$ eV Ohmic heating is significant and must be included in the power balance, increasing the complexity of how T_e scales with compression. These effects are included in the discussion of electron temperature measurements in section 4.4. The zero-dimensional formula for the Ohmic heating power for a plasma with major radius $R_{\text{axis}}(t)$ and minor radius $a(t)$ is:

$$P_\Omega = \frac{a^2(t)}{2\eta(t)R_{\text{axis}}(t)} \left(\frac{d\psi(t)}{dt}\right)^2. \quad (5)$$

The poloidal magnetic flux ψ within resistive plasma decays with a flux decay time $\tau_\psi = \mu_0/\eta\lambda^2$ [46]. Here, λ is the magnetic eigenvalue (for spherical system $\lambda(t) = 4.493/R(t)$) which in general scales as $\lambda \sim C_R(t)$, and η is the plasma resistivity which scales according to Spitzer formula, $\eta \sim T_e^{-3/2} \sim C_R^{-3\epsilon/2}$. In the case where electron heating can still be described by $T_e(t) = T_e(0)C_R^\epsilon(t)$, where ϵ may depend on more quantities than in (3) due to Ohmic and ion-thermal terms, the poloidal flux will have a time dependence of:

$$\psi(t) = \psi_0 \exp\left(-\frac{1}{\tau_{\psi 0}} \int C_R^{2-3\epsilon/2} dt\right), \quad (6)$$

where $\tau_{\psi 0} = \tau_\psi(0)$ is the initial value of the flux decay time. A useful reference case for the scaling of the Ohmic heating power is the isothermal case where $\epsilon = 0$ and η is constant:

$$P_\Omega = \eta \left(\frac{\psi_0 \lambda_0^2}{\mu_0}\right)^2 \left(\frac{a_0^2}{2R_{\text{axis}}(0)}\right) C_R^{3-4\tau_C/\tau_{\psi 0}}, \quad (7)$$

which is arrived at by combining (5) and (6) and using the power-law heating trajectory $C_R(t) = (1 - t/\tau_C)^{-1/2}$ to evaluate and simplify the integral term for the case of $\varepsilon = 0$. This will provide an upper bound for Ohmic heating power for a range of cases where $\varepsilon \geq 0$ where net heating is occurring. It is instructive to compare that to the compressional heating power for electrons, again for the isothermal limiting case, is given by:

$$P_{\text{comp}, e} = 3 \langle n_{e0} T_{e0} \rangle_V V_0 C_R^{-1}(t) \left(\frac{dC_R}{dt} \right) = \frac{3 \langle n_{e0} T_{e0} \rangle_V V_0}{2\tau_C} C_R^2(t), \quad (8)$$

where the final expression is simplified via the relation (24) for power-law heating trajectories, and $\langle n_{e0} T_{e0} \rangle_V$ is the volume-averaged initial electron pressure, and V_0 is the initial volume. This provides a lower bound for compressional heating in a range of cases $\varepsilon \geq 0$. A quantitative comparison of these heating terms will be presented in the context of the experimental data in section 4.4, and the general formulas for arbitrary values of ε , extending beyond the isothermal case, will be provided in appendix A.

The resistive loss of flux (6) will be observable via the time-evolution of the poloidal field such that for spherical self-similar compression, Lagrangian advection of the fields gives a magnetic compression factor

$$C_B(t) = \frac{B_{\text{pol}}(\vec{x}, t)}{B_{\text{pol}}(C_R(t)\vec{x}, 0)} = C_R^2(t) \frac{\psi(t)}{\psi_0}. \quad (9)$$

This will be used in section 4.2 to estimate the poloidal flux decay and infer a lower bound on the electron temperature. Geometries that depart from self-similar compression (such as our PCS tests) will have a more complex relationship between flux and magnetic field and require two-dimensional equilibrium modeling to numerically evaluate the geometric scaling factor, which is elaborated on in section 4.3.

The dependence of plasma flux conservation on the rate of temperature rise is strong enough that magnetic measurements during compression experiments can, in principle, provide constraints on the magnitude of thermal losses. However, in practice, confounding effects exist, such as the possibility of impurity increase causing resistive loss due to the Z_{eff} dependence, as well as possible changes in the radial profile of plasma current that changes the magnetic field at the edge of the plasma volume without changing the flux ψ , and so it is important to have a complete diagnostic program that directly measures $T(t)$ and $n(t)$. The final conclusions we present in this paper are a synthesis of all available diagnostic data taking into account the different limitations of each method.

2.2. MHD stability during compression

The compressional heating of the plasma will deviate from the scaling law (2) with a constant ε value if the magnetic structure becomes disordered, causing radial thermal transport to increase during compression. For an intermediate-timescale

MTF concept, it is important to maintain the plasma in a configuration that is MHD stable or at least has instabilities that grow much slower than the compression rate. Ideal MHD instabilities grow on the Alfvén time, so they are always deleterious over the compression time scale. Resistive MHD instabilities are due to magnetic reconnection (i.e. tearing and interchange) occurring at resonant surfaces so they have growth rates which are much less than ideal MHD instabilities, but they must also be considered. Due to the stabilizing influence of a flux conserving metal wall in close proximity to the plasma boundary, we have conducted a linear analysis, without including the effect of free-boundary modes, as a baseline study of internal stability. The presence and growth rate of instabilities depend on details of the underlying equilibrium, such as magnetic curvature, current density profile and the corresponding safety factor $q(\psi)$ profile, as well as pressure.

Tokamak configurations tend to have stabilizing field line curvature on the inboard or high-field side of the poloidal cross section, and destabilizing curvature on the outboard or low-field side. It is for this reason that modern conventional tokamaks, such as DIII-D [47] and ITER [48], are designed with D-shaped cross sections, placing more poloidal extent on the inboard side of the cross section. The flux conserver in the PCS experiments (figure 1) differs from a typical D-shaped tokamak cross section because the dynamic compression geometries must be implemented by smoothly deforming an aluminum shell without buckling or tearing and require a center shaft that is shaped to trap the plasma deep into compression without intersecting the trajectory of the imploding metal liner.

In previous numerical studies [49, 50], we analyzed a simplified MTF device geometry undergoing compression and found that a stable scenario exists given carefully chosen plasma profiles and shaping. This result is promising and informative for how to design MHD stability during compression.

The $q(\psi)$ profile is the leading factor for determining stability and can be defined as $q(\psi) = d\Phi/d\psi$, which is conserved in ideal MHD because the toroidal flux Φ contained within each poloidal flux surface ψ is constant in time (both fluxes being frozen to the plasma mass). Hence, the q profile can only change due to resistive flux diffusion/loss. However, during rapid compression that is close to ideal, in order for q to be conserved MHD forces may drive significant changes to plasma shape, deviating from self-similarity, if external forces are not applied in a way that tracks the increasing internal forces. Rapid changes in plasma shape in the direction perpendicular to the wall are passively stabilized by reaction currents induced by the conductive wall, however axial motion is possible and is not constrained to be perfectly axisymmetric, and therefore can be an opportunity for instability.

The concave geometry of the flux conserver and poloidal field line tension provide an obstacle against axial motion back into the annular opening of the Marshall gun, however this barrier can be overcome if there is a sufficient difference in toroidal magnetic pressure between the plasma interior and the gun region. During compression, the coaxial inductance of the compression chamber decreases rapidly, this dramatically

increases toroidal magnetic pressure within the compressed plasma, while the inductance of the gun is unchanged and therefore does not pressurize in the same way. To maintain the axial balance of toroidal magnetic pressure, we apply a ramp of additional shaft currents from an external circuit to keep the plasma well confined within the collapsing volume of the compression region and minimize the potential for axial instabilities that could damage thermal confinement.

The external circuit as implemented on PCS-16 has a finite capacity and is only able to track the required ramp rate for toroidal pressure balancing up until $t = 385 \mu\text{s}$ when the compression ratio reached $C_R = 1.35$. After that point, the internal toroidal magnetic pressure in the plasma begins to climb above the magnetic pressure in the gun until a threshold for instability is crossed. This behavior can be understood and explored via nonlinear MHD simulations, as described in section 5.2. It should be noted that in a reactor-scale MTF configuration, such as with a liquid metal liner, where the poloidal circuit can be completed by the liner, the external shaft ramp will no longer be required and the shaft current will increase as a result of toroidal flux conservation during compression of the plasma.

In addition to these potentially strong ideal instabilities arising from axial displacement of the plasma boundary, resistive evolution of the q profile can lead to the appearance of slowly growing unstable modes that can also increase core thermal transport. It is anticipated that various instabilities might be possible and so we designed the experiment to make magnetic measurements at six toroidal angles to allow detection of toroidal variations of poloidal field strength at the wall, determining the amplitude of mode numbers $n = 1, 2, 3$ and the phase of $n = 1, 2$ which can indicate the nature of MHD instabilities if they emerge. The Mirnov probe measurements we present in section 4.7 show the onset of MHD modes that promptly affect thermal confinement, as indicated by several independent measures of temperature, as described throughout section 4. This is in general agreement with known expectations, and shows how the same theory can be used to produce MTF designs which are MHD-stable throughout compression.

3. PCS on a mobile platform

The goal of MTF is to use an imploding metal liner to heat a magnetically confined plasma in fusion conditions that requires a physical separation between the static plasma formation system and the compression system. Conventional designs for tokamak formation do not allow for this separation because the plasma is fully surrounded by components that are not compatible with a linear compression system. However, an efficient alternative design can be found based on the concept of CHI formation of plasma toroids, which naturally provides axial separation by having a coaxial formation system (magnetized Marshall gun) that injects a plasma ring across a distance into a separate flux conserving compression system. Rather than initiating plasma poloidal flux with an inductive solenoid in the center shaft like conventional tokamaks, in the PCS-16 device, the lower Marshall gun section

has been designed to generate an initial bridge of radial magnetic flux that links the inner formation electrode to the outer vessel wall, creating this initial flux from a combination of one internal DC coil contained within the formation electrode and two external DC coils just below the compression region. The cross section diagram of the device in figures 1 and 2 shows a photograph of the upper flux conserver section into which the plasma is formed.

A representation of the DC magnetic field lines and the resulting plasma equilibrium are shown in figure 1. For enhanced ionization, the DC magnetic field also includes an electron Penning trap region near the gas valves consisting of looped field lines that terminate at the negatively charged formation electrode on both ends. Deuterium gas was injected through a set of eight custom-made fast opening piezo valves located midway up the outer vessel, forming a cloud that would become ionized when negative 14 kV was applied to the formation electrode. Just below the gas valves were a set of vacuum ports through which the vessel was maintained at a pressure of 3×10^{-7} Torr via a turbo-molecular pump and dry scroll pump.

Prior to plasma breakdown, the current was also driven on a separate central shaft creating a pre-existing toroidal component to the field. Once an electrically conductive plasma was bridging the radial gap between the formation electrode and the outer vessel, a larger formation capacitor bank was discharged through the plasma bridge, which pushed the plasma rapidly upward via $\vec{J} \times \vec{B}$ force, carrying with it the embedded pre-existing poloidal and toroidal magnetic fluxes. This process constitutes the fast-CHI formation method, in which the ST plasma is formed in $50 \mu\text{s}$. The displacement of poloidal flux induces a large toroidal plasma current (typically 300 kA) and the act of expanding into a larger spherical volume provides the opportunity for the distended poloidal field lines to reconnect with themselves forming closed poloidal flux surfaces of the main ST plasma.

All plasma-facing electrode surfaces in the Marshall gun section and instrumented center shaft were coated during manufacturing with $\approx 200 \mu\text{m}$ of low-porosity plasma-sprayed tungsten, which significantly increases the durability of the electrodes. An important feature of the SPECTOR style of Marshall gun used in PCS-16 is that the radial separation between the inner and outer electrodes increases as the conical outer radius decreases, resulting in a 'downhill λ ' configuration [6] that improves the plasma formation efficiency. Another beneficial design feature is a large-volume vacuum gap that electrically isolates the formation electrode from the center shaft within it. This evacuated gap enables a natural exhaust path for electrode impurities that are generated when the formation current reaches the top edge of the formation electrode and is forced to continue through a plasma arc between the electrodes. The annular plasma arc slowly erodes the tungsten-coated electrode surface at that axial gap; however, the current path through the plasma bridge is configured to behave as a Z-pinch with magnetic forces driving any ablated material toward a smaller radius into the gap and then down along the central shaft, away from the main plasma chamber. The vacuum gap feature and Z-pinch

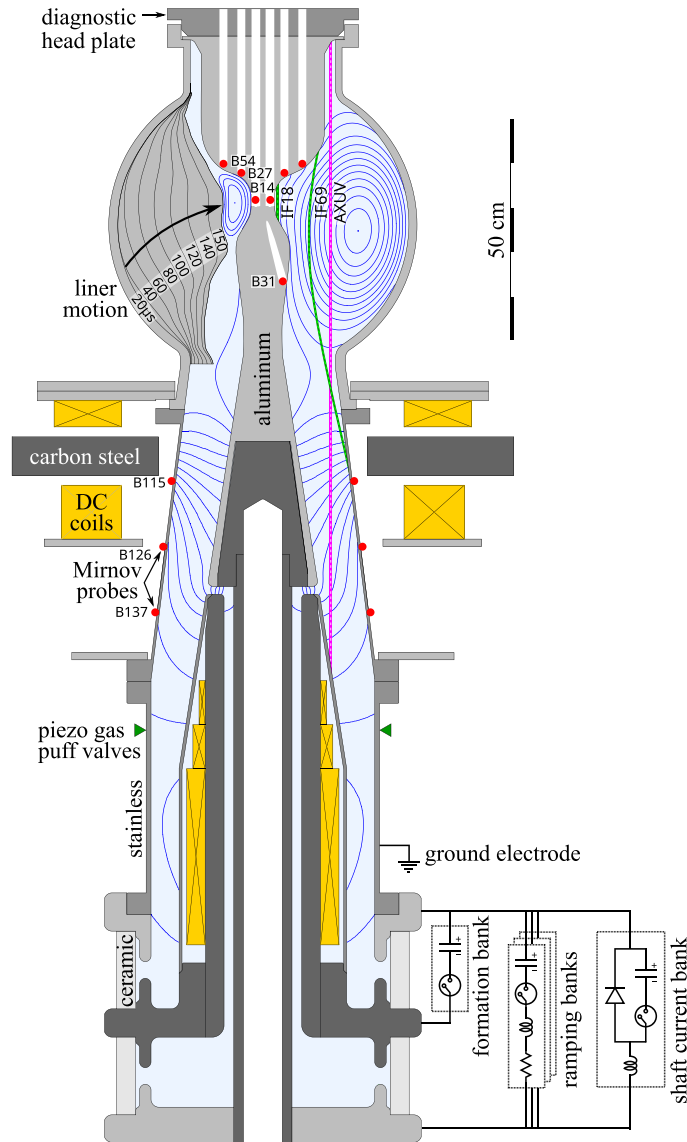


Figure 1. Cross section of the PCS-16 device. Metal components are axially symmetric, but the uncompressed flux conserver geometry is shown on the right and compression trajectory (labeled as liner motion) up to $150\ \mu\text{s}$ is shown on the left. Magnetic flux surfaces appear as blue curves with spacing of $0.5\ \text{mWb}$, except in the compressed toroid where the spacing is $1.5\ \text{mWb}$. Mirnov probe locations indexed by radial coordinate in mm (B14, B27, B31, B54, B115, B126, B137) appear as red circles. Interferometer chords (IF18, IF69) appear as dotted green lines. The primary optical diagnostics (AXUV, ion Doppler spectroscopy, visible spectroscopy) have chords illustrated as a dotted pink line, these are axial chords at different toroidal locations. The driving circuit is shown at lower right. The formation capacitor bank, ramping capacitor bank, and shaft capacitor bank connected through a large inductor are shown in separate boxes.

effect enables the PCS-16 device to operate with relatively low metallic impurity content in the main plasma and correspondingly higher electron temperature.

The final component of the vacuum vessel is the upper aluminum spherical chamber which acts as a passive flux conserver to confine the poloidal field of the ST plasma. Current driven up the central shaft and returning down along the axisymmetric outer aluminum wall acts as a single-turn toroidal field coil with negligible error fields, serving to provide enough toroidal flux to stabilize the plasma with $q > 1$. Lithium evaporators were used to coat the surface of an aluminum spherical chamber and a central shaft with a thin layer of solid Li ($0.1\ \mu\text{m}$) providing a strongly gettering plasma facing the surface. The spherical aluminum flux conserver

section is also called the liner in the MTF context because it is rapidly compressed with symmetrically detonated HE, in turn compressing the plasma toroid. In order to prevent the inner surface of the aluminum liner from ejecting material into the plasma during compression, it requires high ductility; therefore, it is the one surface that is not coated with brittle tungsten. The lithium coating on the Al liner works as a low-Z plasma-facing material to prevent Al ablation.

There are five capacitor banks connected to the machine to generate toroidal field: a shaft current bank ($2.1\ \text{mF}$, $14\ \text{kV}$), a formation bank ($1.4\ \text{mF}$, $16\ \text{kV}$), and three ramping banks to rapidly increase the shaft current during compression ($236\ \mu\text{F}$, $236\ \mu\text{F}$, and $472\ \mu\text{F}$, all at $18\ \text{kV}$). The shaft current bank is in parallel with a set of crowbar diodes, connected through

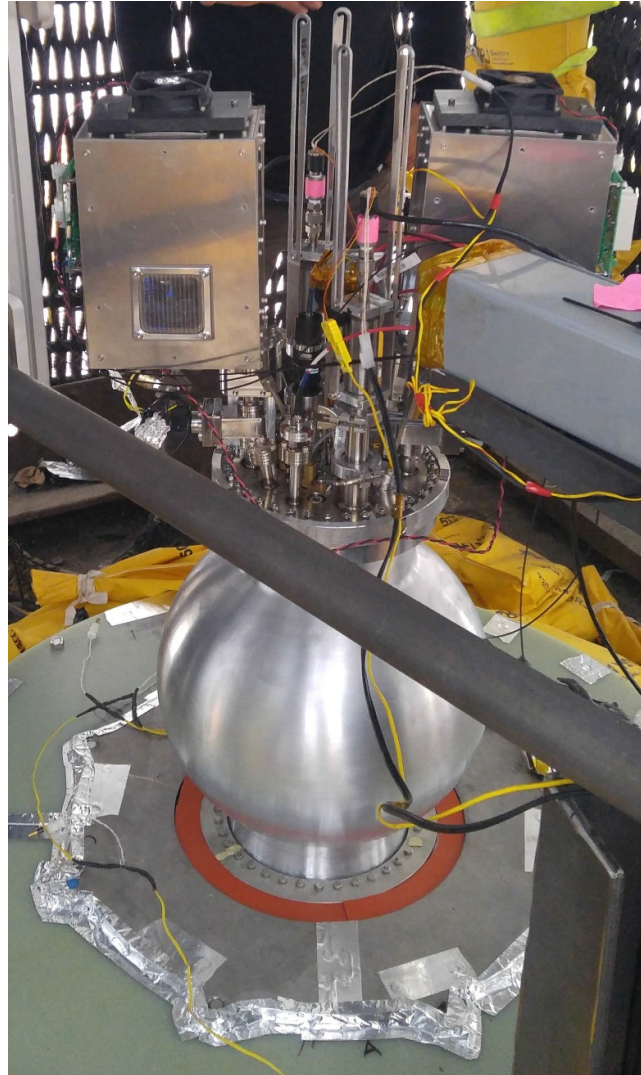
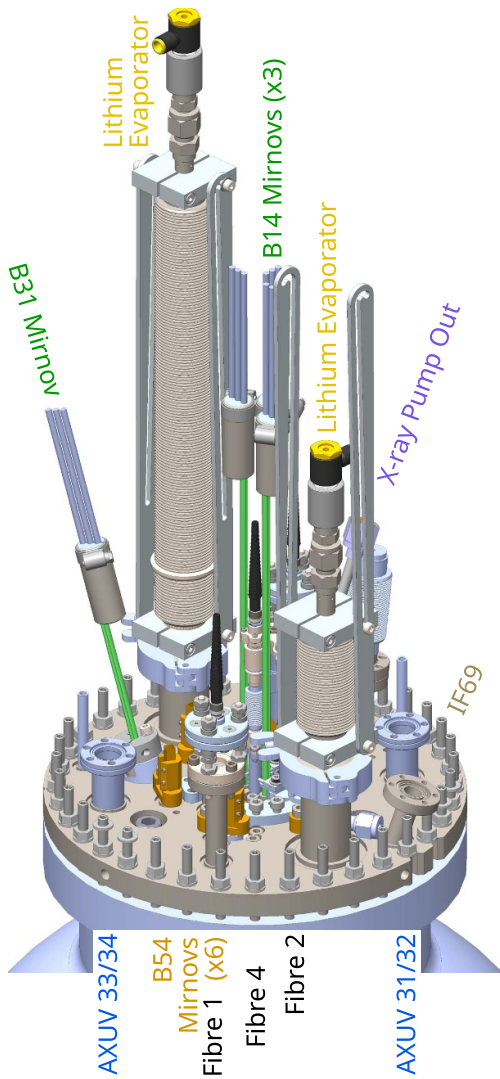
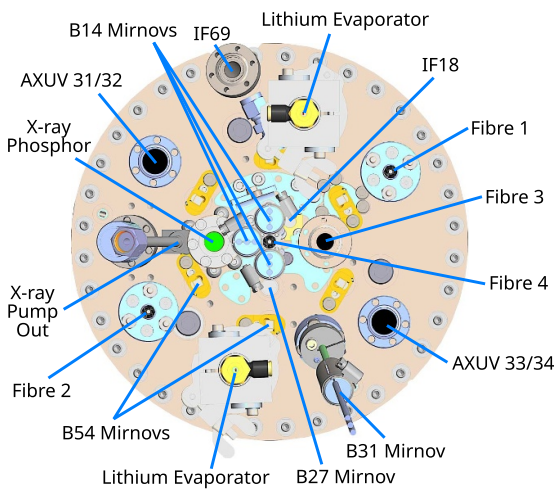


Figure 2. Photo of PCS-16 assembled in the field prior to the addition of high explosives, showing both the flux conserver and diagnostic head plate. The visible diagnostics are labeled on the adjacent diagram. A more comprehensive top-down view is shown in figure 3.



<p>Fibre 1 (R=88 mm, 120 deg): Ion Doppler Spectrometer G</p>	<p>Fibre 3 (R=35 mm, 90 deg): Ion Doppler Spectrometer H Octo Fibre: Spectrum 7: 0–435 μs Spectrum 6: 300–450 μs Unfiltered Photodiode 2 FS 6 = 280 nm (Mg II) FS 7 = 656 nm (H-α) FS 8 = 550 nm (Li II) FS 9 = 671 nm (Li I) FS 10 = 486 nm (H-β)</p>
<p>Fibre 2 (R=88 mm, 300 deg): Octo Fibre: Spectrum 0: 0–290 μs Spectrum 1: 270–330 μs Spectrum 2: 290–350 μs Spectrum 5: 330–355 μs Spectrum 4: 345–365 μs Spectrum 3: 360–420 μs Unfiltered Photodiode 1 Octo Fibre: FS 11 = 486 nm (H-β) FS 12 = 280 nm (Mg II) FS 13 = 671 nm (Li I) FS 14 = 656 nm (H-α) FS 15 = 550 nm (Li II)</p>	<p>Fibre 4 (Center Mirror): Octo Fibre: FS 1 = 656 nm (H-α) FS 2 = 671 nm (Li I) FS 3 = 550 nm (Li II) Unfiltered Photodiode 4 FS 5 = 280 nm (Mg II)</p>

Figure 3. Top view of the diagnostic head plate with a list of optical diagnostics attached to fibers. FS denotes a Filter Scope, IF18 and IF69 denotes the two interferometer chords. See figure 1 for the cross section view of diagnostics in relation to the plasma.

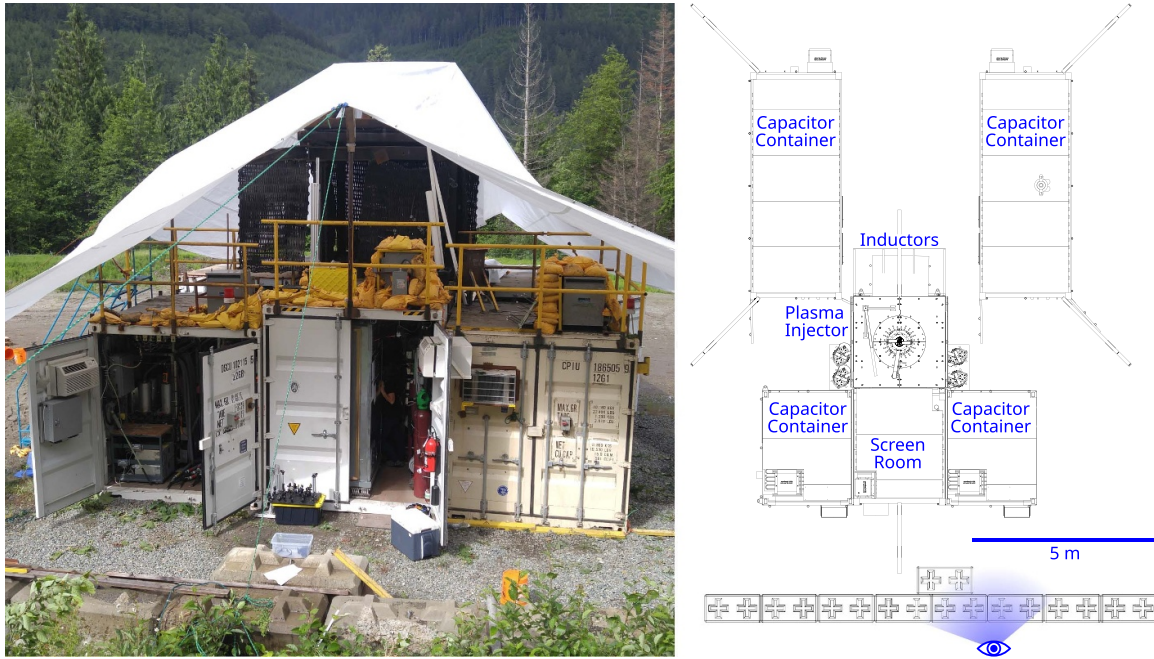


Figure 4. (Left) Photo of PCS-16 configured at the test site. Five customized containers were required to house and transport the capacitors and other equipment from the lab. (Right) Top view of site layout showing location of each container and labeled with its contents.

a large inductor which acts to keep the shaft current as constant as possible prior to compression. Refer to figure 1 for more details. The ramping banks were connected to the vessel shaft via a pulse-shaping network. Their purpose is to maintain toroidal pressure and MHD balance during compression. The three capacitor modules were fired in a timed sequence of additive pulses that closely approximate the theoretic ramp that ensures toroidal flux neither moves into or out of the compression chamber, as described in section 2.2.

The apparatus for the PCS experiments was constructed in a modular manner so that they could be commissioned in a laboratory environment and then transported to the field for the plasma compression shot. In order to optimize the plasma performance for a compression shot, the experimental operation was divided into two phases of activity. First, there was a longer sequence of in-lab commissioning, diagnostic calibration, wall cleaning shots and a campaign of the fine-tuning of control parameters for forming ST plasma discharges, which could span several months to up to a year. The in-lab campaign was conducted on the same containerized hardware that could be moved to the field once the decision was made to do so. The second and final in-field phase leading up to the compression shot typically requires roughly 1 week for disconnection of modules and transport to the field, and a final week is allotted for experimental operation in the field, culminating in the compression shot.

The HE-driven compression of an ST plasma was performed at a private blasting range in the mountains of southern British Columbia [35]. To facilitate transport, the MRT2 (Magnetized Ring Test-2) mobile experimental platform used for PCS-13 to PCS-17 was housed in five blast-reinforced shipping containers: two 20 ft and two 10 ft containers for

pulsed power capacitor banks and one 10 ft container for control computer, diagnostic lasers and data acquisition screen room, see figure 4. The plasma vessel was supported within a central custom-built cubic steel frame that experienced four blasts unharmed.

Once lab operations were determined to yield optimal plasma performance, the electrical cables between containers were disconnected and diagnostics were stowed for shipping. The logistics of disassembly, transport to the field, and reassembly in the mountains were implemented in the span of 1 week. This was followed by a recommissioning sequence of plasma shots in the field that took to 4 days to complete, followed by installation of a high-explosive charge on day 5 for the plasma compression shot.

An important contributor to the reliability of the plasma compression system is an FPGA veto logic circuit. This circuit was enabled on candidate plasma compression shots such that HE detonation was only triggered when the plasma properties measured during the first $50 \mu\text{s}$ after formation met predetermined performance criteria. The FPGA veto circuit performed real-time evaluation of threshold and ratio conditions on inputs from Mirnov and AXUV diagnostics and outputted a latched Boolean go/no go signal that was ANDed with a second trigger signal (of adjustable timing) from the LabView control system, and then it was the output of the AND gate that would trigger the HE detonation circuit. This second operator-controlled trigger signal would only be enabled when we were fully ready to attempt a compression shot, and the time of this trigger was set to $t = 300 \mu\text{s}$ for PCS-16 based on previous in-lab studies indicating what seemed like the most quiescent period to begin the compression with the HE driven liner. This veto system is a valuable tool to ensure that compression is never triggered

in the case of a plasma formation misfire or the random occurrence of substandard plasma performance.

To define the terminology we will use throughout this paper, when describing the compression trajectory, we will refer to the moving outer wall as the ‘liner’, the start of compression as the time of the ‘liner move’ and the completion of compression as the ‘liner contact’ when the liner first contacts the metal of the inner shaft.

3.1. Plasma diagnostics

Diagnostic ports could not be placed on the aluminum compression liner since it is needed to maintain mechanical symmetry to high precision during implosion. Generally, that leaves only the upper and lower regions at small angles away from the z -axis for implementing access through a diagnostic ‘head plate’ (see figures 1–3). This head plate contained a wide set of plasma diagnostics: an array of flush-mount Mirnov coils for measuring poloidal and toroidal magnetic fields, ports for passive measurement of plasma emission in the visible (time resolved spectroscopy and filterscopes [51]) and soft x-ray (absolutely-calibrated extreme ultraviolet photodiodes, AXUV), density measurement with two vertical interferometry beams, ion Doppler spectroscopy (IDS) and a filtered pinhole camera for fast imaging of hard UV and soft x-ray plasma emission (aluminum-filtered phosphor imaged with Phantom camera via optical fiber bundle). The high-speed video obtained using the soft x-ray phosphor pinhole camera showed no anomalous events; however, the full description of its analysis is beyond the scope of this paper. The Mirnov probes are arranged in toroidal arrays in the shaft and we refer to them by their radial coordinates in mm: B14 ($\times 3$), B27 ($\times 1$), B31 ($\times 1$), B54 ($\times 6$). There are also toroidal arrays of Mirnov probes on the outer wall of the injector: B115 ($\times 4$), B126 ($\times 4$), B137 ($\times 4$). Interferometer chords are also labeled by their (minimum) radial location in mm: IF18 and IF69. Vertical IDS chords were located at $R = 88$ mm (IDS G) and $R = 35$ mm (IDS H). See figure 3 for the physical arrangement of these diagnostics.

Experimental campaigns conducted in parallel with a non-mobile second copy of the experimental device (named SPECTOR-1) had additional diagnostics that made use of horizontal chords via ports on the instrumented outer flux conserver, allowing for multi-point Thomson scattering T_e measurements, additional interferometry, and polarimetry chords [52] as well as more comprehensive spectroscopy to characterize the noncompressed plasmas. These in-lab characterizations provide valuable constraints for developing realistic models of the PCS plasma configurations.

3.2. PCS-16 compression shot

The PCS-16 compression shot (MRT2-13 893) was completed in June 2018 and successfully achieved the compression of a CHI-formed ST plasma composed of deuterium.

In the preparatory phase of noncompression shots in the lab leading up to the PCS-16 compression shot in the field, the

plasma performance was optimized in various ways building off the guidance from previous builds of the experiment. The highest performance shots used peaked current profiles that resulted in good precompression stability and were achieved using a double-pulse current waveform for the shaft current. In the double-pulse method, the shaft current was first ramped to 200–300 kA before plasma breakdown, and then the formation current pulse was fired, coincident with a second ramp of shaft current to 500–600 kA. This method generates a more peaked plasma current profile, as indicated by a smaller ratio of polar to equatorial B_{pol} . The magnetic energy of the plasma after formation was nominally 0.96 kJ poloidal, 17 kJ toroidal while thermal energy is in the range of 350 ± 25 J. Plasma equilibrium was a low- β state with $\beta_{\text{tor}} \sim 4\%$ and $\beta_{\text{pol}} \sim 15\%$. The magnetic configuration is adjustable with vertical field coils just below the spherical flux conserver to create an x-point junction with the gun flux. However, resistive diffusion into the flux conserver quickly led to a configuration that was limited to the outboard equator, see figure 1.

It was found that the optimal recipe also required firing after a very recent lithium coat and using an unusually long delay between opening the gas valves and firing the formation capacitors. For the PCS-16 sequence of shots we used a pair of retractable, nearly Omni-directional ($\Omega = 3.5\pi$ sr) lithium coating evaporators (see figure 3). These were run at 600°C for 10–15 min, during which a layer of lithium approximately $0.1 \mu\text{m}$ thick is deposited on the flux conserver and inner electrode of the compression region. The first ~ 10 plasma discharges immediately after the Li coating exhibits the benefits observed from ‘fresh’ lithium, i.e. longer magnetic lifetimes, favorable MHD evolution, smooth density evolution, and high T_e .

A key component of the PCS-16 shot was the shaft current ramp applied during compression. Figure 5 shows this shaft’s current ramp. A significant physics objective of PCS-16 was to determine what happens when the external circuit is depleted and the plasma is less constrained during rapid compression. In the PCS-16 device, due to the nature of the coaxial geometry and deformation mechanics of the solid liner, the radial gap connecting the flux conserver and the gun remains open during compression up to $C_R = 4$. The theory in section 2.2 suggests that the PCS-16 plasma is likely to undergo a free-boundary instability, which could cause poor thermal confinement, when the shaft current is no longer sufficient. As previously noted, once the liner closes off the entrance to the gun by metal-metal contact (which occurs on the PCS-16 compression at $t = 460 \mu\text{s}$) the external ramp of shaft current would no longer be needed and the poloidal loop of shaft current within that closed volume would increase due to conservation of toroidal flux within a rapidly compressed coaxial inductor, resulting in stable support of the q profile, as required by the theory of section 2.2, without a continued external supply. This can be seen in the final rapid increase in shaft current at late time $t > 460 \mu\text{s}$ as measured by the toroidal Mirnov probes on the shaft within the closed plasma volume, as shown with the ‘Shaft through plasma’ current trace on figure 7(b). We also show that it is possible to accomplish toroidal flux trapping

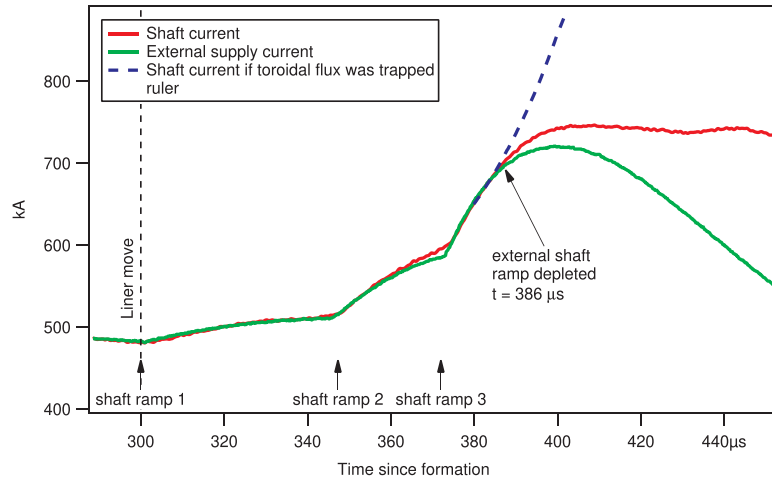


Figure 5. An external power supply with 3 pulses (the first at the liner move, followed by shaft ramp 2, and shaft ramp 3) increases the shaft current during compression to ensure that toroidal flux neither leaves nor enters the compression chamber, until it is depleted.

within the compression volume if the radial gap between the liner and the shaft becomes so narrow that the poloidal circuit becomes closed by the current flowing in an arc formed through the edge plasma. Such a possibility would enable MHD stability without metal–metal contact.

3.3. Implosion kinematics

In the context of applying the power-law heating formalism from section 2.1 to provide a quantitative analysis of the temperature evolution in PCS-16 we will make use of the fact that the experimental trajectory closely agrees with the theoretic formula (25): $C_R(t) = (1 - (t - t_0)/\tau_C)^{-1/2}$ with best fit parameters of $t_0 = 324 \pm 1.7 \mu\text{s}$ and $\tau_C = 139 \pm 1.8 \mu\text{s}$. In the experiment there was an early phase during the first $24 \mu\text{s}$ after the liner began to move, during which compression was relatively slow to accelerate. After $t_0 = 324 \mu\text{s}$ the compression proceeded more rapidly, fitting the power-law heating trajectory to within 4% maximum relative error (1.4% mean relative error). For any analytic estimate we will use $\tau_C = 139 \mu\text{s}$ as the characteristic compression time for PCS-16. To facilitate further study of the PCS-16 experiment, we have included as a data supplement¹ a set of csv files that define the geometry of the poloidal cross section of the interior region between the center shaft and the moving liner as a function of time, in $5 \mu\text{s}$ increments starting at the beginning of liner motion. The inner surface curve of the liner geometry is based on 16 poloidally distributed, simultaneously measured, photon Doppler velocimetry (PDV) beams [53] during a sequence of test implosions and solid-mechanics deformation simulations using Ansys LS-DYNA that match the PDV data.

The toroidal symmetry of the inner surface of the aluminum liner at the moment of contact with the shaft can be determined by looking at the variation in time when the six Mirnov signals at the $R = 54 \text{ mm}$ probe locations become flatlined. These

reveal an average time of the liner contact of $460.37 \mu\text{s}$ with the earliest contact at $459.9 \mu\text{s}$ at $\phi = 240^\circ$, and a last contact at $460.7 \mu\text{s}$ at $\phi = 60^\circ$, consisting of a dominantly $n = 1$ toroidal mode structure. This constitutes a peak–peak amplitude in the contact timing variation of $(t_{\text{max}} - t_{\text{min}})/2 = 0.4 \mu\text{s}$. The velocity component of the liner normal to the shaft surface was determined from PDV measurements and LS-DYNA deformation simulations to be 874 ms^{-1} at the $R = 54 \text{ mm}$ location. This translates to a surface deviation from axisymmetry having an amplitude $\delta R = (R_{\text{max}} - R_{\text{min}})/2 = 0.35 \text{ mm}$. This constitutes clear evidence that liner buckling was avoided within a $\delta R/R = 0.65\%$ level of relative surface deviation at an overall compression ratio of $C_R = 4.2$. The simplest explanation of an $n = 1$ shift by 0.35 mm is due to concentricity errors in the assembled components which have a radial tolerance stack-up of $\approx 0.5 \text{ mm}$ between shaft and liner when assembled.

4. PCS-16 results

In this section we present the experimental results from the compression shot and build a coherent picture of the behavior observed during the rapid compression. The plasma properties of the PCS-16 shot are compared to a set of prior noncompression shots performed under similar conditions on the same device.

As motivated by section 2.1, the degree to which poloidal flux is conserved can be a useful way to indicate how well thermal confinement is maintained during compression. The fact that PCS-16 was a very successful plasma compression is clear when we examine the progression of improvements over the PCS campaigns, as shown by the relative increase in poloidal magnetic field shown in figure 6. The poloidal magnetic signals are normalized at the time of liner movement and plotted with $t = 0$ set to be the start of each compression. Each trace is the toroidal average of a set of poloidal Mirnov probes at $R = 27 \text{ mm}$ (B27, figure 1), or the nearest equivalent position for that device.

¹ See supplemental material online at (<https://doi.org/10.1088/1741-4326/ad9033>).

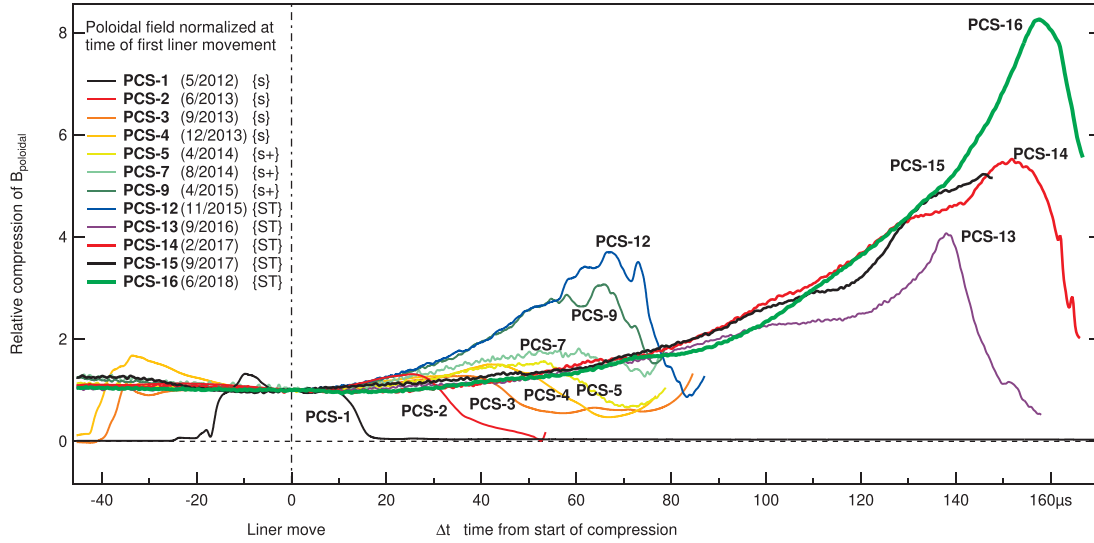


Figure 6. Summary of progression of significant PCS shots. This shows normalized poloidal magnetic field near the $R = 27$ mm position being compressed during the shots of significance. PCS-1 to PCS-4 compressed decaying spheromak plasmas {s}, PCS-5 to PCS-11 compressed sustained spheromaks {s+}, PCS-12 to PCS-17 compressed spherical tokamak plasma configurations {ST}. The campaigns with $80 \mu\text{s}$ compression used a 29 cm internal diameter cylindrical liner imploding in a hyperboloid deformation, while the campaigns with $160 \mu\text{s}$ compression used the 38 cm internal diameter spherical liner shown in figure 1. For simplicity and readability only PCS shots showing incremental improvement are included in this plot.

Before presenting the details of the methods and results, we first provide an overview of the key points. A compact summary of the primary diagnostic signals is shown in figure 7. The major results from the PCS-16 experiment are as follows:

1. Density compression is very clean and follows the model for particle conserving volumetric compression deep into the compression (figure 9), up to a measured increase of 188 times its starting value, going from $1.2 \times 10^{14} \text{ cm}^{-3}$ to $2.3 \times 10^{16} \text{ cm}^{-3}$. The details of the results and analysis are described in section 4.1. The angled interferometer beam (IF69) measures the early time behavior before compression and will observe the core of the plasma as it is pushed across the beam during the compression. The trend of volumetric compression of density determined by IF69 continues to hold when the plasma is compressed into the pocket region and can be measured by the inner IF18 beam, with very good continuation to the original trend as late as $465 \mu\text{s}$, only $10 \mu\text{s}$ before completion of compression with liner contacting the central shaft. The plasma density profile that best matches the observed signal is a flat plateau with a drop in electron density near the wall.
2. Magnetic field compression was better than any previous test, as shown in figure 6. Not only does the data show that the poloidal field is compressed to higher values relative to the starting value but the evolution is much smoother, without the plateaus and other features present in previous shots. The signals from the inner-most Mirnov probes at $R = 14$ mm (B14) show the existence of a highly compressed, magnetized plasma toroid with a significant fraction of its original poloidal flux remaining at $160 \mu\text{s}$ into compression, reaching a radial compression ratio of $C_R =$

8.65, with details of the results and thermal implications discussed in sections 4.2, 4.3 and appendix D.

3. Measurements of plasma temperature are relatively flat with time or show a moderate increase during the first two-thirds of the compression (from 300 to 410 microseconds), with $T_i(t)$ from neutron yield and the lower bound from IDS both showing a slight rise, while $T_e(t)$ from filtered AXUV ratio shows a mostly flat trend in comparison to a slight rise on the T_e lower bound from the flux decay estimate. All temperature metrics agree that starting at $t \approx 410 \mu\text{s}$ the plasma temperature rapidly decreases in a measurable way for the remainder of the compression. The details of these temperature measurements are described in sections 4.4–4.6.
4. We observed a significant increase in the neutron count rate during the first two-thirds of compression as seen in figure 8. This constitutes a four-sigma increase above the average rate for a noncompressed plasma of similar properties. The increase in neutron output was consistent with slightly increasing ion temperature while plasma density increased by a large factor. Details of the analysis of scintillator data are described in section 4.6.
5. The best estimates for the core ion and electron temperatures at the start of the compression are $T_i = 600 \text{ eV}$ (from neutron data, see section 4.6) and $T_e = 200 \text{ eV}$ (from AXUV diagnostic, see section 4.4). That $T_i \approx 3 T_e$ is due to a combination of CHI formation dynamics, a thermal confinement difference $\tau_{Ei} > \tau_{Ee}$, and the compression beginning before electrons can equilibrate with ions. Because $T_i > T_e$ equilibration provides a significant ion cooling term that nearly balances compressional heating of ions. Ion–electron thermalization physics and implications are discussed in appendix F. Note that the ion Doppler data

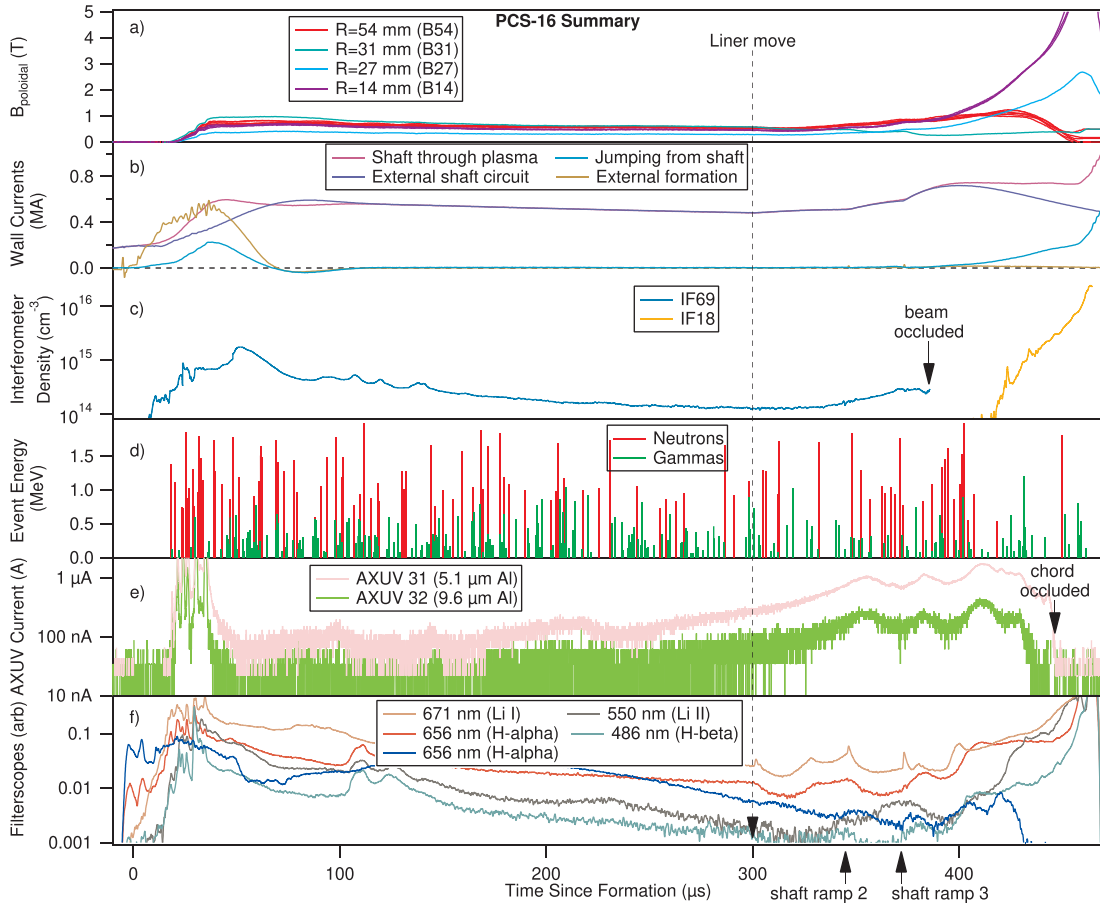


Figure 7. Summary of key measurements vs. time during PCS-16 shot. From top to bottom these are (a) Mirnov probes signals of poloidal magnetic field B_{poloidal} , (b) wall currents, (c) line averaged density from two interferometer chords, (d) neutron and gamma detection events, (e) Al-filtered AXUV current, and (f) filteroscope measurements. Arrow markers indicate the time at which the liner begins to move, at which the first shaft current ramp pulse is fired, then the times of triggering the second and third shaft ramp pulses, as well as the times at which the interferometer beam and AXUV line of sight become occluded by the liner passing across the chord.

shown in section 4.5 does not provide a good indication of the core ion temperature due to the carbon impurity likely being fully ionized there, and the measured C V charge state is likely to only exist further out closer to the wall where it is colder.

- The AXUV x-ray photodiode signals show a smooth rise in x-ray emission for the first $55 \mu\text{s}$ of compression, and then transition into a sequence of peaks corresponding to a phase of increased MHD mode activity as seen in the Mirnov probes. See figure 7 as well as a complete description in section 4.7.

We will discuss the details of these observations in the following subsections.

4.1. Density rise during compression and implied profile

At first sight, the two interferometric chords (denoted IF18 and IF69 figure 1) seem like a small number of measurements compared to other fusion experiments. However, during compression, the moving central region of the plasma is swept across the measurement chord before the beam is occluded by the liner. The IF18 chord initially measures the vacuum

on open field lines until late in compression when the edge of the plasma enters the beam and samples the core of the plasma when it is extremely compressed. Based on this information, it is possible to provide strong constraints on the density profile and total electron inventory.

In the general case, forward modeling of the interferometric signal is required to attempt to deconvolve the effect of possible density profile evolution with simultaneous changes in the electron inventory. However, the PCS-16 raw data (figure 9) is particularly well fit by a simple model in which the total electron inventory is constant in time and the density profile has a broad flat region over most of its volume and falls to $n_e \approx 0$ at the wall. The well-behaved quality of the density signal can rule out the possibility that a large amount of high Z material entered the plasma at some point, as well as ruling out a poor particle confinement time. The plasma density profile is a key input to neutron-implied temperature calculations in section 4.6, and we find that the observations are well described by a model profile with a central plateau with a Gaussian edge of the form:

$$n_e(\bar{\psi}, t) = n_e(0, t) \left[1 - e^{-(1-\bar{\psi})^2/0.005} \right]. \quad (10)$$

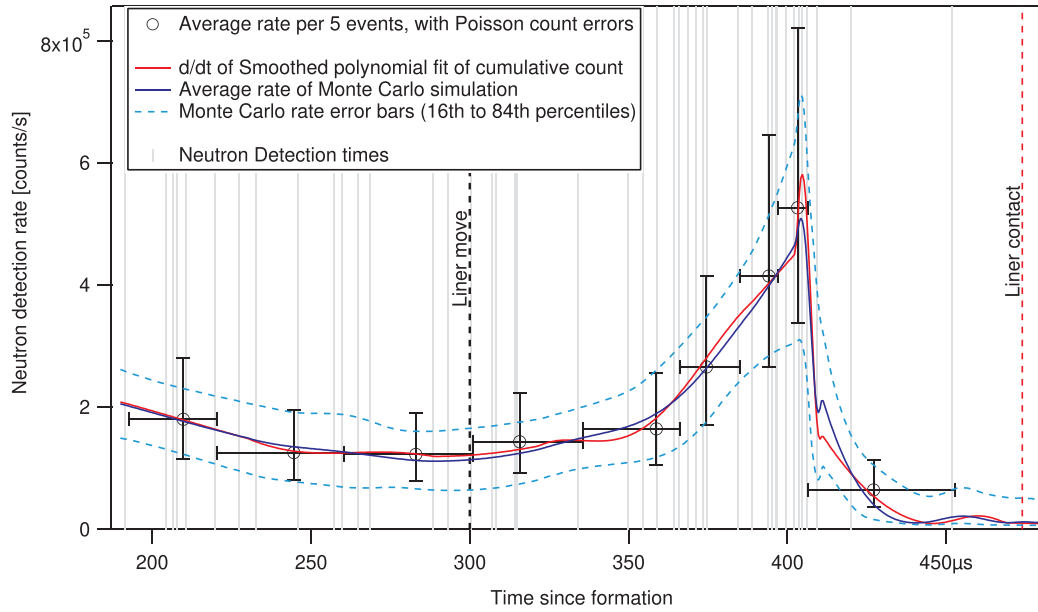


Figure 8. Neutron detection rate quantified by several methods. Vertical light grey lines show the sequence of detection times. Black markers (\circ) show average rate per 5 detections, with vertical bars showing Poisson uncertainty in a true rate, and horizontal bars showing the duration of each time-bin. The red curve is time derivative of the smoothing polynomial fit of the cumulative neutron count $\rho_n(t) = dP_S(t)/dt$, while the upper and lower bounds determined from the standard deviation of slope values of a set of random instances of cumulative counts generated in a Monte Carlo Poisson simulation of the detection process. See section 4.6 for a complete description of the analysis.

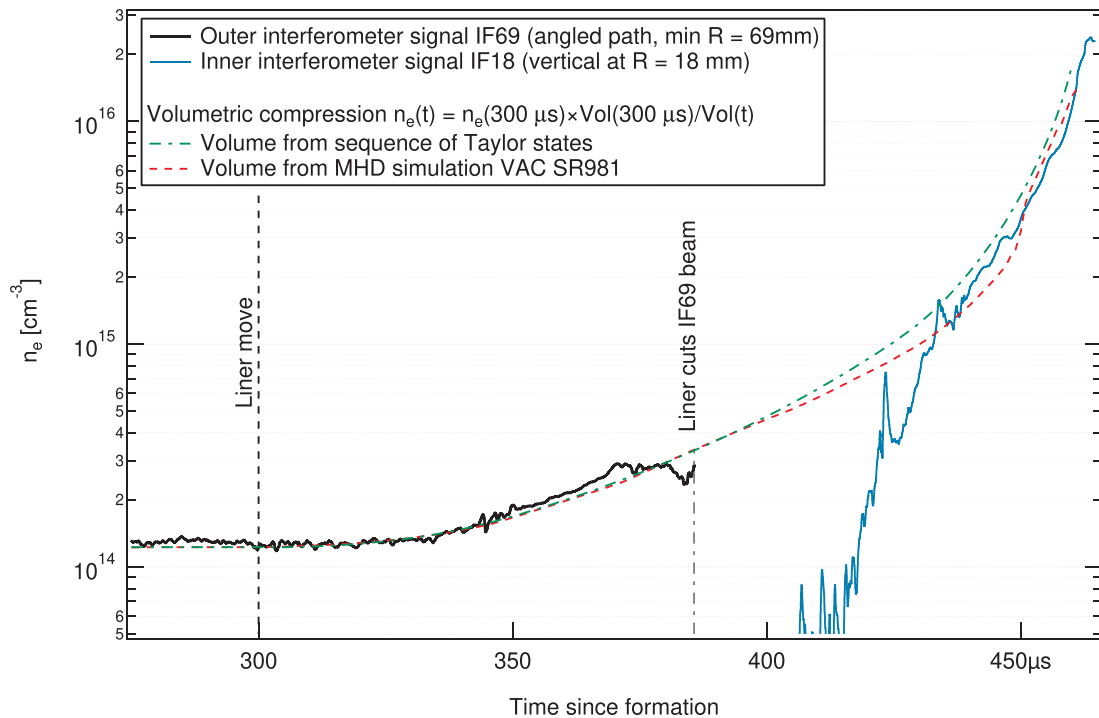


Figure 9. Measured line-averaged density on outer chord IF69 (minimum $R = 69$ mm, black curve), which initially measures the outer half of the plasma volume before compression begins then is swept across the moving core of the plasma until the beam is fully cut off by the liner motion at $t = 385 \mu\text{s}$, and inner chord IF18 ($R = 18$ mm, blue curve), which is near the shaft and only measures significant density once the core of the plasma begins to push into the pocket region of the shaft at late time $t > 410 \mu\text{s}$. Measured signals are compared to two versions of volumetric compression estimates, using volume versus time from a sequence of Taylor state solutions $\psi(R, Z)$ (green dashed curve) and volume inside the $\psi = 95\%$ surface of an MHD simulation (red dashed curve), VAC run SR981, which has transport fine-tuned to match PCS-16 magnetic decay and probe ratios (see section 5.2).

Here the core density is particle-conserving while the rapid compression is:

$$n_e(0, t) = C_V(t) n_e(0, t_0) \quad (11)$$

with the volumetric compression ratio of $C_V(t) = V(t_0)/V(t)$, where V is the volume of the plasma and $t_0 = 300 \mu\text{s}$ is the time of liner move.

From this analysis we estimate the volume of the plasma as a function of time in several ways. We have an accurately determined geometry of the space between the inner electrode and the collapsing liner as a function of time, established from PDV [53] measurements and contact pin timing from a sequence of previous test implosions with no plasma. The exact shape of the liner was determined from a solid-mechanics deformation simulation (using Ansys LS-DYNA) which had material models adjusted until a best-match to the empirical measurements of wall position was found. For the PCS-16 shot itself we obtain the time of occlusion for each of the optical diagnostics, as well as the time of the metal-metal liner contact from the Mirnov probes, which all confirm that the actual wall motion matches the preestablished model to within $1 \mu\text{s}$ accuracy. The plasma will nearly fill the radial extent of the metal cavity. However, due to the field line tension of the poloidal magnetic field the plasma will be constrained in the axial direction rather than filling the full volume of the open vessel. To determine how the magnetized plasma is constrained by the concave geometry of the outer wall, the simplest method is to calculate a Taylor state eigenvalue solution [54] that is uniquely determined by the boundary geometry. The Taylor state calculation gives the poloidal flux function $\psi(R, Z)$, and we find the volume inside the outer flux surface such as $\bar{\psi} = 90\%$ to calculate the expected density rise for constant electron inventory due to volumetric compression as shown in the green dashed curve in figure 9. The Taylor state is useful in its simplicity, however it only works as a rough approximation to magnetic geometry. Improvements can be made by matching an MHD simulation to the experimental signals (section 5.2), which can self-consistently predict changes to volume due to flows not considered in the simpler equilibrium models. The results using the volumes from the MHD simulations are shown in the red dashed curve in figure 9. Despite the distinct properties of these different approaches, they both converge closely to the trend observed with the interferometer signals as measured.

Once the compression begins at $t = 300 \mu\text{s}$ and the plasma is moving across the interferometer beam, we are able to constrain the density profile from this extra information, however before compression begins the profile in the early phase just after formation is less well determined. Studies on a nearly identical lab-only SPECTOR-1 device with an array of four horizontal midplane interferometric chords showed that the early density profile was hollow with a large off-axis maximum in density that relaxed into a flat profile. We also see evidence that a crowbar current near the mouth of the Marshall gun can cause an extra density signal on the IF69 chord that is not observed in the midplane horizontal chords. This leads us to the interpretation that the high spike in density seen on IF69

just after formation in the PCS-16 campaign is due to a combination of these effects directly observed in SPECTOR-1. As such, it is reasonable to interpret the value of IF69 reading as being higher than the core density until the crowbar current dies, and the profile can relax into a more flat profile by 200–300 μs , typical of the observed behavior on SPECTOR-1 and consistent with the density profile observed by beam-sweeping during compression for $t \geq 300 \mu\text{s}$ on PCS-16.

As a general point of analysis there is motivation to characterize the early phase of the plasma discharge of the PCS-16 shot before compression begins and correlate this to other similar shots to establish an approximate counterfactual baseline of behavior that the PCS-16 shot would have continued on if it had not been compressed. An important metric of behavior can be found in the density signal, which can be very reproducible shot-to-shot, yet with a semi-random bimodal behavior that can be roughly categorized into ‘low-density’ shots and ‘high-density’ shots, which begin to be distinct in average density value after $t > 250 \mu\text{s}$. All the shots in both categories used the same operating settings and the difference in behavior is due to small random variation in gas input and wall effects. The two categories of shots have the IF69 signal at $t = 300 \mu\text{s}$ in the range of $(8.7 \pm 2.7) \times 10^{13} \text{cm}^{-3}$ for the low-density shots and in the range of $(9.8 \pm 1.9) \times 10^{13} \text{cm}^{-3}$ for the high-density shots. These categories of shots become even more distinct in density values by $t = 500 \mu\text{s}$, having completely disjoint error bands for the middle phase of the discharge. At $t = 750 \mu\text{s}$ the low-density category ranges over $(3.6 \pm 0.9) \times 10^{13} \text{cm}^{-3}$ while the high-density category spans $(7.7 \pm 1.7) \times 10^{13} \text{cm}^{-3}$. The PCS-16 shot before the liner move was at the upper end of the high-density range at $n_e(300 \mu\text{s}) = 1.25 \times 10^{14} \text{cm}^{-3}$. The equatorial to polar Mirnov probe ratio (B54/B31, see figures 1 and 7(a)) was a secondary classifier of the categories in the case of similar density values midway between the two average values, with a higher ratio corresponding to the high-density category. Overall, there were 66 shots that fit into the high-density category, and 58 shots that fit into the low-density category. The low-density group has a noticeably higher neutron count rate than the high-density group (see section 4.6), and the low-density shots also show higher electron temperature AXUV signals (section 4.4). The PCS-16 shot has a precompression density evolution that lies at the high end of the high-density category and has a similar probe ratio that places it in that category. However, its neutron emission and AXUV electron temperature are in the middle territory between the two categories.

4.2. Peak magnetic compression ratio

As a way to quantify poloidal flux conservation during compression, we can begin by defining the ratio of peak $B_{\text{pol}}(t_{\text{max}})$ when compressed to the initial value of $B_{\text{pol}}(t_0)$ at that Mirnov probe when the liner starts to move as:

$$C_B = \frac{B_{\text{pol}}(t_{\text{max}})}{B_{\text{pol}}(t_0)}. \quad (12)$$

Table 1. Summary of results for peak compression of poloidal magnetic field for PCS-16.

Label	Mirnov position	N_{probes}	t_{max}	$C_R(t_{\text{max}})$	$C_B(t_{\text{max}})$	$\max(C_B)$ ideal
B54	$R = 54$ mm	6	$418.6 \pm 7.1 \mu\text{s}$	1.91	2.1 ± 0.12	2.7
B27	$R = 27$ mm	1	$457.7 \mu\text{s}$	6.76	9.1	No limit
B14	$R = 14$ mm	3	$461.2 \pm 1 \mu\text{s}$	8.65	13.74 ± 1.52	No limit

During the PCS-16 compression, we saw a significant magnetic compression ratio at the $R = 27$ mm (B27) Mirnov probe with $C_B = 9.1$ at $t_{\text{max}} = 457.7 \mu\text{s}$, while the three probes at $R = 14$ mm (B14) reached a mean value $C_B = 13.74 \pm 1.52$ at $t_{\text{max}} = 461.2 \pm 1 \mu\text{s}$. The plasma has reached a radial compression ratio of $C_R = \{6.76, 8.65\}$ at the peak times $t_{\text{max}} = \{457.7 \mu\text{s}, 461.2 \mu\text{s}\}$ respectively. After these times of peak magnetic field, the signal at these probes decreases rapidly due to resistive flux loss in the final stages of compression. Results are summarized in table 1.

In addition to flux compression, liner motion also results in a radial shift in the magnetic axis, and so probes at larger radius will have a maximum possible C_B value even if the flux is perfectly conserved. Compression past that point reduces the field measured at that probe because the radius of the magnetic axis is less than the radial position of the probe, and the probe is beginning to sample toward a low-field corner of the plasma. See the flux surfaces of the compressed state illustrated in figure 1 for an illustration of this effect. For the six $R = 54$ mm probes (B54) on PCS-16 we observe a peak magnetic compression of $C_B = 2.1 \pm 0.12$ at $t_{\text{max}} = 418.6 \pm 7.1 \mu\text{s}$, corresponding to a compression ratio of $C_R = 1.91$. The ideal limit assuming self-similarity through (9) is $C_B = 1.91^2 = 3.65$. Thus, the simplest estimate of flux conservation is $\psi(418 \mu\text{s})/\psi_0 = 2.1/3.65 = 0.57$. Using the MHD simulation results described in section 5.2 to more accurately describe the non-self-similar geometry changes, we find that with perfect flux conservation the magnetic field at the $R = 54$ mm (B54) position would only increase by a factor of $C_B = 2.7$ before decreasing due to the magnetic axis passing through the probe. With this as the ideal case, an estimate of flux conservation up to the observed peak at $R = 54$ mm would be $\psi(418 \mu\text{s})/\psi_0 = 0.77$.

We next see in section 4.3 that these analytic estimates of poloidal flux conservation during compression have reasonable accuracy compared to several alternative analysis methods.

4.3. Poloidal flux conservation during compression

The closed poloidal flux in the plasma and how it evolves is important because it is the primary contributor to magnetic confinement. In this section we compare three different methods of estimating the poloidal flux as a function of time (shown in figure 10), all working from the Mirnov probe magnetic signals as input data. These constitute an extension of the simple analytic estimates presented in section 4.2 which compare the observed magnetic compression ratios C_B at different probe positions to what they would have been in an idealized flux conserving compression.

The most direct method to estimate the poloidal flux as a function of time uses a magnetic equilibrium reconstruction based on the surface poloidal field values at the Mirnov probe locations [55]. We use a Bayesian fitting method that is briefly described in appendix C. The reconstructed poloidal flux is nearly constant at 15.5 ± 1.5 mWb for the $100 \mu\text{s}$ before compression. During the first $25 \mu\text{s}$ of compression the estimated flux at the magnetic axis decays with a loop voltage of 45 V. This coincides with the early phase of slowly accelerating compression before the liner trajectory begins to follow the power-law heating trajectory (25). Then, after $t = 345 \mu\text{s}$, the reconstruction indicates a rise in poloidal flux, which could be due to a dynamo process involving the $n = 1$ mode that is observed to be slowly grown at that point (see section 4.7). The Bayesian reconstructed model fits the PCS-16 surface magnetic measurements quite accurately with a relative error of only 5%–7%, however there is no guarantee that this reconstruction is unique. The a-posteriori error estimates for reconstructed output values such as poloidal flux depend on the assumption that the physical truth is contained within the model equilibria of the Grad–Shafranov solution lookup table; if the truth is outside of what can be represented by the assumed profiles that generate the table, then the estimated flux can differ from the physical truth by more than the Bayesian error estimated in figure 10. The reconstruction method was also limited to only being able to provide flux estimates up to $t = 405 \mu\text{s}$, after which the Grad–Shafranov solver had a high rate of failing to converge on equilibrium solutions for these highly compressed geometries, resulting in incomplete lookup tables.

An independent method for estimating the poloidal flux vs. time, which has some advantages, is to fine-tune the initial conditions and transport coefficients of an MHD simulation to match the values and rates of change of the Mirnov probe signals from PCS-16. The resulting poloidal flux (blue curve in figure 10) from this MHD simulation (VAC run SR981) is within the error bars of the Bayesian reconstructed values at the time of the liner move. A detailed discussion of this simulation is given in section 5.2. The advantages of this method are that it provides an evolution that is physically consistent with resistive MHD during compression without assumptions of an analytic functional form for pressure or current profiles, and it provides a comprehensive physics model nearly continuously in time all the way through full compression. The drawback of this MHD simulation model is that it tends to underestimate how thermal losses evolve within the compression and at late times over-estimate the poloidal flux conservation. It also may not properly capture the possibility of dynamo processes and the corresponding flux amplification, despite having some capability for simulating nonaxisymmetric three-dimensional

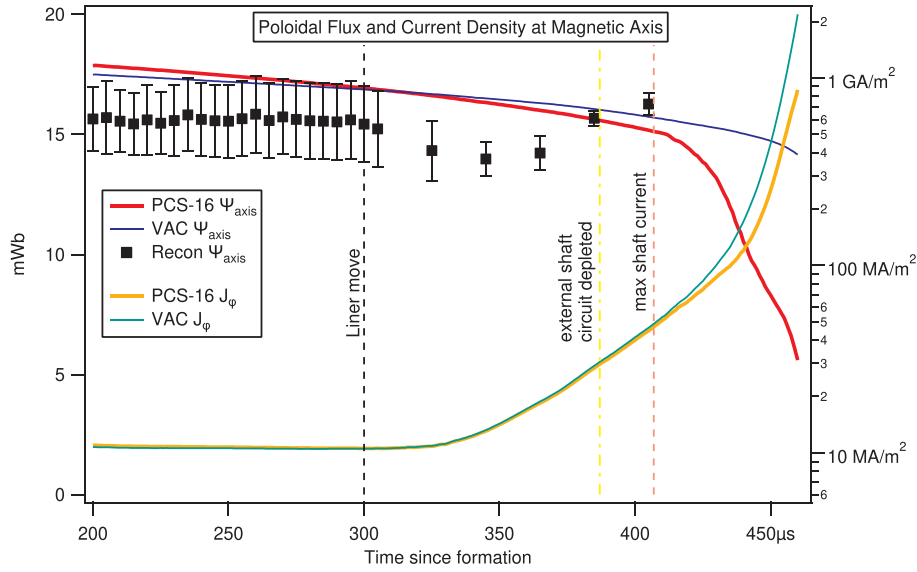


Figure 10. Estimated experimental poloidal flux at the magnetic axis (ψ_{axis}) by three methods are compared to each other, as well as toroidal current density (J_{ϕ}) at the magnetic axis via two methods. Black markers show the poloidal flux and one-sigma error bars determined from a Bayesian Grad–Shafranov equilibrium reconstruction [55], which finds a best fit to the experimental magnetic data. The blue trace shows the poloidal flux vs. time for the three-dimensional MHD simulation (VAC) for which the initial conditions and thermal transport model were fine-tuned to best match the evolution of magnetic signals from the PCS-16 shot before compression. The red trace shows an estimate of poloidal flux that is an improvement on the simulation-derived estimate by taking the ratio of the experimental magnetic signals divided by the simulated synthetic magnetic signals and multiplying by the simulated poloidal flux. Current density at the magnetic axis (orange trace) can be rescaled from the simulation (green trace) by the magnetic probe ratio as an intermediate step in calculating the resistivity.

dynamics. A final limitation is that only a certain amount of fine-tuning is practical to do via a sequence of MHD simulations, and while the final agreement with PCS-16 initial magnetic geometry was good (10% average error of probe ratios), it is not quite as good as the Bayesian fit (5% average error of probe ratios).

This final method of poloidal flux estimation makes use of the VAC SR981 simulation as a simple and quantitatively well-understood example model with known flux, known magnetic field values at the Mirnov locations, and having a physically realistic plasma geometry. Then, we apply a rescaling correction to the poloidal flux based on the ratio of actual magnetic field values divided by those in the VAC model as:

$$\psi_{\text{exp}}(t) = \psi_{\text{VAC}}(t) \left\langle \frac{B_{\text{exp}}(t)}{B_{\text{VAC}}(t)} \right\rangle. \quad (13)$$

This correction term is an average (experiment/VAC) magnetic ratio for the $R = 27\text{mm}$ (B27) and $R = 14\text{mm}$ (B14) Mirnov probes, with smoothing applied to the raw experimental signals for $t < 405\ \mu\text{s}$. The same correction factor can rescale the VAC toroidal current density J_{ϕ} to give an estimate for its value in the experiment. These results are shown in figure 10. The primary observation of this result is that the plasma appears to only slowly decay in poloidal flux until 405–410 μs when something happens that causes it to begin to rapidly lose flux compared to the VAC model.

The estimate (13) of $\psi_{\text{exp}}(t)$ for PCS-16 is a conservative lower bound on poloidal flux because resistive decay of edge currents or plasma reorganization via dynamo processes can cause the profile to become increasingly peaked with time,

which would result in lower magnetic signals at the wall even if poloidal flux is perfectly conserved in the core. Therefore, this will be a lower bound on $\psi(t)$, which pessimistically assumes that the apparent reduction of the relative magnetic signal at the wall is due entirely to resistive flux loss at the core without a change in the shape of the current profile.

With an estimate of the value of Z_{eff} , the rate of change of $\psi(t)$ can be used to infer a lower bound on the electron temperature, which is discussed in appendix D. The general conclusion from this analysis is that there was an event around 410 μs that led to rapid cooling and was responsible for the increased rate of resistive flux decay during the final stage of plasma compression.

4.4. Electron temperature from filtered AXUV soft x-ray ratio

Pairs of AXUV photodiodes with flat responsivity (A W^{-1}) in the XUV to soft x-ray region ($\lambda < 70\text{nm}$) collect light from the plasma through apertures along approximately overlapping lines of sight. Each diode has a different thin metallic filter that passes photons with energy greater than a threshold, typically $E_{\gamma} > 1500\text{eV}$, but with an exact filter function that depends on foil thickness and material. The filters used on PCS-16 included $5.1\ \mu\text{m}$ and $9.6\ \mu\text{m}$ thick aluminum. Using the spectral transmissions of each filter and simulations of the plasma emissivity spectrum using the FLYCHK [56] code, we construct a lookup table of forward-modeled diode signals for various temperatures and a range of possible models for the plasma impurity content. The ratio of calibrated diode currents, shown in figure 7, can then be used to infer the temperature of the plasma [40].

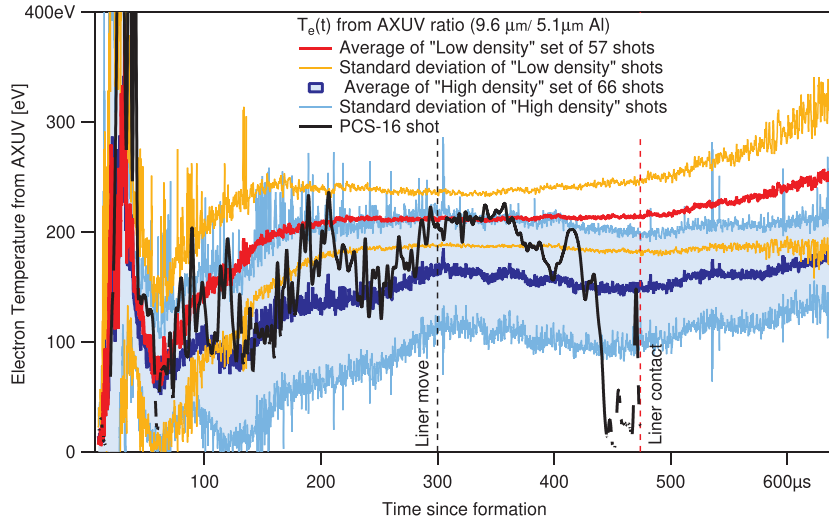


Figure 11. Electron temperature measured by ratio of filtered AXUV signals. This graph shows how $T_e(t)$ varies between the two categories of field configuration shots ‘low-density’ (red with orange error bands, one shot is omitted from the average due to electrical noise problems on the signal) and ‘high-density’ (dark blue with light blue error bands) and the PCS-16 compression shot (black). The low-density group has less deviation within the set and has a mean value roughly one sigma above the mean of the high-density group. There are some properties of the PCS-16 shot that would imply it should be categorized as a member of the high-density group, although it is on the high end the spread for $T_e(300\mu\text{s})$, which coincides with mean of the low-density group. On the basis of AXUV signals, it would appear that the PCS-16 shot is somewhere in between the two groups.

As shown in figure 11, the AXUV measurement of T_e at time of liner move for the PCS-16 compression shot is $T_e(300\mu\text{s}) = 207 \pm 10\text{eV}$, similar in value to the range of measurements for the low-density shots which had $T_e(300\mu\text{s}) = 211 \pm 24\text{eV}$, while the high-density shots were colder with a wider range of values: $T_e(300\mu\text{s}) = 164 \pm 50\text{eV}$.

The primary observation from this diagnostic indicates that T_e was essentially constant during the first $60\mu\text{s}$ of compression, then began a linear decline until $t = 400\mu\text{s}$, then experienced an upturn for the next $15\mu\text{s}$ before a final rapid cooling event that coincided with loss of signal in the AXUV due to occlusion by the liner at $t = 445\mu\text{s}$ (see also figure 20).

In chord-averaged temperature measurements, this measurement is likely to have some sensitivity to spatial inhomogeneities in the plasma temperature, resulting in the high frequency fluctuations seen in the signal. We also believe it is likely that the transient upturn in T_e after $400\mu\text{s}$ is due to a relatively hotter region passing directly into view, rather than indicating overall heating of the whole plasma.

To provide context for this result it is informative to examine the energy balance for the electron population during compression, taking $t = 360\mu\text{s}$ as a representative example when compression is underway in a smooth fashion. The dominant heating term is the Ohmic heating power $P_\Omega(360\mu\text{s}) = 1.03\text{MW}$ determined through (7) with an initial flux decay time of $\tau_{\psi_0} = 266\mu\text{s}$, while the electron compressional heating power via (8) is $P_{\text{comp}, e}(360\mu\text{s}) = 447\text{kW}$. For the collisional heating power applied to electrons from the hotter ions, we can multiply the first term of (41) by $(3/2)n_i V_0$ and taking $\tau_{\text{eq}} = 693\mu\text{s}$, gives a value $P_{i,e} = 498\text{kW}$.

With this accounting for the energy balance we can estimate the thermal confinement time for electrons. For the isothermal

case we have a thermal confinement time of:

$$\tau_{\text{Ee}} = \frac{E_{\text{th}, e}}{P_\Omega + P_{\text{comp}, e} + P_{i,e}}. \quad (14)$$

This gives $\tau_{\text{Ee}} = 52\mu\text{s}$ using the electron thermal energy $E_{\text{th}, e}(360\mu\text{s}) = 102.3\text{J}$. This is of a similar magnitude to the overall thermal confinement time of $\tau_E \approx 84\mu\text{s}$ that was indicated by the MHD simulations that matched the experimental magnetic decay (see section 5.2). With an electron thermal confinement time on the order of $\tau_{\text{Ee}} \approx 50\mu\text{s}$ it is expected that electrons would act as a net cooling influence given the significantly longer compression time of PCS-16 ($\tau_C \approx 139\mu\text{s}$). The scaling of electron thermal confinement time with device size in STs in line with $\tau_{\text{Ee}} \sim R^2$, provides a route for expected improvement of this result. It is likely that a reactor-scale compression device would have a significantly longer energy confinement time than this subscale experiment.

4.5. Ion temperature from IDS

The IDS diagnostic uses two high-resolution 0.55m focal-length Czerny–Turner spectrometers (Horiba iHR550), with 16-channel linear photomultiplier tube (PMT) arrays as detectors. One spectrometer collects light from the $R = 88\text{mm}$ vertical chord (IDS G), which passes through the central region of the plasma, while a second identical spectrometer (IDS H) observes light at the $R = 35\text{mm}$ vertical chord, which is close to the edge of the plasma until deep into compression (see figure 1). For PCS-16 we had both spectrometers measuring the C V 227.089 nm line, however because of its location close to the plasma edge, the IDS H chord at $R = 35\text{mm}$ did not produce a consistent enough signal on in-field aggregates shots to allow being included in this analysis. Instead, we focus on the

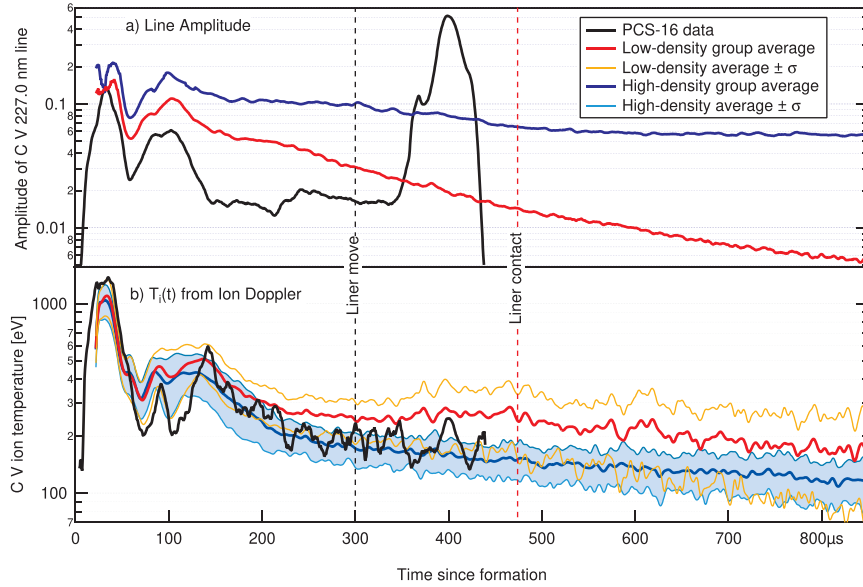


Figure 12. Data from IDS chord G ($R = 88$ mm) from PCS-16 and in-field aggregate shots. In (a) we show the measurement amplitude of the C V 227 nm line (volts) for the compression shot (black), the low-density aggregate average (40 shots, red) and the high-density aggregate average (45 shots, blue). Ion temperature shown in (b) with error bands equal to the standard deviation the aggregates.

IDS G data, which better measures near the core of the plasma during the early phase of compression, as well as providing a baseline for behavior from noncompressed aggregate data.

In our implementation of the IDS system, PMT outputs are digitized at 10 MHz sample frequency and then are time-integrated numerically in post-processing to form spectra vs. calibrated wavelengths for time-bins that typically need to be a few microseconds in duration to achieve good signal-to-noise ratio. The observed spectrum is fit to a Gaussian line shape to obtain the spectral width, Doppler shift and line brightness as a function of time. Instrumental broadening is then subtracted from the line width in quadrature to obtain the ion temperature of the carbon impurity. This is an emissivity-weighted average temperature along the observation chord. The estimated relative error on T_i due to the quality of the Gaussian fit can be in the range of 7%–20%, however due to nonuniformity of plasma properties and carbon abundance the measured value $T_i(t)$ can fluctuate in time by 30% on a timescale of $\sim 10 \mu\text{s}$. Because of this, taking averages over an aggregate of many similar shots can show a clearer trend in the evolution of ion temperature vs. time. Data is shown in figure 12.

From the comparison of the PCS-16 shot and lead-up shots we see that there is a consistent trend for the low-density shots (40 shots with the same IDS settings) to have a relatively dim carbon line and hotter T_i measurements than the high-density shots (45 shots with the same IDS settings), see figure 12. The PCS-16 shot had an average $T_i(t)$ evolution that was very close to the high-density average, however it had a significantly lower C V line amplitude than either aggregate group. This, combined with the fact that PCS-16 has higher density than average, may suggest that the impurity concentration is particularly low for PCS-16 which may have contributed to its successful performance. At the time of wall-move for the PCS-16 shot we measure a fluctuation cycle-average

of $T_i(300 \mu\text{s}) = 201 \pm 32$ eV, while the high-density aggregate had $T_i(300 \mu\text{s}) = 172 \pm 35$ eV. Line brightness for the PCS-16 shot is maximum at $t = 400 \mu\text{s}$ which corresponds to the moment just before the transition to rapid cooling as seen by the AXUV and neutron yield measurements.

It is also worth noting that the IDS temperature measurement constitutes a lower bound for T_i , due to it being an emissivity-weighted chord-average of the impurity ion temperature and for the observed values of n_e and T_e the charge state being observed only exists in coronal equilibrium at a position midway between the core and the edge, so it is likely that we are not measuring the core value of T_i . In figure 13) we show a coronal equilibrium calculation of the distribution of C V charge states within the plasma volume, using a parabolic $T_e(\psi)$ profile with a core value of $\max(T_e) = 200$ eV. The fact that neutron yield measurements (section 4.6) consistently show higher core ion temperatures than IDS measurements is supportive of a parabolic-like profile where the core is hotter than the mid-region where C V can exist in equilibrium.

Finally, by inspecting the raw spectral data shown in figure 14, it is clear that we are observing a single isolated line with a single Gaussian shape. We also see that for the early phase during formation the carbon line is distinctly blue-shifted due to being ejected from the Marshall gun toward the collection optics at substantial vertical velocities (10^5 ms^{-1}). However, for the remainder of the plasma evolution, including the compression phase, there is no significant Doppler velocity shift in the C V line. The high axial velocity during fast-CHI formation is the primary reason why the ion temperature begins at such a high value, which is due to the net kinetic energy of the ions being converted into thermal energy as the particle motion is randomized during the stagnation of this fast flow.

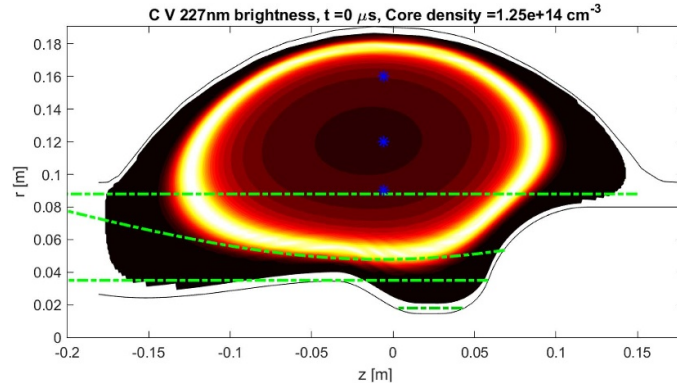


Figure 13. The coronal equilibrium C V charge state distribution in space for a parabolic $T_i(\bar{\psi})$ profile and the corresponding locations of the PCS-16 diagnostic chords (green dashed) with IDS, AXUV both at $R = 88$ mm, the IF69 chord being angled out of plane and so projects to a hyperbola in the (R, Z) plane, while the IDS $R = 35$ mm and the innermost IF18 ($R = 18$ mm) measure only in the pocket region for observing deep compression. Corresponding locations for midplane interferometry chords for SPECTOR-1 are shown as blue markers.

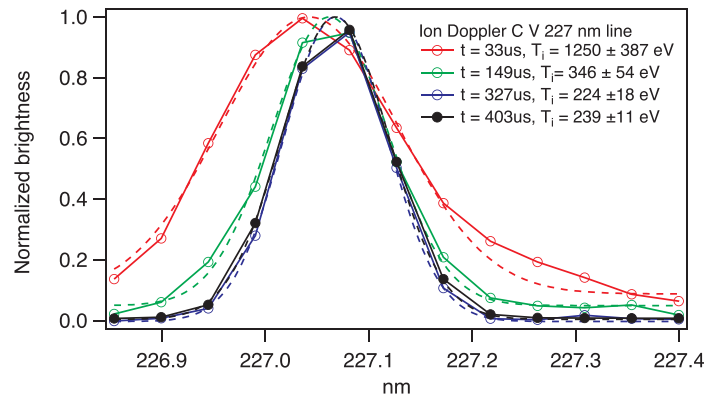


Figure 14. Data from IDS chord G ($R = 88$ mm) from the PCS-16 compression shot, showing the raw spectra at four points in time and the resulting Gaussian fit from which T_i is determined.

4.6. Ion temperature from neutron analysis

We monitor the high energy (100 keV–30 MeV) particle emission during the plasma shot with eight liquid scintillators manufactured by Scionix that use EJ301 fluid (five detectors) or EJ309 fluid (three detectors) with PMTs from ET Enterprises Ltd 9390B series (large) and 9821B series (small). The scintillator fluid is contained in an aluminum cube, the two smaller detectors have a volume of $10 \times 10 \times 10 \text{ cm}^3$, while the six larger detectors have a volume of $15 \times 15 \times 15 \text{ cm}^3$. On PCS-16, some were mounted quite close to the compression chamber, inside armored steel cases, and all but one were shielded with 25.4 mm thick lead [41]. See figure 15 for details of the physical placement.

Signals are digitized at 2 GHz during the shot, so that offline digital pulse shape discrimination (PSD, [57]) can be used to distinguish between incident neutrons and gammas, as well as measure their energy, with $\{n, \gamma\}$ discriminated pulses shown in figure 7 panel (d). Our detectors have been absolutely calibrated for detection efficiency at the TRIUMF nuclear physics lab with an Am-Be source producing both gammas and neutrons. The detectors were further calibrated with a deuterium-tritium neutron generator at

Simon Fraser University. The PSD threshold curve has been calibrated to reject gammas emitted from a Co-60 source. The calibration of the overall sensitivity of the scintillator array to infer the neutron yield from the plasma source is determined through MCNP simulations [58] as described in appendix B. We find from the analysis of the MCNP simulation that any PSD-identified neutron detection event of $E > 0.5 \text{ MeV}$ (proton-scaled energy) can only occur from prompt neutrons (2.45 MeV) that have been generated by D-D fusion in the plasma within the previous $1.2 \mu\text{s}$, having a minimal amount of scattering off the structure before being detected. Secondary gamma emission from neutron-induced reactions in the structural material was also included in the MCNP simulation outputs and was studied for the expected energy spectrum and total count rates in the scintillator. Gamma events can be detected with significant delay due to nuclear reactions involving highly downscattered thermal neutrons.

Analysis of the scintillator data for 124 shots taken while the mobile experiment was situated in the field can serve as a baseline for performance with which to compare the change in neutron output during the PCS-16 compression shot. The in-field shots can be divided up in to two main categories of plasma discharges, high-density and low-density, as described

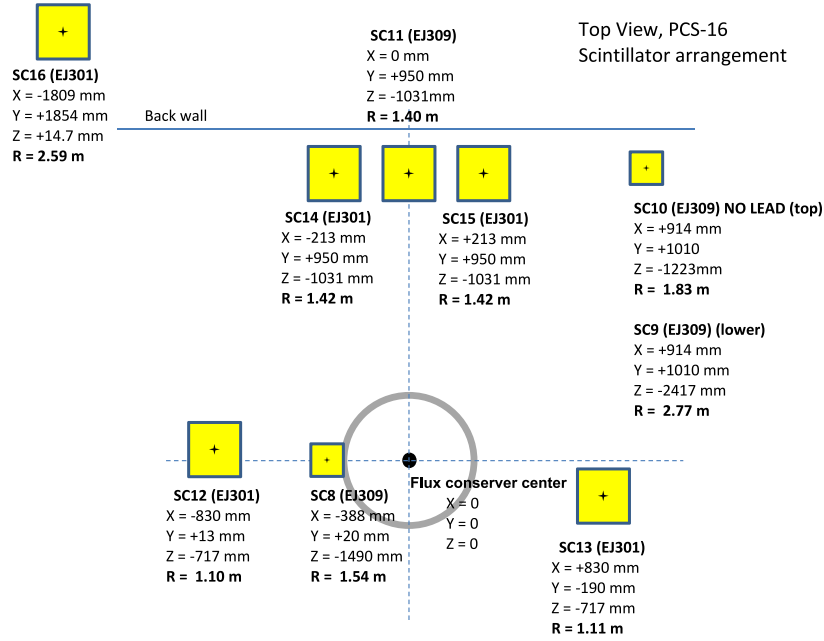


Figure 15. Arrangement of neutron scintillators relative to the plasma vessel. Scintillators are shielded by 25.4 mm of lead to reduce gamma flux except for SC10 which is used to validate n/γ PSD ratio by directly measuring both. Liquid hydrocarbon scintillating fluids EJ301 and EJ309 are used. SC8 collected data for lab shots but was not collecting data for the field shots.

in section 4.1. The combined dataset for each of these categories can be aggregated together to give an average rate of neutron emission that has substantially smaller statistical uncertainty than for a single shot.

The PCS-16 shot can be considered to be a member of the high-density category, both in terms of initial density and probe ratio, however its precompression neutron output was more similar to the low-density shots, which typically had hotter electron and ion temperatures in addition to lower density. Taking all evidence into account, it is reasonable to conclude that the pre-compression phase of the PCS-16 shot had elevated neutron output due to having higher than average density while having a similar ion temperature to the average of the high-density aggregate shots.

The neutron rate measured during compression in PCS-16 is significantly higher than what would be expected in any of the uncompressed shots during the same time window, as shown in figures 8 and 17. This increase in the neutron rate is most consistent with the interpretation of being caused by an increase in density during compression, while the ion temperature is nearly constant.

The determination of the Maxwellian ion temperature from the neutron count rate is completed according to the following method. First, the PSD identified neutron count rate and uncertainty as a function of time was tabulated via two complementary approaches:

1. Sequentially we find the time interval Δt_i in which the i th (nonoverlapping) set of five counts occurs, and the average rate within this time-bin is $\rho_n(t_i) = 5/\Delta t_i$. The one-sigma uncertainty of the true value of the dimensionless Poisson rate parameter λ , given that five counts were observed, is

determined by the equation $\lambda \pm \sqrt{\lambda} = 5$, which has solutions of $\lambda = \{3.21, 7.79\}$ and the bounds on the physically true rate during that time bin would be $3.21/\Delta t_i < \rho_n(t_i) < 7.79/\Delta t_i$. This approach will average across rapid changes in the actual neutron rate that may happen in a longer-duration bin, resulting in apparent average rates that are due to past or future neutron counts that are close to the edge of the bin, and losing some information in the process. Fewer counts per bin will have a better ability to track rapid changes but will have correspondingly higher uncertainties for local rates, and will not convey the correct trend of how the rate changes as the plasma evolves due to exaggerated rates when a few detection events coincidentally occur close together. A choice of more counts per bin will result in larger bins that have lower intrinsic error bars and better show the general trend of how the rate changes with time but does a worse job at showing a rapid decrease in count rate. Overall $N = 5$ counts per bin were close to an optimal compromise for this method.

2. Tabulating the cumulative neutron count as a function of time $c_n(t) = \sum_i H(t - t_i)$, where $H(x)$ is the Heaviside step function, we then fit a locally low-order piecewise smoothing polynomial $P_S(t)$ to the cumulative data which is continuous and has continuous 1st derivatives everywhere [59]. Then, the instantaneous detection rate is calculated as $\rho_n(t) = dP_S(t)/dt$. This will give a continuous rate that is within the error bars of the average rate determined by approach 1) but has better ability to localize inflection points in the full set of data encoded in $c_n(t)$. Error analysis can be conducted via Monte Carlo simulations of time-dependent Poisson processes (via thinning algorithms, e.g. [60]) with trial functions $\lambda(t)$ that specify the expected

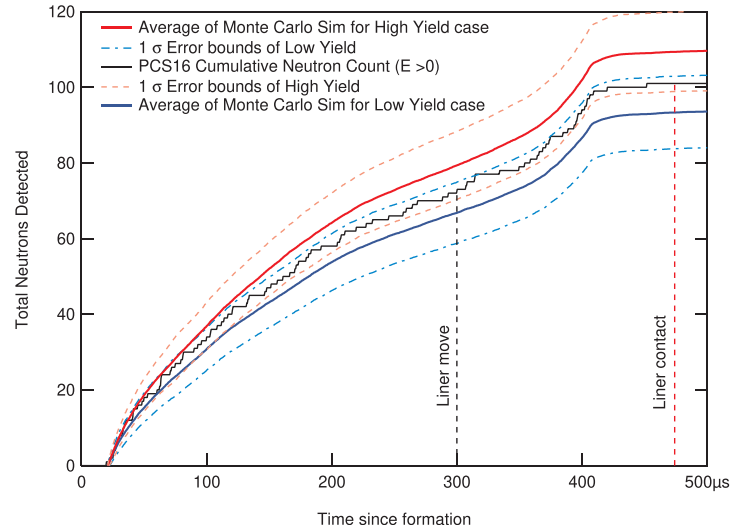


Figure 16. Monte Carlo simulation of the Poisson-process of detection events (thinning algorithm) method to evaluate upper and lower bounds for source emission rate $\lambda(t)$ that are consistent with the observed cumulative scintillator signal (black) on the PCS-16 compression shot.

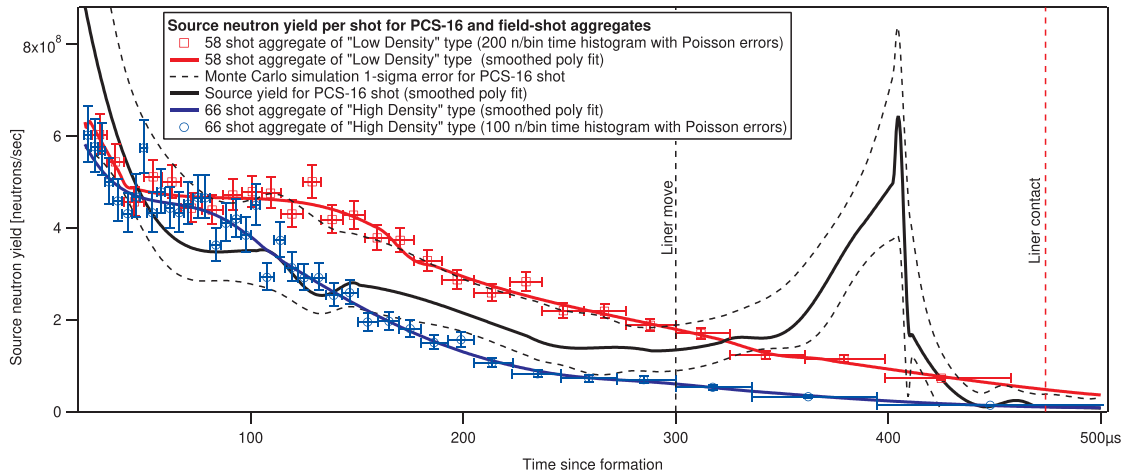


Figure 17. The PSD-identified neutron count rate scaled by MCNP calibration to neutrons per second emitted from the plasma, for PCS-16 in black, and the average number of neutrons/second/shot, for 66 similar uncompressed shots in the high-density category in blue, and the 58 shots in the low-density category in red. For the aggregate results of these two shot-categories we show both the time derivative of the smooth polynomial fits to the cumulative yield curves and the constant count box-histogram rate with Poisson uncertainty in the source rate. We see that before compression the PCS-16 neutron emission rate was in between the two categories and during compression the PCS-16 neutron rate significantly exceeds both categories of shots.

value of the detection rate, each trial function gives rise to $N_{MC} = 200$ instances of cumulative detection curves. The variation present in this set of randomly generated instances gives a standard deviation measure of what possible measurements are consistent with that trial function. The upper and lower trial functions are then varied iteratively until the experimental $c_n(t)$ data is maximally bracketed above by the one-sigma bound of the lower trial function and maximally bracketed below by the one-sigma bound of the upper trial function. See figure 16. The upper and lower trial functions then serve as an error estimate for the statistically plausible range of true cumulative neutron counts that are consistent with our measurements. Uncertainty in count rates can be found by fitting each

Monte Carlo instance of cumulative counts to the smoothing polynomial, then taking its time derivative, and tabulating its variation away from the mean rate at each time. The inferred rate with error is shown in figure 8. Final error estimates $N_{MC} = 1000$ were used to generate the variation in the neutron count rate.

Once the detection rate and error are quantified, the MCNP-determined calibration factor is applied to convert the total count rate from a set of eight scintillators into an inferred neutron yield (neutrons/second) emitted from the plasma source. In figure 17 the neutron yield vs. time for PCS-16 is compared with the low-density and high-density aggregates of similar control shots. The primary conclusion is that the PCS-16

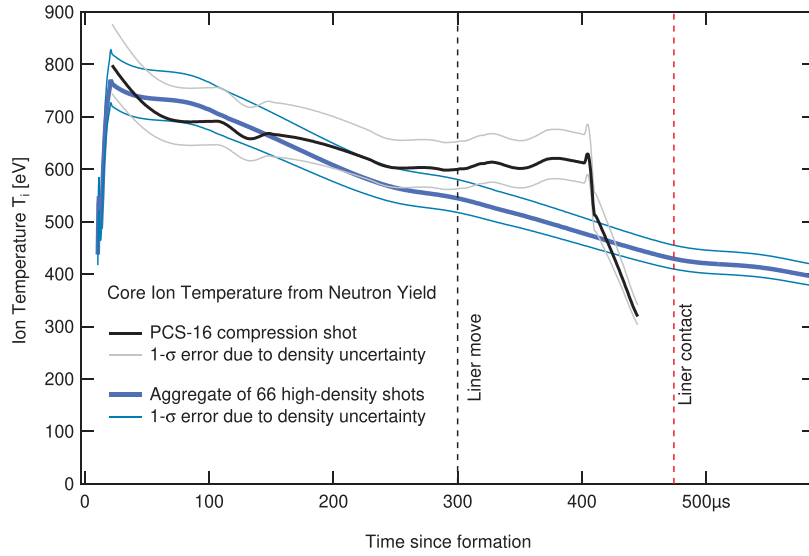


Figure 18. Ion temperature inferred from neutron yield and density. Error bands are due to the largest uncertainty in estimating the core density. Black trace shows the PCS-16 shot and is compared to the aggregate of 66 high-density field shots (in blue), which is representative of how $T_i(t)$ for the PCS-16 shot would have decayed if it had not been compressed. At the time of liner move the e-folding decay time for $T_i(t)$ for the high-density average is $\tau_{T_i} = 930 \mu\text{s}$, with a temperature of 545 eV at $t = 300 \mu\text{s}$. During the compression, the PCS-16 shot starts with $T_i(300 \mu\text{s}) = 600 \text{ eV}$ and rises a modest amount to $T_i(405 \mu\text{s}) = 629 \text{ eV}$ before rapidly decreasing below 400 eV in the final phase of the compression.

neutron yield was close to the high-density aggregate average prior to compression but rose to more than four-sigma (Poisson count error for PCS-16) above the average neutron yield for the uncompressed high-density shots during the compression period $300 \mu\text{s} < t < 465 \mu\text{s}$.

To calculate the ion temperature required to produce the measured value of plasma-sourced neutron yield, we generate a lookup table of neutron yields as a function of T_i and n_e at the plasma core, given a time-dependent Taylor-state model of the volume enclosed by each flux surface $V(\bar{\psi}; t)$, and assuming a parabolic profile of $T_i(\bar{\psi})$, and a plateau profile for $n_d(\bar{\psi})$ given by the fuel dilution ratio $f_D \equiv n_d/n_e$ times the n_e profile given by (10).

Neutron yield is calculated from $Y = \frac{1}{4} \langle \sigma v \rangle n_d^2$ where the DD reactivity is given by [61] as:

$$\langle \sigma v \rangle = 2.33 \times 10^{-14} T_i^{-2/3} \exp(-18.76 T_i^{-1/3}) \text{ cm}^3 \text{ s}^{-1} \quad (15)$$

for ion temperature T_i in keV. The prefactor is $\frac{1}{4}$ instead of $\frac{1}{2}$ because only half the DD fusion reactions produce a neutron. The volume of the plasma is discretized into 100 flux-shells with the specified T_i , n_d and volume, and the neutron generation density Y is calculated in each shell, resulting in a total neutron production after integrating over the volume of the plasma.

Then, to determine the ion temperature in the experiment, we combine the measured neutron yield with the measured electron density. Interferometers measure the chord-average electron density \bar{n}_e from which we infer the core n_e . The table then provides T_i .

We have considered values of f_D in the range 0.7–0.9. The relation between the variables is such that lower values of f_D

result in lower values of $n_d = n_e f_D$ for a given measurement of n_e . Lower n_d values require higher T_i values to achieve the same measured value for the neutron yield. Therefore, to report the most conservative estimates for T_i we are using the upper bound of $f_D = 0.9$. We might actually have more impurities resulting in lower f_D , but that would also require correspondingly higher T_i than what we are reporting.

By relating the neutron yield to the ion temperature we assume a Maxwellian distribution of ion velocities. In appendix F we discuss why we believe this is a reasonable working assumption.

The most conservative estimate for the ion temperature inferred from neutron counts on the PCS-16 shot, assuming $f_D = 0.9$, is a value of $T_i = 600_{-31}^{+46} \text{ eV}$ at time of the liner move ($t = 300 \mu\text{s}$), which increases to a maximum of $T_i = 629 \pm 50 \text{ eV}$ at $t = 405 \mu\text{s}$ during the compression. Results are shown in figure 18.

The modest increase in T_i during this rise can be interpreted via the compressional heating formula (1). Numerical variation of $\chi_i(t)$ and integration in time provide a best match model to experimental $T_i(t)$ as shown in figure 19. The decay of $T_i(t)$ in the early phase before compression is consistent with $\chi_i = 0.52 \text{ m}^2 \text{ s}^{-1}$ and initial $\tau_{Ei} = (a_0/j_{01})^2/\chi_i = 1.19 \text{ ms}$. This is with the initial minor radius $a_0 = 6 \text{ cm}$, and $j_{01} = 2.4048$. Therefore, in order for the thermodynamic model to match the average slope of experimental $T_i(t)$ after compression starts, it is necessary for χ_i to steadily increase to $5.0 \text{ m}^2 \text{ s}^{-1}$ at which point the equivalent τ_{Ei} value would have decreased to $122 \mu\text{s}$. Then, at $t = 405 \mu\text{s}$ the MHD crash happens and the χ_i value briefly jumps up to $13 \text{ m}^2 \text{ s}^{-1}$ with an equivalent initial τ_{Ei} value of only $47 \mu\text{s}$. Then, there is a prompt recovery with χ_i dropping back down to $6 \text{ m}^2 \text{ s}^{-1}$. The neutron-inferred evolution of ion transport will be compared to

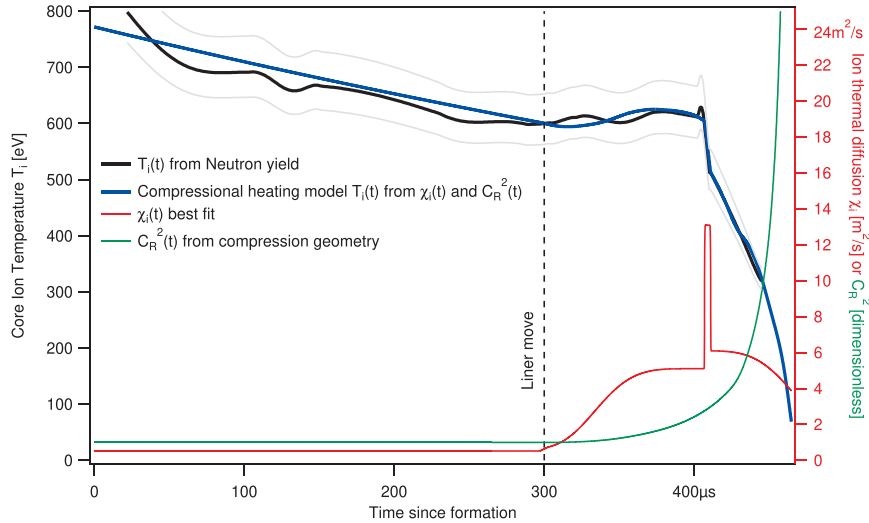


Figure 19. Thermodynamic model of the ion temperature using (1). The diffusion parameter $\chi_i(t)$ (red) was varied and numerically integrated using the PCS-16 compression trajectory $C_R^2(t)$ (green) until the best match for $T_i(t)$ was found.

MHD simulation results in section 5.2. Note that in interpreting the ion temperature evolution in this way, $\chi_i(t)$ describes all cooling mechanisms, and the variation of $\chi_i(t)$ includes the effects of changes in diffusive transport, changes in ion cooling by equilibration with electrons, and even changes in transport barriers that may exist.

Alternatively, the ion temperature during the first $100 \mu\text{s}$ of compression can be directly fit to the power-law heating formula, which yield a best fit of $\epsilon = 0.056 \pm 0.006$, and with the compression time $\tau_C = 138.8 \mu\text{s}$ implies an average thermal confinement time of $\tau_{Ei} = 143 \mu\text{s}$, which is close to the value determined from χ_i fitting shown in figure 19 which has a mean value of $\langle \tau_{Ei} \rangle = 156 \mu\text{s}$ over the interval $[324 \mu\text{s}, 405 \mu\text{s}]$ during which power-law heating is expected to be possible.

Equilibration of electrons plays an important role in cooling the ions in the time leading up to compression. Assuming an ion cooling timescale $\tau = 930 \mu\text{s}$ that is characteristic of the high-density aggregate $T_i(t)$ data, and an electron temperature $T_e = 211 \text{ eV}$, we find that the contribution to the ion cooling timescale due to equilibration with electrons is 2.2 ms implying that the ion cooling timescale due to transport is $\tau_{Ei} = 1.6 \text{ ms}$ before compression begins. For further details, see appendix E.

4.7. Evolution of asymmetry in the poloidal magnetic field during compression

With the results presented in the previous sections, an important task emerges to provide evidence for the prime cause for both the gradual increase in ion thermal transport implied by the neutron data and the sudden drop in electron and ion temperatures observed by several different diagnostics shortly after $t = 400 \mu\text{s}$. Fourier analysis of the toroidal modes present in the poloidal Mirnov data (figure 20(a)) reveals how resistive instabilities grow during compression and may explain why thermal transport changed during compression. We calculate the amplitude of the $n = 1, 2, 3$ toroidal modes of the

poloidal field measured in the six $R = 54 \text{ mm}$ (B54) probes (figure 20(b)), as well as the unwrapped phase of the mode with the offset of the phase angle at the time of the liner move subtracted to show a change of phase during compression (figure 21).

By the time of the liner move at $t = 300 \mu\text{s}$ the initial transient modes of CHI formation are damped out and we are left with a small amplitude of magnetic asymmetry $< 1\%$, which is comparable to the electrical noise floor of the Mirnov probe signal. From phase measurements of the $n = 1$ component, the initial magnetic mode has a near-constant phase angle, which is likely due to the drag from the edge field that diffuses into the conductive wall.

After the compression begins, there is a period of good symmetry for the first $40 \mu\text{s}$. Then, a dominantly $n = 1$ mode becomes detectable as it slowly increases in amplitude above the noise floor of the diagnostic, and experiences one e-folding of growth between $t = 340 \mu\text{s}$ and $368 \mu\text{s}$. Only after reaching this larger relative amplitude of 2.9% does the mode suddenly begin to observably rotate in the negative toroidal direction, with a rotation period of roughly $30 \mu\text{s}$. There is a general trend of amplitude growth for the remainder of the compression for all three mode numbers. During its growth, the magnetic mode completes a total of 1.79 revolutions before reversing direction late in compression after the $B_{\text{pol}}(R = 54 \text{ mm})$ signal has passed its peak value.

Supportive evidence for this rotation is found in a strong correlation between the magnetic fluctuations and similar fluctuations observed in the AXUV signal. The AXUV signal has a smooth rise up to $t = 355 \mu\text{s}$, at which point it experienced a downturn as part of a periodic dynamic. The onset of noticeable rotation of the $n = 1$ mode appears to coincide with the first minimum point in the AXUV signal. The decline of the X-ray signal is indicative of the loss of electron thermal energy from the core of the plasma, which could be triggered by the magnetic mode passing a threshold in amplitude. At the time of the first decline of the AXUV signal, the relative amplitude

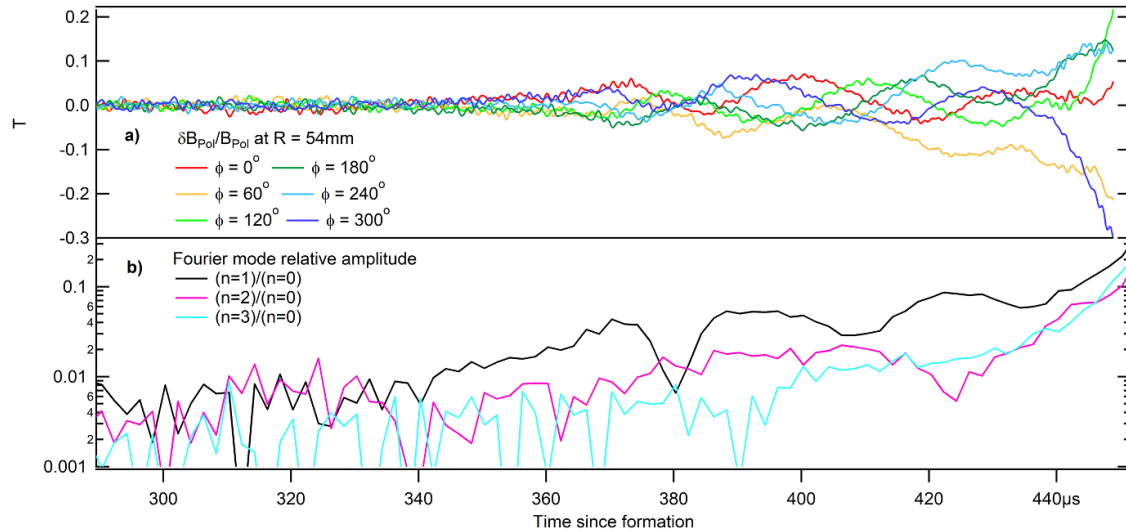


Figure 20. Appearance of toroidal $n = 1, 2, 3$ modes during compression. In subplot (a) the relative deviation from axisymmetry is shown for each of the six toroidal locations of Mirnov probes, showing $\delta B_{\text{pol}}/B_{\text{pol}}$. The relative amplitude of a Fourier decomposition with respect to the toroidal angle is shown in subplot (b), with $n = 1$ being the dominant mode growing up from a background of $<1\%$.

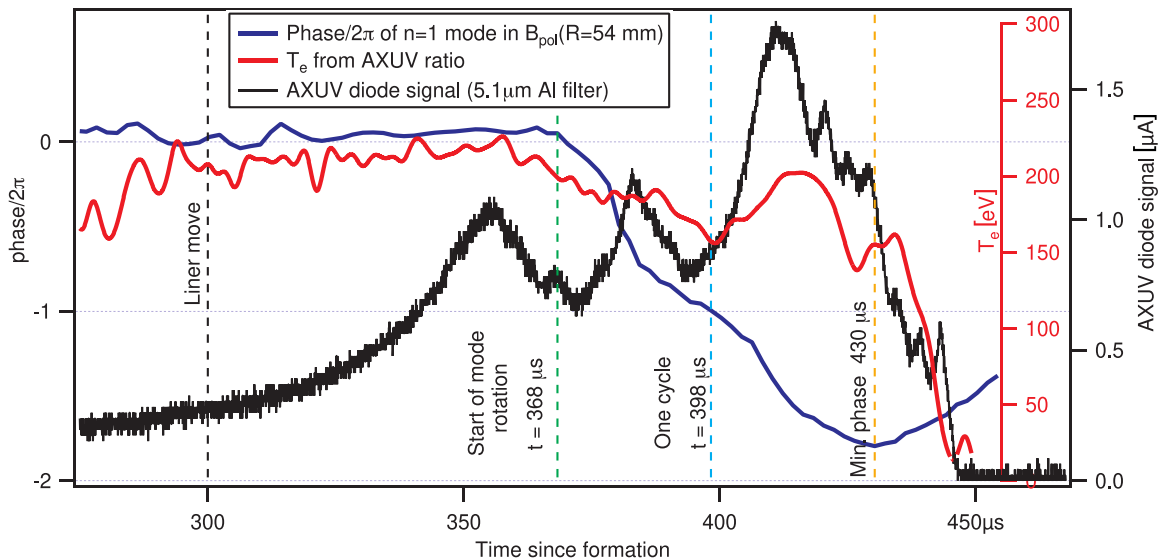


Figure 21. Evolution of the phase/ 2π of the poloidal magnetic $n = 1$ mode as determined from Fourier analysis of the 6 Mirnov probes at $R = 54$ mm (blue curve), compared to T_e from AXUV ratio (red curve) and AXUV diode current for the $51 \mu\text{m}$ Al filter channel (black curve). The general observation is a non-rotating locked mode at the $<1\%$ level of relative amplitude (see figure 20(b)) at the time of the liner move, which grows in amplitude without rotating until $t = 368 \mu\text{s}$ when the mode begins rotating in the negative toroidal direction with a period of approximately $30 \mu\text{s}$, completing 1.79 rotations before reversing direction in the final phase of compression. The T_e reading is nearly constant while the mode is not rotating, and only begins to fall when the AXUV diode signal reaches its first local maximum. The period of magnetic rotation matches cycle of dips in AXUV diode signal.

of the nonrotating $n = 1$ mode as measured at the wall is 1.6% . The subsequent rise in the AXUV signal once rotation begins could be indicative of a plasma reorganization that temporarily increases energy in the core of the plasma, which could be compatible with a dynamo action of a rotating $n = 1$ mode. The closely matched period of the two processes, magnetic and X-ray emission, is an indication of some linked mechanism between the core and the edge field dynamics. When a full cycle of the magnetic mode rotation is completed at $t = 398 \mu\text{s}$ and the AXUV signal reaches its second local minimum, the $n = 1$ mode relative amplitude reaches 4.6% in combination

with an $n = 2$ mode at 2% and $n = 3$ is just beginning to rise above the noise at 0.7% . Roughly at the time of this complete revolution point, the thermal crash is observed in the neutron yield data, then in the IDS, then in the AXUV ratio T_e , and finally in the Ohmic estimate of T_e .

We conclude in general from the experimental data of PCS-16, that given the evidence of near-constant electron inventory, which helps rule out significant increase in impurity content of the plasma as a cooling mechanism, it is fairly convincing that the observed rise in magnetic asymmetry is a prime cause of thermal transport increasing during compression. A more

complete understanding of the plasma dynamics observed in the experimental data can be gained from comparison with numerical stability analysis and MHD simulations in the following sections 5.1 and 5.2.

5. Comparison of simulation with experiment

It was shown in the previous section that the compression behaved well during the first two-thirds of its duration, up to $t \sim 400 \mu\text{s}$, $C_R \sim 1.5$, after which there was a significant change in the transport behavior of the plasma measured by several independent methods. In this section we explain the observed dynamics of the PCS-16 plasma with a combination of simulation and theoretical analysis. We first present a linear stability analysis (section 5.1) that connects to the observed evolution of the magnetic field asymmetry (section 4.7). We then present a three-dimensional MHD simulation (section 5.2) that illustrates what likely happened to the plasma during this $400 \mu\text{s}$ transition point as a result of exhausting the ability to rapidly increase the shaft current (figure 5) and maintain internal versus external toroidal magnetic pressure balance.

5.1. Linear stability analysis

To evaluate the plasma stability before and during compression, we use a Bayesian reconstruction method to analyze the Mirnov probe data and generate a series of representative Grad–Shafranov equilibria. A brief description of this method is found in appendix C. The equilibria are evaluated for their ideal and resistive stability at $5 \mu\text{s}$ intervals before compression and $20 \mu\text{s}$ intervals after compression. Due to the shape of the flux conserver, the last time that we are able to generate equilibria is $105 \mu\text{s}$ into compression. However, we will show in this section that stability is lost before that point.

Once we have equilibria, we analyze the growth rates of various plasma instabilities with the RDCON [62] and RMATCH [63] codes. RDCON calculates the resistive MHD stability based on the method of matched asymptotic expansions in full toroidal geometry, where the plasma is partitioned into an ideal outer region and a resistive inner region around each rational q surface. We seek equilibrium states that are both locally and globally stable. Global stability is approximated by RMATCH by considering the interaction between the two innermost integer- q surfaces (only if the q profile contains two such surfaces) effectively neglecting integer- q surfaces in close proximity to the wall. Using this technique, we have found compression trajectories for reactor models that remain stable until fusion conditions are reached [49, 50].

The equilibrium reconstruction shows that the q profile evolves slowly prior to compression (figure 22(a)). After the liner starts to move, the profile begins to drop, taking q_{\min} from 2.2 down to 1.4. Consequently, the magnetic axis drops through the $q = 2$ rational surface about $65 \mu\text{s}$ after liner move. The only other integer surface in the plasma is the $q = 3$ surface, which is always close to the LCFS. It is clear that there is always a reversed shear in the q profile, as the q_0 and q_{\min}

are separated, but this is a consequence of the assumed current density profile. Poloidal β is always assumed to be 5%, so pressure has a negligible effect on the q profiles. The assumed shape of the model q profile only considers the case of reversed shear near the core, which may overestimate the occurrence of instabilities because it does not include the more stable case of monotonically increasing q profile. Experimental measurements on PCS-16 are not able to distinguish between these two cases of q shear near the core and so we work with a more conservative test for instability, which may be an overestimate.

Both the reconstructed shaft and plasma currents are slowly dropping prior to the liner moving, but rise during compression (figure 22(b)). To accommodate the changing geometry, the Bayesian reconstruction is executed with limited flexibility in the profiles. Selecting the best approximation, we limit the shape of the current profile F' , which forced the shaft current and q_{\min} to be roughly proportional to one another. Because q_{\min} is more important when evaluating plasma stability, q_{\min} is fit accurately and the shaft currents of the evaluated equilibria are allowed to deviate from the experiment. Ultimately, the deviation is less than 20% and is deemed an acceptable approximation to compute the results.

Results of the linear stability analysis are summarized in figures 22(c) and (d), which show that the plasma was at least marginally stable until the $q = 2$ surfaces appeared within the plasma $65 \mu\text{s}$ after the liner started to move. At this point, a fixed MHD ideal $m/n = 2/1$ mode appears with a growth rate three orders of magnitude faster than the compression rate. This ideal mode is immediately followed by resistive modes (both tearing and interchange) that continue until the equilibrium is no longer calculable. The resistive growth rate is of the same order of magnitude as the compression rate, so it is not likely to be ignorable. Though these results show that the 2/1 mode continues for $20 \mu\text{s}$, in reality, it is likely that the instability will cause the equilibrium to quickly evolve to a configuration with 2/1 islands where the tearing mode will be able to grow more easily.

This stability analysis agrees fairly well with the other experimental data. As described in section 4.7, the plasma poloidal magnetic field shows a slowly growing, small amplitude $n = 1$ mode after the liner move. The linear stability analysis does not identify instability with growth rate above the pre-specified threshold during this time, but that may be due to the extra constraints required for the reconstructed equilibria. Around $65 \mu\text{s}$ after liner move, the phase of the $n = 1$ mode suddenly begins to rotate (as seen by the start of the oscillating phase in the Mirnov signal in figure 20(a)), coincident with the reconstructed q profile passing through the $q = 2$ surface and the stability analysis predicts that the equilibrium is strongly unstable to the 2/1 tearing mode. After this $q = 2$ crossing, it is observed that the $n = 1, 2, 3$ modes continue to grow for the remainder of compression up to a $\delta B_{\text{pol}}/B_{\text{pol}} \sim 20\%$ level. Once this transition into more unstable behavior has occurred, the plasma becomes nonaxisymmetric and the linear stability analysis is no longer applicable. We will need to utilize MHD simulations to provide insight into the dynamics later in compression.

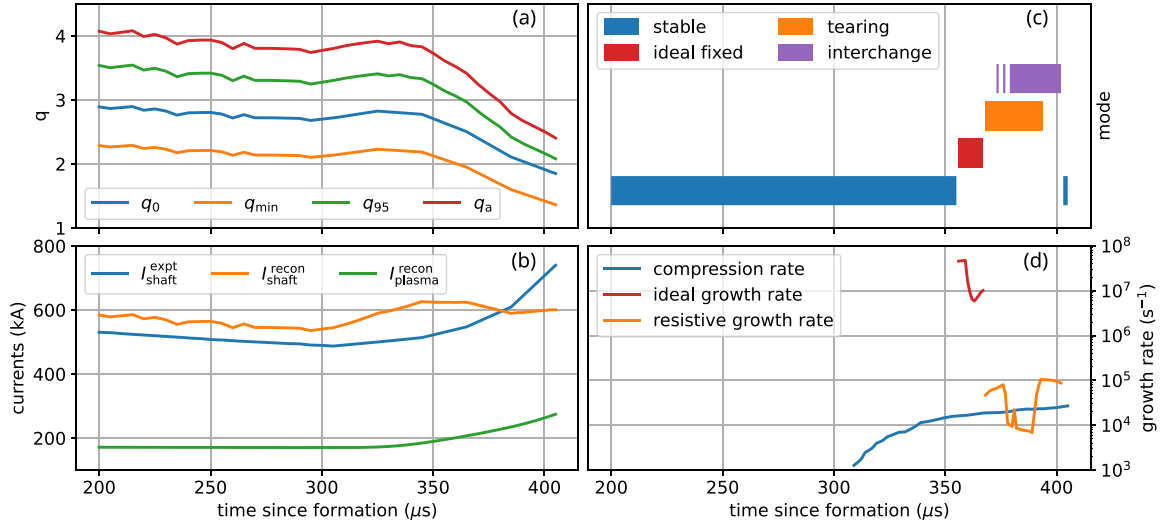


Figure 22. Results of Bayesian equilibrium reconstruction and linear stability analysis based on the Mirnov probe measurements of the PCS-16 shot: (a) Reconstructed safety factor values at the magnetic axis, minimum, 95% poloidal flux surface, and LCFS. (b) Measured shaft current $I_{\text{shaft}}^{\text{expt}}$, reconstructed shaft current $I_{\text{shaft}}^{\text{recon}}$, and reconstructed plasma current $I_{\text{plasma}}^{\text{recon}}$. $I_{\text{shaft}}^{\text{recon}}$ is permitted to deviate from $I_{\text{plasma}}^{\text{recon}}$ to optimize the match to q_{min} . (c) The existence of unstable modes in the reconstructed equilibria as calculated by RDCON. (d) Growth rate of ideal (red) and resistive (yellow) modes as calculated by RMATCH. The resistive growth rate is applicable to both tearing and interchange modes. Modes that grow faster than the compression rate are deleterious to plasma confinement.

5.2. MHD simulations to match experimental signals

For MHD simulation of the PCS-16 experiment we use VAC [39, 64], a versatile framework providing various numerical schemes to solve advection equations in curvilinear geometries. Here, we employ the Total Variation Diminishing Lax–Friedrich (TVDLF) scheme with a projection method to keep the magnetic field divergence-free. Resistive evolution of the plasma is modeled assuming an isotropic resistivity whose value is equal to the local temperature-dependent parallel Spitzer resistivity (the dependence on Z_{eff} is described in section 14.10 of [65]). Momentum transport is included using a uniform isotropic viscosity $\approx 6 \mu\text{Pa}\cdot\text{s}$, with the plasma mass modeled as being pure deuterium. Temperatures for electrons and ions are independently evolved and are equilibrated on a classical time scale. Cross-field heat transport uses independent anomalous diffusivity for electron and ion thermal energy. Note here that the thermal diffusivity parameter χ as implemented in the VAC transport model differs from the $\chi_E = (a_0/j_{01})^2/\tau_E$ as defined for the analytic circular cross section model in section 2.1. The model for heat transport along field lines uses a hyperbolic method for physically realistic fast transport. The boundary conditions imposed at the metal walls include zero flux diffusion, zero mass flux, and a low plasma temperature. The thermal conduction to the cold wall results in a cold layer of plasma near the wall.

The simulation is initialized with a magnetic equilibrium representing the flux surfaces of the precompression plasma, obtained by solving the Grad–Shafranov equation for the poloidal flux field $\psi(R, Z)$. The wall is approximated as a flux conserver with no frozen-in flux, providing a constant ψ boundary condition. The shape of the current profile is given by $F' \propto 1 - 2\bar{\psi}^2 + \bar{\psi}^3$ where $F(\bar{\psi}) = rB_\phi$, and the normalized flux coordinate $\bar{\psi}$ is defined to be linear in ψ with $\bar{\psi} = 0$ at

the magnetic axis and $\bar{\psi} = 1$ at the LCFS. The plasma thermal pressure p profile is initially $p/p_0 = 1 - 3\bar{\psi}^2 + 2\bar{\psi}^3$

The compression process is modeled by deforming the conformal curvilinear mesh as a function of time. In VAC, plasma compression is interleaved with advancing MHD equations in time (a form of operator splitting). The geometry is updated every 100 MHD time steps, which is essentially continuous, as the time step varies from 5×10^{-11} s at the start of the simulation to 3×10^{-12} s at the end. Remeshing is done 32 times during the simulation to deal with the strong deformation of the geometry. The meshes are logically rectangular with 50 cells in the radial direction in each mesh. The number of cells in the axial direction N_z is increased when remeshing, from $N_z = 363$ at the start to $N_z = 1683$ at the end of the simulation, to keep the aspect ratio of the cells near unity. In three-dimensional simulations, the two-dimensional mesh revolves about the z -axis and gives 32 cells in the toroidal direction. Typically, we run the VAC simulation for $100 \mu\text{s}$ before beginning the compression sequence to allow any initial transients to dissipate. This also provides a time to observe the trends in resistive flux decay and heat transport that unfold as a model of uncompressed plasma dynamics.

To provide a simulation that closely matches experimental Mirnov signals, we conducted a sequence of VAC runs in which we varied the electron thermal diffusivity χ_e , both in its initial value and how it changed during compression. This led to the development of a representative simulation (run SR981).

Simulation SR981 uses a transport model with nonuniform electron thermal diffusivity $\chi_e(\bar{\psi})$, increasing exponentially with $\bar{\psi}$ and varying in time during the compression, in order to improve the agreement with experimental Mirnov signals. The core value was held constant at $\chi_{\text{core}} = 40 \text{ m}^2 \text{ s}^{-1}$ and the edge value started at $\chi_{\text{edge}} = 40 \text{ m}^2 \text{ s}^{-1}$ and was increased to $\chi_{\text{edge}} = 100 \text{ m}^2 \text{ s}^{-1}$ at $300 \mu\text{s}$ (liner move) and to $\chi_{\text{edge}} = 200 \text{ m}^2 \text{ s}^{-1}$ at

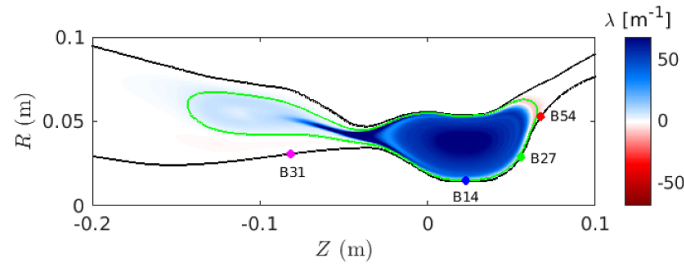


Figure 23. Distribution of simulated plasma current intensity $\lambda(r, z) \equiv \mu_0 J_{\parallel} / B$ at high compression, at $t = 450 \mu\text{s}$. At this time a magnetized plasma daughter toroid is being ejected back toward the gun. The poloidal flux of the ejected toroid is about 1 mWb. For comparison the poloidal flux of the magnetic axis of the compressed plasma is 14.7 mWb. The plotted green curve is the poloidal flux contour 0.7 mWb.

$370 \mu\text{s}$. The ion thermal diffusivity is uniform and constant at $\chi_i = 5 \text{ m}^2 \text{ s}^{-1}$ (we note that the evolution of the ion temperature is of little consequence in the simulation and this parameter is unrelated to experimental observations). The simulation exhibits a thermal confinement time $\tau_E \approx 84 \mu\text{s}$, immediately prior to compression. For comparison, for the parameters of the simulation, the neo-Alcator scaling law gives $\tau_E = 103 \mu\text{s}$ [66].

For SR981 we used the following initial conditions. The poloidal flux linking the magnetic axis is 17.5 mWb. The shaft current is 521 kA. Initial ion density is uniform with $n_i = 10^{20} \text{ m}^{-3}$ and, for simplicity, $n_e = n_i$. Initial temperature profiles peak with temperatures at the magnetic axis set to $T_e = 200 \text{ eV}$ and $T_i = 500 \text{ eV}$. The core plasma pressure $p_0 \approx 11 \text{ kPa}$ is determined by temperature and density profiles. Initially, the plasma velocity is toroidal, with angular velocity proportional to $1 - \bar{\psi}$, zero near the wall and 30 km s^{-1} at the magnetic axis. The initial plasma has a toroidal plasma current 199 kA and a safety factor profile with $q_0 = 1.4$ and $q_{95} = 5.3$. Resistivity of the plasma uses a value $Z_{\text{eff}} = 3$ chosen in order to match the precompression decay of the plasma current. We expect that a neoclassical resistivity model would yield similar results with lower Z_{eff} .

The shaft current in the simulation is programmed to follow the measured experimental waveform. This sets the toroidal magnetic field value at the gun end of the compression chamber. The detailed distribution of the current along the shaft depends on the current flowing from the wall into the plasma that evolves according to the MHD equations with flux-conserving boundary conditions.

One of the more dramatic observations that can be made regarding the simulated behavior is the occurrence of a significant MHD event that happens soon after the transition point in experimental behavior near $t = 400 \mu\text{s}$. When the externally-applied shaft current ramp reaches its peak, the resulting toroidal pressure imbalance generates significant currents in the edge plasma and ejects a ‘daughter toroid’ back into the gun, as anticipated by simpler considerations described in section 2.2. Figure 23 shows a frame from the simulation at the moment of ejection.

This phenomenon is experimentally observed in the time-evolution of the signals from the four poloidal measurement positions of the Mirnov probes in the chamber, shown in

figure 24. Solid traces are experimental signals and dashed traces are synthetic. The key evidence for this daughter toroid ejection is in the B31 Mirnov trace, which rises between 400 and 450 microseconds. At this time, the plasma should be receding from the probe location if the poloidal field were fully trapped by the converging wall into a decreasing volume. However, the experimental signal from the B31 Mirnov probe arises over this time period, as does the synthetic trace.

The ability of the experiment to produce and diagnose these phenomena, as occurs in the simulation, is a significant part of fulfilling the goal of PCS-16 to improve our understanding of the plasma behavior when the external shaft current ramp falls below internal toroidal pressure, as seen in figure 5.

The impact this ejection event had on the plasma thermal confinement is fairly clear in experiment. At the time of ejection, there is a $4.6\% n = 1$ mode, which would mean the release of magnetic energy into the daughter toroid is not going to be a perfectly axisymmetric process, likely to provide a fast growing ideal instability of the plasma boundary beyond what was considered in the linear stability analysis of section 5.1. We only had one toroidal probe location at the $R = 31 \text{ mm}$ position so there was no direct measurement of how asymmetric the ejection was, however we have all the remaining diagnostics showing rapid energy loss following the onset of this event. The VAC simulation shows the ejection as a toroidally symmetric extension of the edge of the main plasma, and while there is some energy loss involved, it is much less than disruptive than what is seen in experiment.

As an example of how the flux ejection is less disruptive in the simulation, the height of the peak on the $B_{\text{pol}}(R = 54 \text{ mm})$ curve (red) in figure 24 is higher in the simulation than in experiment. This suggests a faster decay of plasma current and poloidal flux in the experiment compared to the simulation, as previously described in section 4.3. In addition, the three-dimensional simulation did not reproduce the $n = 1$ mode observed in the experiment (figures 20 and 21). The simulation did develop a small $n = 1$ instability, but later, at $t \approx 457 \mu\text{s}$. A difference in the q profile between simulation and experiment may be the reason for this discrepancy. It is also possible that 32 cells in the toroidal direction are not sufficient to fully capture localized distortions in the magnetic flux to provide pathways for energy to reorganize within the simulation.

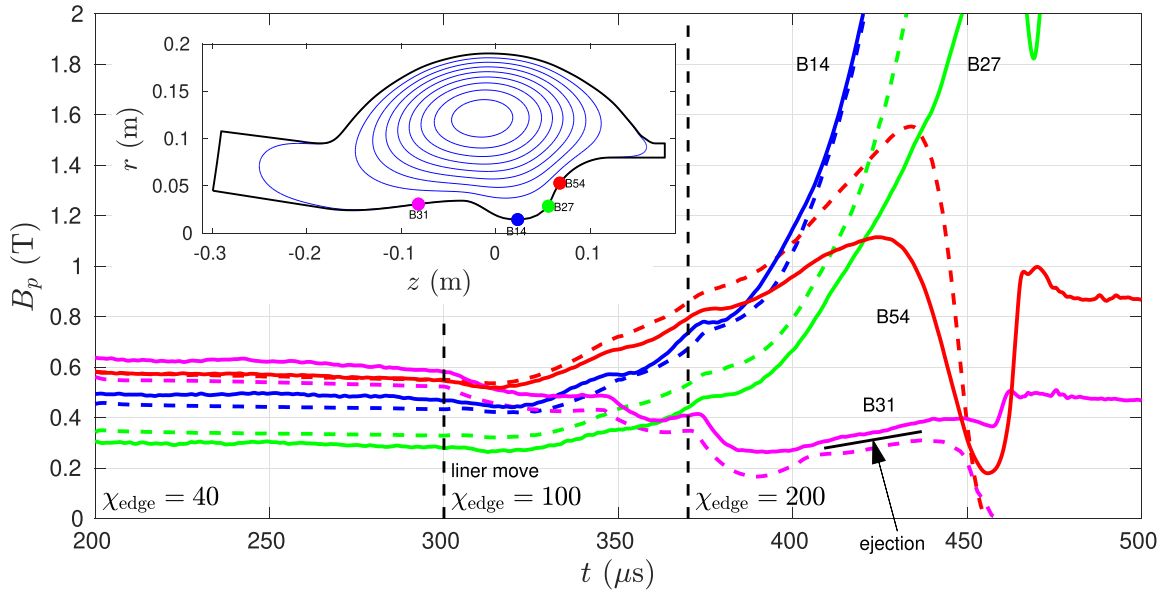


Figure 24. Comparison of Mirnov probe readings of poloidal magnetic field from the PCS-16 experiment (solid) and three dimensional MHD simulation (run SR981, dashed). The inset plot shows the location of the Mirnov probes on the shaft and contours of poloidal flux on the pre-compression poloidal cross section. The simulation used a transport model with electron thermal diffusivity varying as described in the text, the key times and values are indicated on the plot. The increasing poloidal field on the B31 Mirnov probe (magenta curve), due to the developing ejection of a magnetized plasma daughter toroid, is indicated on the plot.

Given the ability of MHD simulations to reproduce flux ejection events in the form of a daughter toroid the consequences for thermal confinement of the core plasma of this event are relatively smaller in the simulation than in the experiment and stand as an important distinction between the simulation and experimentally observed behavior. The interpretation that seems most plausible is that VAC correctly captures the 2D nature of this free boundary instability, and as a result of being closer to an axisymmetric state it suffers less of an impact on the simulated thermal confinement at the core. The experiment seems to be contrapositive to this lack of symmetry during the ejection that caused a significant impact of core thermal confinement.

The primary result of this detailed study of the mechanism of toroidal pressure imbalance causing this daughter toroid ejection event is that we see clear ways to avoid this happening in future MTF designs. The fact that the PCS-16 plasma compression maintained good axisymmetry during the first two-thirds of compression while the external shaft ramp was actively maintaining toroidal pressure balance demonstrates that active control of shaft current is an effective means of stabilizing this nonlinear free-boundary perturbation.

The simulations can also be used to understand the relative size of heating and cooling mechanisms in the early phase of PCS-16 compression. Figure 25 shows that the cooling of ions by collisions with electrons rises during compression, overall remaining similar in magnitude to the heating power due to compression. The initial rapid increase in the cooling is not intrinsic to compression but rather is due to the change in electron transport that was imposed in the simulation at $t = 300 \mu\text{s}$ in order to better match the Mirnov data. Increasing

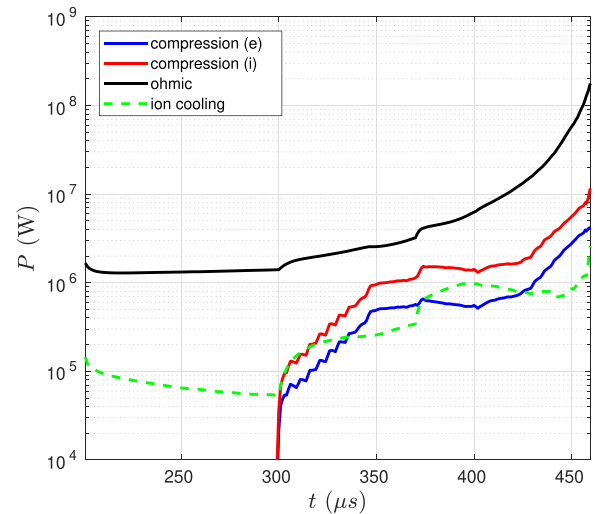


Figure 25. Comparison of heating and cooling mechanisms in the simulation (VAC run SR981). Electron compressional heating (blue), ion compressional heating (red), Ohmic heating (black) and ion cooling by equilibration with electrons (green dashed). During compression the equilibration cooling increases to remain similar in magnitude to compressional heating.

density also plays a role in increasing the cooling power of collisions. The evolution of electron transport undoubtedly differs in the experiment, but the basic picture may be similar. The experimentally determined $\chi_i(t)$, an effective transport coefficient that includes collision cooling of ions, also shows a rise during early compression. This rise may be due to degradation of electron confinement due to increasing MHD

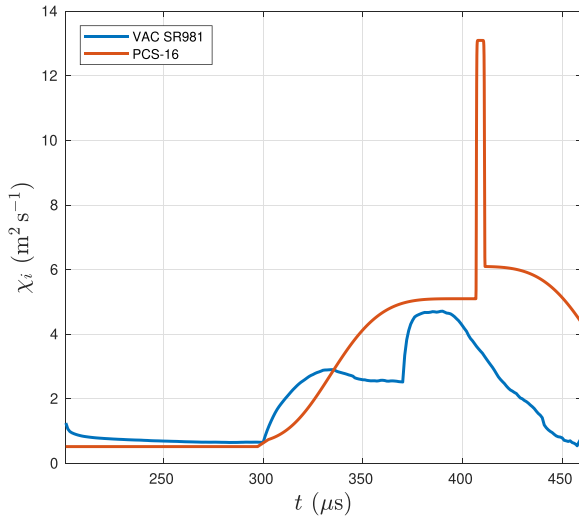


Figure 26. Effective ion thermal diffusivity χ_i as a function of time. *Blue:* simulation VAC-SR981, shows the cooling power applied to ions by equilibration with electrons as an equivalent diffusivity. *Red:* PCS-16 experiment, shows the holistic value determined from PCS-16 experimental data, from figure 19. Changes in electron transport, imposed step wise in the simulation at $300 \mu\text{s}$ and $370 \mu\text{s}$, give rise to rapid increase in ion cooling power.

activity and consequent enhancement of collisional cooling of ions. Figure 26 compares the experimental results in the equilibration cooling power in the simulation.

6. Improvements for future devices

The observed, heightened transport during the PCS-16 compression has the following root causes: marginally stable initial q -profile, electron-ion temperature difference, insufficient initial τ_E , and eventual imbalance of the toroidal magnetic pressure. For each of these causes, we will now detail the pathways leading to heightened transport and describe steps that can be taken to improve performance in future plasma compression experiments. With these improvements, demonstrations of significant heating to fusion conditions becomes feasible in the next step of this line of research.

Initial q -profile: Early time growth of the $n = 1$ mode to more than 1% of the total field, as discussed in section 4.7, can provide a pathway to increased electron thermal transport through stochastization of the magnetic field [67, 68]. The occurrence of the observed $n = 1$ mode was most likely a consequence of the initial q -profile of the plasma at the start of compression being marginally stable to resistive tearing modes. To deal with this mechanism, a more stable configuration can be created with proper choice of initial q -profile. Recent theoretical work ([50], for example) explored how the stability of plasma compression depends on the q -profile and pointed out the requirement to operate in a particular range of q . Fine control of the q -profile can be accomplished on a fast-CHI device by adjusting the rate at which currents are applied to the formation electrode and the center shaft during CHI formation (as described

in section 3.2), as well as by adjusting the axial distribution and total amount of poloidal flux in the Marshall gun, and lastly with the shaft current at the start of compression (by changing either the peak shaft current or time that compression starts). Optimization of the CHI formation dynamics, combined with MHD stability modeling and accurate equilibrium reconstruction of experimental plasmas can be applied to improve the initial magnetic geometry used in future experiments to avoid instabilities.

Electron-ion equilibration: On PCS-16, electrons were significantly cooler than ions, which provided a pathway for ion cooling at a rate which was proportional to plasma density. This temperature difference between the two populations is caused by a number of factors. The initial plasma just after CHI formation begins with relatively hot ions. We believe this is due to the rapid stagnation of CHI-driven flows as the Alfvénic plasma flow abruptly comes to rest within the target chamber. Due to the mass difference between electrons and deuterium ions (a factor of 3670), the forward kinetic energy of the plasma during ejection from the Marshall gun is converted to a significant average thermal particle velocity for the ions after stagnation, yet it amounts to an insignificant thermal energy increase for the electrons. This ion heating mechanism is well known in the compact torus community [6, 69], as is the fact that magnetic reconnection also preferentially energizes the ions [6, 43]. Thus, just after forming, the ST plasma can have a relatively cool electron temperature of a few tens of eV, while the ions can begin near 1 keV (PCS-16 measurements shown in figures 12 and 18). Ohmic decay of the high initial plasma current rapidly heats the electrons. However, it does not bring them fully up to the ion temperature. Also, due to the small overall size of the PCS-16 device, the electron energy confinement time ($\tau_{Ee} = 52 \mu\text{s}$, section 4.4) is short compared to the ion energy confinement time and ion-electron equilibration time ($\tau_{Ei} = 1.6 \text{ms}$ and $\tau_{eq} = 2.2 \text{ms}$, section 4.6). There was no external heating of electrons used to compensate for these effects. This issue of $T_e \ll T_i$ can be avoided in several ways. Future devices that have an initial radius at least a factor of ≈ 3 times larger than the SPECTOR/PCS-16 design will naturally result in a longer electron energy confinement time, providing more time for ion-electron equilibration to occur. Likewise, operating at higher density to make a faster ion-electron equilibration time will bring the temperatures together before compression begins. Lastly, RF heating the plasma prior to compression can raise the electrons' temperature to that of the ions. Hotter electrons would also slow the growth of resistive instabilities, generally enhancing confinement.

Increased initial τ_E/τ_C : PCS-16 compression time was only comparable with initial overall energy confinement time of the plasma, not several times faster as would be required to expect significant heating. One important consideration with this third issue is that compression speed could be increased for the same size of device by using a thinner solid liner wall, however if the liner is too thin it would become more prone to buckling. Alternatively a

lighter and softer material could be used to get faster compression, such as pure lithium rather than aluminum, but with some added practical complications of mechanical handling and providing structural integrity against a vacuum/atmosphere pressure difference. Also, simply going to a larger device size can help this heating ratio as the energy confinement time generally scales at least as fast as $\tau_E \sim R^2$ [65, 66] while the compression time scales like $\tau_C \sim R/v_{ave}$, with maximum average velocity v_{ave} that is only weakly dependent on the device size. This constant-velocity scaling is useful because it preserves drive pressure and rotational stress (the case of a rotating fluid liner) for the same trajectory; this helps maintain engineering feasibility. Therefore the ratio that determines expected heating would follow $\tau_E/\tau_C \sim R$ or even faster. Overall there are several engineering routes to increase this heating ratio for future plasma compression experiments.

Control of toroidal magnetic pressure balance: The final effect to be considered here of the ‘disruption-like’ ideal instability of the daughter toroid ejection event, which was likely large enough in asymmetric perturbation amplitude at the core of the plasma that both ion and electron confinement would be directly affected, thus providing a pathway to rapid cooling. The primary cause of this event was an imbalance in the toroidal magnetic pressure due to shaft current falling below the predicted necessary value, simply due to the choice of capacitor bank size. However, in future designs it is straightforward to have a larger external power supply that can apply a shaft current ramp extending deeper into compression. It may also be feasible to engineer a liner trajectory which results in the formation of a fully closed poloidal circuit when it contacts the center shaft, thereby disconnecting the plasma region from any external volume into which anything could be ejected, naturally maintaining toroidal flux conservation within the fully closed compression region. A rotating liquid metal liner naturally allows for some independent control of fluid velocity at the point of contact with the shaft, better enabling a ‘soft’ contact that does not result in jetting events. Choice of a shaft geometry with conical features near the ends can allow this first point of electrical contact to happen early in compression at larger radius rather than late in time when the contact speed is higher.

Careful experiment design informed by accurate modeling can address all four of these factors, thereby reducing transport and increasing heating. Future progress in MTF research will depend on coupling resistive MHD, fluid and structural dynamics simulations to model realistic dynamics during compression. Many of the dynamics needed to calibrate such simulations were directly observed for the first time in PCS experiments. We now have the understanding needed to navigate around these instabilities so that future MTF devices can be optimized to achieve significant heating and demonstrate fusion conditions.

7. Concluding remarks

In this work, we demonstrate how a high-performance compact ST plasma can be compressed within an imploding metal liner in a well-diagnosed subscale exploratory plasma physics experiment that provides a foothold in a new regime of fusion research. The PCS-16 experiment demonstrated compression that was significantly faster than the plasma resistive decay time, maintaining a significant fraction ($\sim 77\%$) of its initial poloidal flux up to a compression factor of $C_R = 1.91$ and at least $\sim 30\%$ of its flux up to a compression factor of $C_R = 8.65$. With proper lithium coating procedures and well-engineered implosion dynamics, we were able to increase the plasma density during compression consistent with a particle confinement time significantly longer than the compression time, $\tau_p \gg \tau_C$. Impurity ingress to the core of the plasma remained below our detection limit throughout the compression.

Poloidal magnetic field and plasma temperature (T_e, T_i) measurements during the first two-thirds of compression were consistent with electron heating from a combination of compression-enhanced Ohmic heating and compressional heating, which together approximately matched cooling due to transport and radiative losses. Compressional heating of the ions was nearly balanced with cooling. Modeling this cooling as a transport diffusivity χ_i , we found it began small, but then grew slowly in correlation with the observed growth of the toroidal $n = 1$ asymmetry, as well as with the trend of increased cooling due to equilibration with the colder electrons as the plasma density increased during compression. In section 6, we described feasible strategies for overcoming the mechanisms for these transport pathways, thereby enabling compressional heating to dominate the power balance in future MTF devices. The primary improvements we recommend are as follows: (1) to optimize the initial q -profile to better avoid resistive and ideal instabilities, (2) to generate a plasma with $T_e = T_i$ at the start of compression to avoid electron collision as a cooling mechanism for the ions by increasing the device radius or other possible methods, (3) to minimize compression time so that τ_E/τ_C is maximized by using a lighter liner material such as lithium and (4) to maintain toroidal magnetic pressure balance between the ST plasma and the Marshall gun actively via a sufficient external current supply and/or passively via a well-engineered liner contact that fully encloses the plasma compression volume.

Direct observation of MHD behavior during plasma compression, combined with predictive simulations and theory, provides highly valuable guidance for advancing the intermediate-timescale MTF approach being developed by General Fusion. As described in sections 4.7 and 5.1, the slow $n = 1$ mode growth observed during compression is qualitatively in agreement with a linear stability analysis, which predicts crossing through an ideal instability at $q_{min} = 2$ at the time the $n = 1$ mode begins to rotate in the experimental plasma and the AXUV signals begin to oscillate. Shortly after the time ($t = 385 \mu s$) when we expected an axial displacement instability or daughter toroid ejection caused by an

externally applied shaft current falling below the balance point with internal plasma toroidal field pressure (section 5.2), we observed direct evidence of this predicted plasma displacement in the magnetic probes. Several independent measurements indicate rapid loss of plasma thermal energy immediately following this MHD event, as covered throughout section 4. The analysis of plasma dynamics on PCS-16 indicates that optimizing the initial plasma q -profile and maintaining toroidal magnetic pressure balance with the external volume are essential requirements for thermal confinement during compression. As detailed in section 6, we have practical methods for implementing these improvements in future devices.

PCS-16 and the PCS experimental campaign have demonstrated that significant volumetric compression of an ST plasma is practical to explore with experimental fusion devices. In light of these results, we believe that next-generation MTF demonstrations can achieve more stable plasma compression and reach greater fusion yields. Linear stability analysis of other compression geometries shows that MHD-stable compression is possible when the initial plasma q -profile is correctly selected [49, 50]. The good agreement of simulations with PCS-16 lends confidence to the applicability of these analyses to designing larger scale MHD-stable MTF systems. Liquid metal liners and solid liners in alternate configurations, have the ability to close the poloidal circuit surrounding the main plasma toroid at some time early in compression, thereby disconnecting from the inductance of the Marshall gun and eliminating the need for an external shaft current ramp beyond the initial stages of compression. Drawing from the experience of PCS experiments and other devices, the next phase of larger MTF experiments is planned with a reusable compression system comprising a solid lithium liner to be compressed by high power theta-pinch coils. An electromagnetic compression driver will allow a larger initial ST plasma radius than what is practical in a highly explosive driven implosion. Larger initial size is also enabled by compressing the liner via a theta-pinch rather than a Z-pinch approach. Increasing the radial scale of the device by a factor of 5 to approach the scale of a demonstration reactor will improve the initial thermal energy confinement time τ_E by a factor of 25 or more, while for constant liner launch velocity the compression time τ_C scales roughly proportional to radius. This improves the τ_E/τ_C ratio at least five-fold, with a corresponding increase in the expected heating exponent ε of the thermal scaling law through the relation (3). At larger radial scales, the electrons and ions can be allowed to come further into thermal equilibrium before compression. In addition, a reusable compression system will enable more compression shots to be completed with the same hardware and provide better diagnostic access, both of which improve the ability to learn from these experiments. These next-generation experiments will be another significant step toward demonstrating that MTF is practical and commercially viable as an energy production technology.

Acknowledgments

This work was supported by funding from the Government of Canada through its Strategic Innovation Fund (Agreement No. 811-811346). The funding source had no involvement in: the study design; the collection, analysis and interpretation of data; the writing of the report; and the decision to submit the article for publication. We thank David Plant for useful conversations and encouragement of the manuscript. We thank Martin Cox for insightful comments that improved the manuscript. We would very much like to thank Pacific Blasting, who helped to make this project possible as well as the partnerships with the TRIUMF particle accelerator center and Krzysztof Starosta of Simon Fraser University. We would like to thank Andrew Higgins and the Shock Wave Physics Group at McGill University for expertise that supported the diagnostics and design of the compression system. We would also like to thank the full team at General Fusion for their dedication in making this happen.

Appendix A. Derivation of MTF scaling formula

The general form of the compression-diffusion equation can be stated in terms of the convective time derivative of entropy, for general adiabatic index γ ,

$$\frac{d}{dt} \left(\frac{p}{n^\gamma} \right) = \frac{1}{n^\gamma} \nabla \cdot (n \chi_E \nabla T). \quad (16)$$

Modeling the torus as a periodic cylinder with minor radius $a(t) = a_0/C_R(t)$, we use minor-radius coordinate ρ , we obtain:

$$\frac{d}{dt} \left(\frac{p}{n^\gamma} \right) = \frac{1}{n^\gamma} \frac{1}{\rho} \frac{\partial}{\partial \rho} \left(\rho n \chi_E \frac{\partial T}{\partial \rho} \right). \quad (17)$$

Simplifying this with $\gamma = 5/3$, $p = nT$, and assuming no loss of plasma particles ($n \sim C_R^3$) and spatially uniform density we have:

$$\frac{d}{dt} \left(\frac{T(\rho, t)}{C_R^2(t)} \right) = \frac{1}{\rho} \frac{\partial}{\partial \rho} \left(\rho \chi_E \frac{\partial}{\partial \rho} \left(\frac{T(\rho, t)}{C_R^2(t)} \right) \right). \quad (18)$$

With spatially uniform (but possibly time dependent) value of χ_E , this has a closed-form, self-similar solution that enables exploration of the compression dynamics:

$$T(\rho, t) = T_0 C_R^2(t) \exp \left(-\frac{j_{01}^2}{a_0^2} \int_0^t \chi_E(t) C_R^2(t) dt \right) J_0 \left(\frac{j_{01}}{a_0} C_R(t) \rho \right), \quad (19)$$

where $j_{01} = 2.4048$ is the first zero of the Bessel function J_0 , and T_0 is the central temperature at $t = 0$. This is the general result shown in section 2.1 (1).

Setting $C_R(t) = 1$ and with constant χ_E , gives the case of no compression:

$$\begin{aligned} T(\rho, t) &= T_0 \exp\left(-\frac{j_{01}^2 \chi_E}{a_0^2} t\right) J_0\left(\frac{j_{01}}{a_0} \rho\right) \\ &= T_0 \exp\left(-\frac{t}{\tau_E}\right) J_0\left(\frac{j_{01}}{a_0} \rho\right). \end{aligned} \quad (20)$$

Where the thermal energy confinement time must be related to χ_E via:

$$\tau_E = \left(\frac{a_0}{j_{01}}\right)^2 \frac{1}{\chi_E}. \quad (21)$$

For the case of when χ_E is constant we can find a trajectory where the general formula (19) reduces to a simple power law form $T_0 C_R^\epsilon$, analogous to the adiabatic case, but with an exponent $\epsilon < 2$ that corresponds to realistic losses. The time-dependent part of (19) can be rewritten:

$$T(t) = T_0 C_R^2(t) \exp\left(-\frac{1}{\tau_E} \int_0^t C_R^2(t) dt\right) \equiv T_0 C_R^\epsilon(t). \quad (22)$$

The exponential term can be manipulated as:

$$\begin{aligned} \exp\left(-\frac{1}{\tau_E} \int_0^t C_R^2(t) dt\right) &= C_R^{\epsilon-2}(t) \\ \frac{1}{\tau_E} \int_0^t C_R^2(t) dt &= (2-\epsilon) \ln C_R(t) \\ \frac{1}{\tau_E} C_R^2(t) &= (2-\epsilon) \frac{d \ln C_R(t)}{dt} \\ &= (2-\epsilon) \frac{1}{C_R(t)} \frac{dC_R(t)}{dt}, \end{aligned} \quad (23)$$

yielding a differential equation for $C_R(t)$ as:

$$\frac{dC_R(t)}{dt} = \frac{1}{(2-\epsilon)\tau_E} C_R^3(t). \quad (24)$$

This has a solution of the form:

$$C_R(t) = \left(1 - \frac{t}{\tau_C}\right)^{-1/2}, \quad (25)$$

where τ_C is the time at which the characteristic radius goes to zero. Through (24) that time has a value of

$$\tau_C = \frac{(2-\epsilon)\tau_E}{2}. \quad (26)$$

From this result (4) and (3) are simple rearrangements.

This solution, corresponding to $R(t) = R_0 \sqrt{1 - t/\tau_C}$, has the general characteristic common to many liner compression concepts where the inner surface of a metal liner is accelerating inward at an increasing rate with time due to conservation of metal volume as it is compressed.

In general, there will always be an analytic formula for temperature evolution (19) when $R(t) = R_0 \sqrt{f(t)}$ where $1/f(t)$ is

analytically integrable. We have explored a class of trajectories of the form:

$$R(t) = R_0 \sqrt{1 - \left(\frac{t}{\tau_C}\right)^N}, \quad (27)$$

where $N = 1$ is the case of power-law heating described above, and $N = 2$ is an elliptical trajectory which has slower compression in the early phase and faster compression towards the end. This elliptic trajectory also gives an exact formula for temperature versus time:

$$T(t) = T_0 \left(1 - \frac{t^2}{\tau_C^2}\right)^{-1} \left(\frac{\tau_C + t}{\tau_C - t}\right)^{-\tau_C/2\tau_E}. \quad (28)$$

For $N \geq 3$ the analytic expression becomes sufficiently complicated that it is easier to evaluate (19) numerically. Overall, in terms of minimizing the required ratio τ_E/τ_C to achieve a specified amount of temperature increase (when total energy applied to compression is held constant), the $N = 1$ case yielding the power-law temperature scaling is optimum for this class of trajectories. The PCS-16 compression is closely approximated by the $N = 1$ trajectory $C_R(t) = (1 - (t - t_0)/\tau_C)^{-1/2}$ with a best fit parameters of $t_0 = 324 \pm 1.7 \mu s$ and $\tau_C = 139 \pm 1.8 \mu s$.

For completeness we also include the general formula for Ohmic heating power and compressional heating power for the power-law heating case of $T \sim C_R^\epsilon$

$$\begin{aligned} P_\Omega &= \eta \left(\frac{\psi_0 \lambda_0^2}{\mu_0}\right)^2 \left(\frac{a_0^2}{2R_{\text{axis}}(0)}\right) C_R^{3-3\epsilon/2}(t) \\ &\times \exp\left(-\frac{2}{\tau_{\psi 0}} \int C_R^{2-3\epsilon/2} dt\right), \end{aligned} \quad (29)$$

$$P_{\text{comp}} = 3 \langle n_0 T_0 \rangle V_0 C_R^{\epsilon-1}(t) \frac{dC_R}{dt}, \quad (30)$$

with parameters as defined in section 2.1.

Appendix B. Neutron yield calibration by MCNP simulation

To simulate the scattering and detection of 2.45 MeV neutrons as they pass through the experimental system, we use the Monte Carlo N-Particle (MCNP) code [58]. The neutron source used in the simulation is localized to a small toroidal region near the core of the plasma. Each simulation recorded the collision history of 4×10^7 neutrons emitted isotropically from the source in random directions. An accurate three-dimensional model of the experimental device and support structure was created, shown in figure 27, with three different versions of the model for the different modes of operation: in the lab, in the field without high explosives, and in the field with high explosives, which differed in the presence of low-Z scattering structures near the plasma vessel, with resulting calibration values shown in table 2. These simulations include geometric fall-off with distance, shielding, secondary nuclear reactions, back-scattering from any possible structures in the

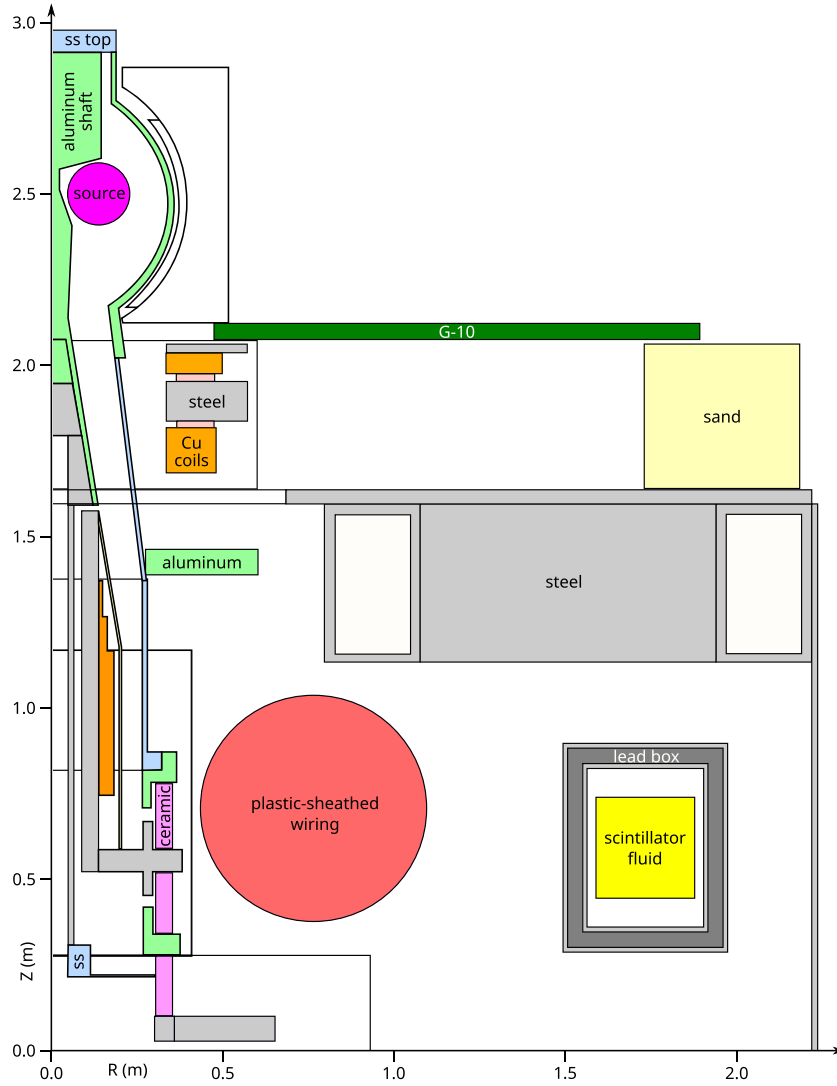


Figure 27. Geometry of the MCNP field model: The neutron source is a magenta toroid surrounding the narrowest portion of the shaft. Carbon steel used for the ferromagnetic shaft components and container reinforcement structure (hollow box beams) are shown in gray. Stainless and aluminum components are slate blue and mint green, respectively. Copper electromagnets are shown in orange. Ceramic rings are shown in pink. A bundle of plastic-sheathed wiring is approximated as a large red torus. A G-10 composite fiberglass plate used to redirect the shockwave is forest green. Sand bags are shown as pale yellow. This radial cross section cuts through a scintillator, shown in bright yellow, that is suspended inside a lead box, shown in dark gray. The geometry of the MCNP model is fully three-dimensional and an accurate representation of the distribution of materials used in the experiment.

system as well as the detection efficiency within the scintillator fluid itself. Special post-processing routines were written to model the behavior of the neutron-proton collisions within the scintillator fluid to generate a synthetic pulse height spectrum for each scintillator for comparison in experimental spectra. Direct experimental absolute calibrations of the scintillator neutron detection efficiencies using the Am-Be source at the TRIUMF nuclear physics lab were used to confirm that MCNP simulations were accurately predicting detection efficiency.

We have used these MCNP simulations to determine an overall neutron yield calibration from the set of scintillator-specific sensitivity calibrations, by the following method. Each experimental detector count rate N_i^{exp} for detector i was used to determine an estimate of neutron yield from the plasma source Y_i^{exp} as:

$$Y_i^{\text{exp}} = C_i(E_{\text{thr}}) N_i^{\text{exp}} (E \geq E_{\text{thr}}), \quad (31)$$

using the calibration factor $C_i(E_{\text{thr}})$ where E_{thr} is a minimum energy threshold for a neutron detection event. The detector-specific calibration is determined from the local tallies of proton collisions within the MCNP simulated scintillator, N_i^{sim} and depends on the minimum threshold E_{thr} for including a collision in the count. This calibration factor is:

$$C_i(E_{\text{thr}}) = \frac{Y^{\text{sim}}}{N_i^{\text{sim}} (E \geq E_{\text{thr}})}, \quad (32)$$

where there are $Y^{\text{sim}} = 4 \times 10^7$ neutrons in the final simulations used for these calibrations. Due to the complexities of the scattering geometry, the values of Y_i^{exp} will vary in practice

Table 2. Scintillator overall sensitivity calibration factor C_{all} for the different machine configurations as calculated by MCNP. The addition of low-Z materials near the plasma source, i.e. sandbags, structural foam, and HE, causes additional scattering which reduces the number of neutrons detected for the same given number emitted by the plasma.

Configuration	$C_{\text{all}}(E \geq 1 \text{ MeV})$
Laboratory	936.75 ± 10.3
Field, no HE	1218.5 ± 13.5
PCS with HE	1727.5 ± 19.1

from one scintillator to the next, and so it is reasonable to compute a weighted average calibration where the weighting factors W_i are determined by each detector's sensitivity,

$$W_i = 1/C_i(E_{\text{thr}}). \quad (33)$$

Then the weighted average of the implied total yield is:

$$\langle Y^{\text{exp}} \rangle_{\text{W}} = \frac{\sum_i W_i Y_i^{\text{exp}}}{\sum_i W_i}. \quad (34)$$

In the numerator the W_i 's and C_i 's cancel and we have :

$$\langle Y^{\text{exp}} \rangle_{\text{W}} = \frac{\sum_i N_i^{\text{exp}}(E \geq E_{\text{thr}})}{\sum_i W_i} \equiv C_{\text{all}} \sum_i N_i^{\text{exp}}(E \geq E_{\text{thr}}), \quad (35)$$

and we calculate the overall calibration C_{all} from the MCNP simulation results by inverting this relation to obtain:

$$C_{\text{all}} \equiv \frac{Y^{\text{sim}}}{\sum_i N_i^{\text{sim}}(E \geq E_{\text{thr}})}. \quad (36)$$

We can estimate the statistical error in this MCNP calibration by analyzing a data set which had the run of 4×10^7 neutrons separated into 40 separate output files of counts from 10^6 neutrons each, the number of neutron detections (of all energies) were summed separately for each detector within each 10^6 -neutron run. Then for each scintillator, the standard deviation was evaluated for the 40-element set of mean count values for the 40 simulations, which was interpreted as the standard error of the mean count for the case of $Y^{\text{sim}} = 10^6$. Let $\sigma_{\mu}(Y^{\text{sim}})$ denote the standard error of the mean for a given number of source neutrons used in an MCNP simulation. We relate this standard error from the $Y^{\text{sim}} = 10^6$ case to the $Y^{\text{sim}} = 4 \times 10^7$ case by $\sigma_{\mu}(4 \times 10^7) = \sigma_{\mu}(10^6)/\sqrt{40}$. Thus, evaluating the high (H) and low (L) cases of number of hits per detector for each scintillator we have:

$$(N_i^{\text{sim}})_{\text{H}} = \langle N_i^{\text{sim}} \rangle + \sigma_{\mu}(10^6)/\sqrt{40}, \quad (37)$$

$$(N_i^{\text{sim}})_{\text{L}} = \langle N_i^{\text{sim}} \rangle - \sigma_{\mu}(10^6)/\sqrt{40}, \quad (38)$$

with $\langle N_i^{\text{sim}} \rangle$ being the mean value of all the 40 numbers for counts from 10^6 neutrons emitted from the source, for the

i th scintillator. Finally, a total calibration can be calculated according to (36) using the low and high values for the possible average counts including statistical errors.

For the MCNP run that was subdivided for this analysis, the source calibration values were a mean value for the field configuration calibration $\langle C_i \rangle = 809.507$, a lower limit $(C_i)_{\text{L}} = 10^6/(N^{\text{sim}})_{\text{H}} = 800.66$, and a high limit $(C_i)_{\text{H}} = 10^6/(N^{\text{sim}})_{\text{L}} = 818.54$ for scintillator ID number $i=9$ through 16. (Note that scintillator SC8 was only used for laboratory calibration, and not for plasma compression in the field.) Then the symmetric error estimate is $[(C_i)_{\text{H}} - (C_i)_{\text{L}}]/2 = 8.9$, a relative error of 1.1%.

The resulting configuration-specific calibration factors (36) are determined from three different MCNP simulations of the different machine configurations (each with $Y^{\text{sim}} = 4 \times 10^7$) and are given in table 2 and are applied to the sum of neutron detector counts with $E \geq 1 \text{ MeV}$ for scintillators 9 through 16. As the various MCNP simulations differ only by small details, this error analysis derived from one run was taken to be indicative of the statistical error on the calibration factor for any MCNP simulations of the device with 4×10^7 neutrons from the source, and the same error of 1.1% was used to characterize those results.

During the PCS-16 compression, only ~ 100 neutron detection events were measured. The 1.1% error described above is relatively small compared to the Poisson noise on such a small count. For this case, the error estimate is based on doing a set of Monte Carlo simulations (described in section 4.6) using the previously established overall calibration factors for detector sensitivities. These gave a relative error on estimating source yield (n/s) in the range of $\pm 11\%$ – 4% for the PCS-16 shot, so for inferring the source yield from the detector data in this work we only use the largest of these errors.

For the 66-shot high-density aggregate of in-field formation-only shots, statistical Poisson noise will be roughly $1/\sqrt{66}$ smaller than for a single shot. This reduces the relative error on the aggregate from 11% on a single shot to 1.35% on the aggregate, which is comparable to the MCNP calibration error. However these are both insignificant compared to the 50% error on core density, which gives rise to a 13% error on final estimate of ion temperature at $300 \mu\text{s}$.

The reason why we calculate the calibration using the threshold of $E_{\text{thr}} = 1 \text{ MeV}$ is because the PSD method has an increasing rejection rate as pulse energy is decreased below that energy, with no ability to detect neutrons with $E < 0.5 \text{ MeV}$. We determined this threshold by comparing experimental and simulated pulse height energy spectra. To determine a total number of neutrons emitted from the source during $t < 750 \mu\text{s}$, the MCNP-determined value of $C_{\text{all}}(1 \text{ MeV})$ was applied to the PCS-16 data for total cumulative count for pulses $E \geq 1 \text{ MeV}$, giving a total of 114015 neutrons. A new calibration was then found to include pulses of any energy, by making it agree with the cumulative total neutrons emitted from the plasma. For the PCS-16 data we found $N^{\text{exp}}(E \geq 1 \text{ MeV}) = 66$ PSD-identified neutron detections, and $N^{\text{exp}}(E > 0 \text{ MeV}) = 103$ PSD-identified neutron detections. Thus, with the calibration for neutrons of energy above 1 MeV as

$C_{\text{all}}(1\text{ MeV}) = 1727.5$ (table 2, ‘PCS with HE’) the calibration for neutrons of all energies $C_{\text{all}}(0\text{ MeV})$ is

$$C_{\text{all}}(0\text{ MeV}) = C_{\text{all}}(1\text{ MeV}) \frac{N^{\text{exp}}(E \geq 1\text{ MeV})}{N^{\text{exp}}(E > 0\text{ MeV})} = 1106.94. \quad (39)$$

With this low-energy calibration we are able to include all PSD-identified detection in the neutron yield curves shown in figures 17 and 16. Where required, calibrations for the other two physical configurations listed in table 2 were calculated in the same manner.

Appendix C. Bayesian equilibrium reconstruction

The magnetic geometry and internal profiles of the plasma are not directly measurable, but can be estimated by finding a best match to surface magnetic measurements provided by Mirnov probes, which is generally referred to as equilibrium reconstruction. We developed a Bayesian reconstruction method [55] to match the Mirnov probes measurements at a given point in time to a large pre-computed table of Grad-Shafranov (GS) equilibria [44]. Each equilibrium is assigned a probability based on the difference between the forward-modelled magnetic fields and the Mirnov probe measurements, taking into account probe measurement errors. The output is a probability density function for each pre-tabulated physical quantity, such as poloidal flux or q profile.

Separate tables of GS equilibria are needed for each snapshot in time to account for the changing wall geometry and ψ_{wall} boundary conditions. For PCS-16 we have one GS table for the uncompressed geometry and six tables based on the compressed wall geometry starting at $t = 305\ \mu\text{s}$ and advancing in $20\ \mu\text{s}$ increments. Before compression begins, we compute reconstruction outputs every $5\ \mu\text{s}$ using the GS table from the uncompressed geometry. After $t = 405\ \mu\text{s}$ the liner is at a smaller radius than the gun, so the GS solver could not converge on equilibrium solutions. Hence the final phase of compression was not possible to analyze using this solver without making further assumptions about the plasma geometry.

The equilibria are calculated with the CORSICA solver [70], assuming no current outside the LCFS and negligible plasma pressure. The plasma current profile is constrained to be of the form²

$$2\pi \frac{dF}{d\psi} = \frac{\mu_0 J_\phi}{B_\phi} = \lambda_0 \exp [2\bar{\psi}^2 - (y_c + 2)\bar{\psi}^{12}], \quad (40)$$

where the free parameters λ_0 (in inverse meters) and y_c determine the value of normalized current density at the magnetic axis and the internal inductance of the plasma, respectively. The table of equilibria is created by scanning over the expected range of λ_0 and y_c and storing the plasma parameters and

magnetic field values at the probe locations. This form was chosen for the current profile because it has few variables and reduces the time and disk space required to store the equilibrium data. Also, for an equilibrium fit to be determined by the four Mirnov probe measurements (toroidal average of signals at each of the four poloidal positions), the profile model must have fewer than four parameters, so we prioritized the two parameters that had the highest correlation to measurable variation in magnetic field strength at the outer boundary of the plasma.

One consequence of the chosen form of the plasma current profile is that it forces the q profile to have some reversed shear near the magnetic axis, which creates the conditions for resistive instability when integer q surfaces appear in the core. The presence or non-presence of the moderate level of reversed shear implicit in this model is not determined by the set of measurements we have on the PCS-16 plasmas. The physical parameters that this model can determine with good accuracy are the total toroidal plasma current and the internal inductance of the plasma (equivalently described by the centroid of the $dF/d\bar{\psi}$ profile), which together provide an estimate of the poloidal flux of the plasma, as described in section 4.3. Overall the Bayesian reconstruction for PCS-16 has a relative error in comparison to Mirnov probe values of 5%–7%.

Appendix D. Electron temperature lower bound from poloidal flux decay

From the loop voltage $V = d\psi/dt$ determined in the Mirnov-corrected VAC method of section 4.3 we can infer a resistivity at the magnetic axis, which we can then combine with an estimate for Z_{eff} to determine an implied electron temperature through the Spitzer formula [61, 65]. Neoclassical corrections are not applicable to the magnetic axis of the plasma where the resistive flux cancellation is occurring, so a Spitzer model of resistivity is sufficient. On the other hand, the current density at the magnetic axis might be locally enhanced at the magnetic axis due to surrounding higher (neoclassical) resistivity. Furthermore, resistive decay of edge currents can cause the profile to become increasingly peaked with time, which would result in lower magnetic signals at the wall even if poloidal flux was perfectly conserved at the core. Therefore this estimate of $T_e(t)$ will be a lower bound, which pessimistically assumes that apparent reduction of relative signal at the wall is due entirely to resistive flux loss at the core of a simple current profile.

The resulting lower bound for electron temperature can be seen in figure 28, shown for the case of $Z_{\text{eff}} = 3$. The resulting temperature estimate has several interesting features. Before compression begins the initial decay of $T_e(t)$ has a time constant of $\tau_{T_e} = 372\ \mu\text{s}$. Then during the early phase of slowly accelerating compression until $t = 324\ \mu\text{s}$ we see a trend of T_e decreasing from initial value of 104 eV at the time of liner move, down to 89.7 eV when the compression begins to accelerate faster. Once in the faster phase of compression, $t > 324\ \mu\text{s}$, where the trajectory matches (25) we find that the resistive estimate $T_e(t)$ begins increase according

² This form for the current profile, which we have found to be a useful parameterization, does not have a previously published source that the authors are aware of. It appears to first occur in the CORSICA source code, along with a comment attributing it to William M Nevins.

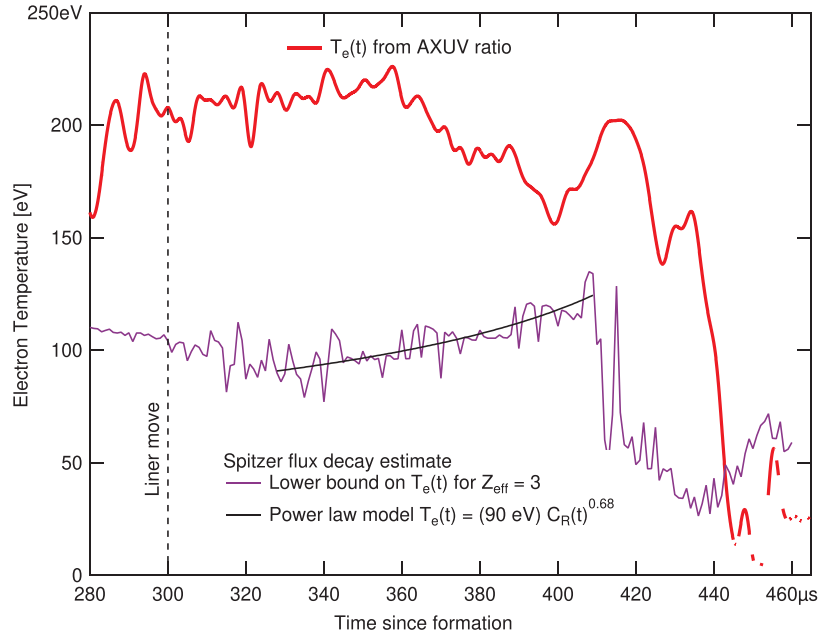


Figure 28. PCS-16 lower bound estimate of electron temperature calculated from Spitzer resistivity inferred from the poloidal flux decay rate for $Z_{\text{eff}} = 3$ (purple trace). The red trace is the measured $T_e(t)$ from the AXUV diagnostic (filter ratio method). The black curve is a power-law fit to the lower bound T_e resulting in a heating exponent of $\epsilon = 0.68$.

power-law heating formula $T_e(t) = T_{e0} C_R^\epsilon(t)$ with $\epsilon = 0.68 \pm 0.05$, until reaching 133 eV just before a rapid loss of heat at $410 \mu\text{s}$ occurs (at $C_R = 1.59$). Interpreting this heating as due entirely to thermodynamic compression through the relation (3), this fitted value of $\epsilon = 0.68$ and $\tau_C = 138.8 \mu\text{s}$ would correspond to $\tau_{E_e} = 211 \mu\text{s}$. Note that this is an effective net τ_E that indirectly includes Ohmic heating as a ‘negative loss’; the conventional energy confinement time taking into account the full energy balance will be a smaller number. Our MHD simulations (section 5.2), with electron transport adjusted to match the plasma current decay, exhibits a conventionally defined confinement time $\tau_E \approx 84 \mu\text{s}$, while the energy balance described for AXUV T_e analysis in section 4.4 yielded $\tau_{E_e} \approx 50 \mu\text{s}$. The approximately four times longer τ_{E_e} from ignoring non-compressional heating terms indicates that electron compressional heating power is roughly one quarter of the total electron heating power, closely in agreement with direct estimates of all terms (recall $P_{\text{comp},e}$ was $1/4.4$ of total power calculated in section 4.4).

We also find it worthwhile to note the similarities and differences between the time evolution of Spitzer estimate of $T_e(t)$ and the AXUV-ratio measurement of $T_e(t)$. Both observe a crash in temperature. However, the AXUV measurement has a transient local maximum coincident with the crash of the resistive estimate at $t = 410 \mu\text{s}$. It is possible that the resistive loss of flux at that moment is driving increased Ohmic heating in a small region that is being observed by the AXUV system. There is also a noticeable difference the general trend of the two signals, the AXUV starts falling after $t = 360 \mu\text{s}$ while the resistive estimate keeps climbing. Although the AXUV measurement is close to isothermal, there is possibly a small rise of $\Delta T_e = 14.5 \text{ eV}$ during the first $60 \mu\text{s}$ which would yield a heating exponent of $\epsilon = 0.40 \pm 0.02$, which is at least roughly

similar to the 0.68 of the resistive estimate. The temperature from resistive flux decay is roughly half of the AXUV measurement. These measurements could be reconciled by assuming a very high $Z_{\text{eff}} > 7$ for the resistive estimate, which is highly unlikely due to physical considerations presented in appendix G. However, the resistive estimate is a lower bound, as discussed in appendix D. More plausible interpretations for their discrepancy include the PCS-16 plasma current profile being more centrally peaked than the VAC SR981 simulation.

Appendix E. Electron temperature lower bound from neutron measurements

The observation of a decaying neutron yield in the multi-shot aggregate allows us to put a lower bound on the pre-compression electron temperature at the time of liner move. The ion temperature will decay due to collisions with electrons and due to transport losses, evolving according to

$$\frac{dT_i}{dt} = \frac{T_e - T_i}{\tau_{\text{eq}}} - \frac{T_i}{\tau_{Ei}}. \quad (41)$$

The equilibration rate due to electron-ion collisions is given by (e.g. [71])

$$\tau_{\text{eq}}^{-1} = \frac{n_e e^4 m_e^{1/2} \ln \Lambda}{3\pi (2\pi)^{1/2} \epsilon_0^2 m_i (kT_e)^{3/2}}, \quad (42)$$

where e is the elementary charge and ϵ_0 is the permittivity of free space. The Coulomb logarithm is $\ln \Lambda \approx 31 + \ln T_e - 0.5 \ln n_e$ with T_e in electron volts and n_e in particles per cubic meter. For $n_e = 2 \times 10^{14} \text{ cm}^{-3}$ and $T_e = 200 \text{ eV}$ the equilibration time is $\tau_{\text{eq}} = 693 \mu\text{s}$. The colder the electrons the faster

the ions cool, because both the temperature difference and the equilibration rate are larger. A lower bound on electron temperature is obtained by assuming transport losses are negligible and attributing all of the ion cooling to equilibration with electrons. The steady exponential-like decay of the ion temperature inferred from neutron yield data implies that we can assume constant electron temperature and solve

$$-\frac{T_i}{\tau} = \frac{T_e - T_i}{\tau_{\text{eq}}(T_e)} \quad (43)$$

for T_e , considering T_i as a fixed parameter. Assuming n_e in the range $(1-3) \times 10^{14} \text{ cm}^{-3}$ and $f_D \equiv n_d/n_e$ in the range 0.7–0.9, the neutron yield analysis gives us data for ion temperature T_i and its decay rate τ on this range. We find that the data is described by the power law that has the same exponent in both aggregates (equal to the exponent of temperature in the exponential of the reactivity (15) slightly renormalized by the algebraic prefactor). For the high-density aggregate $(\tau/1 \text{ ms})(T_i/1 \text{ eV})^{0.36} \approx 9$ from data on $516 \text{ eV} < T_i < 635 \text{ eV}$. For the low-density aggregate $(\tau/1 \text{ ms})(T_i/1 \text{ eV})^{0.36} \approx 12$ from data on $604 \text{ eV} < T_i < 816 \text{ eV}$. The power law is independent of f_D . Assuming uniform probability density for n_e and f_D this data induces a distribution for the lower bound temperature T_e^{min} that we calculate using a Monte Carlo method. Reporting the median temperature and full error bounds we have:

- For the high-density aggregate the lower bound is $T_e^{\text{min}} = 125_{-16}^{+14} \text{ eV}$
- For the low-density aggregate $T_e^{\text{min}} = 137_{-28}^{+26} \text{ eV}$.

The uncertainty in the lower bound comes from the range of density used in the calculation; the fuel dilution ratio has little influence. For a particular density $n_e = 10^{20} \text{ m}^{-3}$ the lower bounds are well defined and separated, with $T_e^{\text{min}} \approx 127 \text{ eV}$ and $T_e^{\text{min}} \approx 149 \text{ eV}$ for high-density and low-density aggregates, respectively. The calculated lower bounds are consistent with the AXUV measured temperature for PCS-16 at the liner move, $T_e(300 \mu\text{s}) = 207 \pm 10 \text{ eV}$.

Appendix F. Ion thermalization

The ion–ion collision time τ_i that describes the time to establish a thermal distribution of ion velocities is given by [65]

$$\tau_i = \frac{12\pi^{3/2}\epsilon_0^2 m_i^{1/2} (kT_i)^{3/2}}{n_i e^4 \ln \Lambda_i} \quad (44)$$

with $\ln \Lambda_i = 30 + 1.5 \ln T_i - 0.5 \ln n_i$ for T_i in eV and n_i in ions per m^3 . In the case of the PCS-16 experiment, taking $n_i = 2 \times 10^{14} \text{ cm}^{-3}$ and $T_i = 600 \text{ eV}$ (figure 18), we find $\tau_i \approx 130 \mu\text{s}$. This is less than the time since formation of the plasma ($300 \mu\text{s}$) and short compared to the temperature decay time ($\tau \approx 930 \mu\text{s}$ for the high-density aggregate). Monte Carlo analysis of the high-density aggregate data gives $\tau_i/\tau = 0.09_{-0.06}^{+0.14}$. This lends support to our working assumption of a thermalized ion population made in the neutron analysis.

Appendix G. Effective charge and fuel dilution

To interpret the experimental data it is helpful to have probable values for the effective ion charge Z_{eff} that determines the plasma resistivity. This quantity is difficult to measure, and for PCS-16 we have no direct measurement, but seems roughly constrained by the observed resistive decay of the plasma to be in the range $Z_{\text{eff}} \lesssim 3$ by comparison to simulations based on a Spitzer resistivity model (a neoclassical model would require even lower Z_{eff} to match the observations). Here we provide further arguments to support this range. First of all, we note that, by definition, $1 \leq \langle Z \rangle \leq Z_{\text{eff}}$ where $\langle Z \rangle$ is the average ion charge. Also, if a plasma contains impurity ions of maximum charge Z_{max} then $Z_{\text{eff}} < Z_{\text{max}}$. Consider first the case of an impurity like carbon. Simulation of the ionization process shows that the time to approach coronal equilibrium for carbon typically exceeds the duration of the experiment. Assuming that impurity ions are no more ionized than they would be in coronal equilibrium at $T_e = 200 \text{ eV}$, we estimate that $Z_{\text{max}} \lesssim 7$ for any impurity [72]. And actually having $Z_{\text{eff}} \approx Z_{\text{max}}$ would require an implausible plasma composition, given the strong gettering effect of the lithium-coated walls. An exception to this argument is lithium itself. However, if the dominant impurity was Li^{+3} the plasma would have to be nearly fully lithium to have $Z_{\text{eff}} = 3$. For example, a dirty plasma whose ions were 30% Li^{+3} , 5% C^{+4} and 1% Al^{+9} , with the remainder being deuterons, would have $\langle Z \rangle = 1.83$ and $Z_{\text{eff}} = 2.70$. Thus we assume that $Z_{\text{eff}} \leq 3$. It is worth noting that a significant lithium impurity concentration would have a large effect on the fuel dilution factor for a given Z_{eff} , due to its low Z , giving $f_D = 0.35$ in this dirty-plasma case. We believe that this example is extreme. Therefore, for the purpose of interpreting the neutron yield we assume that $0.7 < f_D < 0.9$

ORCID iDs

- S.J. Howard  <https://orcid.org/0009-0007-3247-6096>
M. Reynolds  <https://orcid.org/0000-0001-5880-2290>
A. Froese  <https://orcid.org/0000-0002-1669-7397>
I.V. Khalzov  <https://orcid.org/0000-0003-1355-0303>
C.P. McNally  <https://orcid.org/0000-0002-2565-6626>
M. Laberge  <https://orcid.org/0009-0006-0093-2168>

References

- [1] Kirkpatrick R.C., Lindemuth I.R. and Ward M.S. 1995 *Fusion Technol.* **27** 201–14
- [2] Laberge M. 2008 *J. Fusion Energy* **27** 65–68
- [3] Howard S., Laberge M., McIlwraith L., Richardson D. and Gregson J. 2009 *J. Fusion Energy* **28** 156–61
- [4] Froese A. et al 2014 Spheromak compression experiments at General Fusion 19th Pacific Basin Nuclear Conf. (PBNC 2014) (Vancouver, Canada, August 2014) (Canadian Nuclear Society (CNS)) (available at: www.proceedings.com/26102.html) p 2151
- [5] Marshall J. 1960 *Phys. Fluids* **3** 134–5
- [6] Bellan P.M. 2000 *Spheromaks* (Imperial College Press) (available at: www.worldscientific.com/doi/abs/10.1142/p121)

- [7] Raman R. and Shevchenko V.F. 2014 *Plasma Phys. Control. Fusion* **56** 103001
- [8] Yamada M., Ono Y., Hayakawa A., Katsuragi M. and Perkins F.W. 1990 *Phys. Rev. Lett.* **65** 721–4
- [9] Browning P.K., Cunningham G., Duck R., Gee S.J., Gibson K.J., Kitson D.A., Martin R. and Rusbridge M.G. 1992 *Phys. Rev. Lett.* **68** 1722–5
- [10] Nelson B.A., Jarboe T.R., Orvis D.J., McCullough L.A., Xie J., Zhang C. and Zhou L. 1994 *Phys. Rev. Lett.* **72** 3666–9
- [11] Jarboe T.R., Bohnet M.A., Mattick A.T., Nelson B.A. and Orvis D.J. 1998 *Phys. Plasmas* **5** 1807–14
- [12] Redd A.J., Nelson B.A., Jarboe T.R., Gu P., Raman R., Smith R.J. and McCollam K.J. 2002 *Phys. Plasmas* **9** 2006–13
- [13] Shimamura S., Taniguchi M., Takahashi T. and Nogi Y. 1995 *Fusion Technol.* **27** 361–4
- [14] Nagata M., Kanki T., Fukumoto N. and Uyama T. 2003 *Phys. Plasmas* **10** 2932–9
- [15] Wurden G.A., Intrator T.P., Clark D.A., Maqueda R.J., Taccetti J.M., Wysocki F.J., Coffey S.K., Degnan J.H. and Ruden E.L. 2001 *Rev. Sci. Instrum.* **72** 552–5
- [16] Degnan J.H. et al 2013 *Nucl. Fusion* **53** 093003
- [17] Degnan J.H. et al 1999 *Phys. Rev. Lett.* **82** 2681–4
- [18] Kirtley D. and Milroy R. 2023 *J. Fusion Energy* **42** 30
- [19] Gomez M.R. et al 2020 *Phys. Rev. Lett.* **125** 155002
- [20] Yamada M. et al 1990 *Phys. Fluids B* **2** 3074–80
- [21] Dunlea C., Howard S., Zawalski W., Epp K., Mossman A., Xiao C. and Hirose A. 2020 *Phys. Plasmas* **27** 062513
- [22] Henins I., Fernandez J.C., Jarboe T.R., Marsh S.P., Marklin G.J., Mayo R.M. and Wysocki F.J. 1989 Design of a spheromak compressor driven by high explosives *Technical Report LA-UR-89-4006* (Los Alamos National Laboratory) (available at: www.osti.gov/biblio/5167829)
- [23] Ellis R. 1985 *Nucl. Fusion* **25** 1145
- [24] Bol K., Cecchi J.L., Daughney C.C., DeMarco F., Ellis J.R.A., Eubank H.P., Furth H.P., Hsuan H., Mazzucato E. and Smith R.R. 1974 Experiments on the adiabatic toroidal compressor *Technical Report* (available at: <https://doi.org/10.2172/4203067>)
- [25] Bol K. et al 1972 *Phys. Rev. Lett.* **29** 1495–8
- [26] Askinazi L., Andrejko M. and Golant V. 2001 *J. Plasma Fusion Res. Ser.* **4** 224–8 (available at: https://www.jspf.or.jp/JPFERS/PDF/Vol4/jpfers2001_04-224.pdf)
- [27] Robinson D. 1985 *Nucl. Fusion* **25** 1101–8
- [28] Kaita R. et al 1986 *Nucl. Fusion* **26** 863
- [29] Tait G., Bell M. and Bell J. 1985 Adiabatic toroidal compression and free-expansion experiments in TFTR *Plasma Physics and Controlled Nuclear Fusion Research 1984 (Proc. 10th Int. Conf.) (London, 1984)* vol 1 (IAEA) pp 141–54 (available at: <https://inis.iaea.org/search/16032318>)
- [30] Grove D.J. and Meade D.M. 1985 *Nucl. Fusion* **25** 1167–72
- [31] Wesson J. 1999 The science of ‘JET’ JET-R(99) vol 13 (available at: www.euro-fusion.org/archives/jet-archive/the-science-of-jet)
- [32] Tanga A. et al 1987 Effects of major radius compression in JET *JET Joint Undertaking Progress Report 1986*, EUR 11113 EN(EUR-JET-PR4) pp 211–14 (available at: <http://aei.pitt.edu/57920/1/JET.J.U.1986.pdf>)
- [33] Siemon R., Lindemuth I. and Schoenberg K. 1999 *Comments Plasma Phys. Control. Fusion* **8** 363–86 (available at: www.researchgate.net/publication/350529732_Why_Magnetized_Target_Fusion_Offers_a_Low-Cost_Development_Path_for_Fusion_Energy)
- [34] Miller R.L. and Krakowski R.A. 1980 Assessment of the slowly-imploding liner (linus) fusion reactor concept *Technical Report LA-UR-80-3071* (Los Alamos National Labs) (available at: www.osti.gov/biblio/6769582)
- [35] Howard S., Mossman A. and Donaldson M. 2016 *58th Annual Meeting of the APS Division of Plasma Physics (San Jose, California, October 2016)* (Bulletin of the American Physical Society) vol 61 p C10.104 (available at: <http://meetings.aps.org/link/BAPS.2016.DPP.CP10.104>)
- [36] Reynolds M., Froese A., Barsky S., Devietien P., Toth G., Brennan D. and Hooper B. 2016 *58th Annual Meeting of the APS Division of Plasma Physics (San Jose, California, October 2016)* (Bulletin of the American Physical Society) vol 61 p C10.108 (available at: <http://meetings.aps.org/link/BAPS.2016.DPP.CP10.108>)
- [37] O’Shea P., Laberge M., Donaldson M. and Delage M. 2016 *58th Annual Meeting of the APS Division of Plasma Physics (San Jose, California, October 2016)* (Bulletin of the American Physical Society) vol 61 p C10.103 (available at: <http://meetings.aps.org/link/BAPS.2016.DPP.CP10.103>)
- [38] Laberge M., O’Shea P., Donaldson M. and Delage M. 2017 *59th Annual Meeting of the APS Division of Plasma Physics (Milwaukee, Wisconsin, October 2017)* (Bulletin of the American Physical Society) vol 62 p U11.136 (available at: <http://meetings.aps.org/link/BAPS.2017.DPP.UP11.134>)
- [39] Reynolds M., Barsky S. and de Vietien P. 2017 *59th Annual Meeting of the APS Division of Plasma Physics (Milwaukee, Wisconsin, October 2017)* (Bulletin of the American Physical Society) vol 62 U11.133 (available at: <http://meetings.aps.org/link/BAPS.2017.DPP.UP11.131>)
- [40] Young W., Carter N., Howard S., Carle P. and O’Shea P. 2017 *59th Annual Meeting of the APS Division of Plasma Physics (Milwaukee, Wisconsin, October 2017)* (Bulletin of the American Physical Society) vol 62 p U11.132 (available at: <http://meetings.aps.org/link/BAPS.2017.DPP.UP11.130>)
- [41] Howard S., Hildebrand M. and Barsky S. 2018 *60th Annual Meeting of the APS Division of Plasma Physics (Portland, Oregon, November 2018)* (Bulletin of the American Physical Society) vol 63 p C11.189 (available at: <http://meetings.aps.org/link/BAPS.2018.DPP.CP11.189>)
- [42] O’Shea P. 2018 *60th Annual Meeting of the APS Division of Plasma Physics (Portland, Oregon, November 2018)* (Bulletin of the American Physical Society) vol 63 NO6.012 (available at: <http://meetings.aps.org/link/BAPS.2018.DPP.NO6.12>)
- [43] Hooper E.B. et al 2012 *Plasma Phys. Control. Fusion* **54** 113001
- [44] Grad H. and Rubin H. 1958 Hydromagnetic equilibria and force-free fields *Technical Report* (United Nations United Nations (UN) iNIS-XU-021) (available at: <https://inis.iaea.org/search/39082408>)
- [45] Furth H.P. and Yoshikawa S. 1970 *Phys. Fluids* **13** 2593–6
- [46] Turner W.C., Goldenbaum G.C., Granneman E.H.A., Hammer J.H., Hartman C.W., Prono D.S. and Taska J. 1983 *Phys. Fluids* **26** 1965–86
- [47] Luxon J.L. and Davis L.G. 1985 *Fusion Technol.* **8** 441–9
- [48] ITER 2002 ITER technical basis, ITER EDA documentation series *Technical Report* (IAEA/ITEREDA/DS/24 IAEA Vienna) (available at: www.iaea.org/publications/6492/iter-technical-basis)
- [49] Brennan D., Froese A., Reynolds M., Barsky S., Wang Z., Delage M. and Laberge M. 2020 *Nucl. Fusion* **60** 046027
- [50] Brennan D., Froese A., Reynolds M., Barsky S., Wen A., Wang Z., Delage M. and Laberge M. 2021 *Nucl. Fusion* **61** 046047
- [51] Colchin R.J., Hillis D.L., Maingi R., Klepper C.C. and Brooks N.H. 2003 *Rev. Sci. Instrum.* **74** 2068–70
- [52] Carle P., Froese A., Wong A., Howard S., O’Shea P. and Laberge M. 2016 *Rev. Sci. Instrum.* **87** 11E104
- [53] Strand O.T., Goosman D.R., Martinez C., Whitworth T.L. and Kuhlow W.W. 2006 *Rev. Sci. Instrum.* **77** 083108
- [54] Taylor J.B. 1986 *Rev. Mod. Phys.* **58** 741–63

- [55] Froese A. *et al* 2022 *64th Annual Meeting of the APS Division of Plasma Physics (Spokane, Washington, October 2022)* (Bulletin of the American Physical Society) vol 67 B11.003 (available at: <https://meetings.aps.org/Meeting/DPP22/Session/BP11.3>)
- [56] Chung H.K., Chen M., Morgan W., Ralchenko Y. and Lee R. 2005 *High Energy Density Phys.* **1** 3–12
- [57] Roush M., Wilson M. and Hornyak W. 1964 *Nucl. Instrum. Methods* **31** 112–24
- [58] James M.R. *et al* MCNP6™ user's manual code version 6.1.1 beta *Technical Report LA-CP-14-00745* (Los Alamos National Laboratory)
- [59] Leemis L.M. 1991 *Manage. Sci.* **37** 886–900
- [60] Lewis P.A.W. and Shedler G.S. 1979 *Nav. Res. Logist. Q.* **26** 403–13
- [61] Beresnyak A. 2023 NRL plasma formulary (Naval Research Lab.) (available at: www.nrl.navy.mil/News-Media/Publications/NRL-Plasma-Formulary/)
- [62] Glasser A., Wang Z. and Park J.K. 2016 *Phys. Plasmas* **23** 112506
- [63] Wang Z., Glasser A.H., Brennan D., Liu Y. and Park J. 2020 *Phys. Plasmas* **27** 122503
- [64] Tóth G. 1996 *Astrophys. Lett. Commun.* **34** 245
- [65] Wesson J. 2011 *Tokamaks (International Series of Monographs in Physics)* 4th edn (Oxford University Press)
- [66] Goldston R.J. 1984 *Plasma Phys. Control. Fusion* **26** 87–103
- [67] Rechester A.B. and Rosenbluth M.N. 1978 *Phys. Rev. Lett.* **40** 38–41
- [68] Biewer T.M. *et al* 2003 *Phys. Rev. Lett.* **91** 045004
- [69] Eddleman J., Hammer J., Hartman C., McLean H. and Molvik A. 1995 Final report on the LLNL compact torus acceleration project *Technical Report UCRL-ID-120238 110784* (available at: www.osti.gov/servlets/purl/110784-nKV800/webviewable/)
- [70] Crotinger J., LoDestro L., Pearlstein L., Tarditi A., Casper T. and Hooper E. 1997 CORSICA: a comprehensive simulation of toroidal magnetic-fusion devices. Final report to the LDRD Program *Technical Report UCRL-ID-126284 (LLNL Report)* (available at: <https://dx.doi.org/10.1088/0741-3335/54/11/113001>)
- [71] Goldston R.J. and Rutherford P.H. 1995 *Introduction to Plasma Physics* (Taylor and Francis)
- [72] Post D., Jensen R., Tarter C., Grasberger W. and Lokke W. 1977 *At. Data Nucl. Data Tables* **20** 397–439